ACTIVE CONTROL OF THE FLOW PAST A CYLINDER EXECUTING ROTARY MOTIONS

Thesis by

Phillip Takeo Tokumaru

In Partial Fulfillment
of the Requirements for the degree of
Doctor of Philosophy

California Institute of Technology
Pasadena, California

1991

(Submitted May 31,1991)

Dedicated to my parents,
Tadasu and Anne-Marie Tokumaru

Acknowledgments

First, I would like to thank Mom and Dad, my sisters, Isabelle and Maria, and my advisor, Paul Dimotakis. I could not have performed this research without their support, patience, and understanding.

I'd also like to thank the rest of my committee, Don Coles, Hans Hornung, Jim Knowles, and Anatol Roshko; as well as Tony Leonard, Dave Dowling, Manooch Koochesfahani, Dan Lang, Rick Miake-Lye, Greg Smedley, and Derek Lisoski, for lending their hands, ears, talents, and insights; Herb Gaebler, Harry Hamaguchi, and Pavel Svitek, in the Hydro Lab, who helped me setup and run my experiments; and George Lundgren, George Wilson, Phil Wood, of the Aero Shop, who helped me design and build my apparatus. Finally, this research was supported by the Air Force Office of Scientific Research, URI AFOSR Grant No. F49620-86-C-0134.

Abstract

Exploratory experiments have been performed on circular cylinders executing forced rotary motions in a steady uniform flow. These motions include harmonic oscillations, steady rotation, and combinations of the two. Flow visualization and laser-Doppler velocimetry measurements were used to characterize the wake structure, and to estimate the convection speed, spacing, and strength of the vortical structures. Laser-Doppler velocimetry measurements were also made to estimate the cylinder drag coefficient and wake displacement thickness. In addition, the periodic flow close the cylinder and in the near wake region was mapped for a particular forced case. The data show that a considerable amount of control can be exerted over the flow by such means. In particular, a large increase, or decrease, in the resulting displacement thickness, estimated cylinder drag, and associated mixing with the free stream can be achieved, depending on the frequency and amplitude of oscillation. In order to assess the effects of oscillatory forcing on a cylinder with a net (mean) rotation rate, a novel method for estimating the steady lift forces was employed. Using this method, it was also found that the addition of forced rotary oscillations to the steady rotation of the cylinder helped to increase C_L in the cases where the wake would normally be separated in the steadily rotating case, and decrease it otherwise. Results obtained for a steadily rotating cylinder (no forced oscillations) compare favorably with similar data published in the literature.

Table of contents

List of figures

CHAPTER 1

Introduction

1.1 Preface

The title of the thesis, "Active Control of the Flow Past a Cylinder Executing Rotary Motions," can mean different things to different people. In this case, it refers to the flow past a circular cylinder in a water tunnel. This cylinder was bounded at both ends and below by test section walls, and from above by the water tunnel free surface. See Fig. 1.1. To control the structure of the flow, the cylinder was programmed to execute rotary motions about its axis. This control strategy is called "active," because energy must be (actively) supplied to execute these motions, *cf.* "passive" controls, such as spoilers or riblets, which require no special input of energy. Since no feedback was necessary (or used) the forcing was under "open-loop," or "program" control.

In the past this has been called "forcing the flow," and if the flow responded in a periodic way, terms like "resonance," "locking," and "synchronization" were used. The notion of controlling unsteadiness was reserved for the *elimination* of instabilities. The aim of the present investigations, however, is to *program* the inevitable vortical structures that dominate unsteady flow behind a circular cylinder.

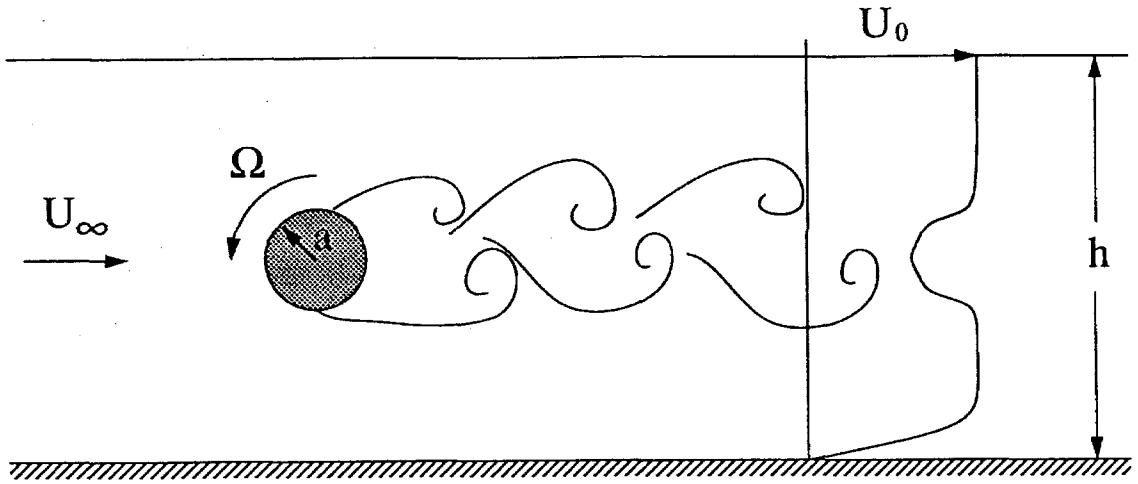

FIG. 1.1 Configuration

1.2 Background

Traditionally, experiments involving a cylinder executing rotary motions in a uniform flow have been performed with cylinder motions that are either harmonic oscillations or steady rotation. It is believed that the present investigations are the first to examine cylinder motions combining the two. Because of this, background material for the oscillating and steadily rotating cases falls naturally into two parts presented here as Secs. 1.2.2 "Rotary oscillations" and 1.2.3 "Steady rotation." Section 1.2.1 introduces a class of forcing functions which includes (rotary) oscillations plus net rotation of the cylinder.

1.2.1 Forcing parameters

The motion of the cylinder in the present experiments can be described by a single equation; *i.e.*,

$$\Omega = \Omega_0 + \Omega_1 \sin(2\pi f t) , \tag{1.2.1}$$

where

$$\Omega \equiv \frac{\dot{\theta}\, a}{U_\infty} , \tag{1.2.2}$$

is the normalized rotation rate of the cylinder, a is the cylinder radius, U_∞ is the free-stream velocity, t is the time, $\dot{\theta}$ is the angular velocity of the cylinder, f is the forcing frequency, and, Ω_0 and Ω_1 are amplitudes of the steady and harmonic components of the cylinder motion. The normalized forcing frequency is

$$S_f \equiv \frac{2\, a\, f}{U_\infty} , \tag{1.2.3}$$

i.e., the forcing Strouhal number.

Three forcing parameters are considered in the present experiments, Ω_0, Ω_1, and S_f. In addition, another important parameter is the Reynolds number,

$$Re \equiv \frac{2\, a\, U_\infty}{\nu} , \tag{1.2.4}$$

where ν is the kinematic viscosity.

Another dimensionless quantity which might have been used is the angular position of the cylinder, $\theta(t)$. In the present experiments, however, $\Omega(t)$ was used in favor of $\theta(t)$ to provide consistent notation for the normalized mean (Ω_0) and harmonic (Ω_1) components of the rotation rate. Using angular position to describe the motion of a cylinder with a net rotation rate is awkward. Note that with $\Omega_0 = 0$ (no net rotation rate), $S_f = 1$, and $\Omega_1 = 2$, the amplitude of the oscillations in the angular position of the cylinder is $\theta_1 \approx 36.5°$.

1.2.2 Rotary oscillations

The dynamic behavior of the flow over a bluff body is dominated by large scale vortical structures shed in its wake. Weihs (1972) proposed a methodology for predicting the structure of such a wake and found that it could become wider, narrower, or remain the same, depending on the initial strength and spacing of these vortices. His work was primarily aimed at describing the wake behind an oscillating airfoil (*e.g.*, Bratt 1953, Koochesfahani 1987). Nevertheless, Weihs's results do suggest the potential for effective control of wakes in general.

Okajima *et al.* (1975) examined the forces acting on a rotationally oscillating cylinder, for Reynolds numbers based on cylinder diameter in the range of $40 \leq Re \leq 6 \times 10^3$. Their measurements were for a normalized peak rotation rate in the range $0.2 \leq \Omega_1 \leq 1.0$, and a forcing Strouhal number in the range $0.05 \leq S_f \leq 0.3$. They noted a "synchronization" similar to that observed, for example, by Bishop & Hassan (1964), Koopman (1967), and, more recently, Ongoren & Rockwell (1988a,b), and Williamson & Roshko (1988) for a cylinder in transverse and in-line oscillation. Both Okajima and Bishop & Hassan reported a hysteresis in their measurements for increasing and decreasing S_f. Investigations at similarly low normalized forcing frequencies, amplitudes and Reynolds numbers were also performed by Wu *et al.* (1989). Taneda (1978) demonstrated that in the range $30 \leq Re \leq 300$, the "dead water" region behind a cylinder can be removed for Ω_1 sufficiently large ($\Omega_1 > 7$ to 27, depending on such factors as the cylinder span and tank width). For somewhat larger Ω_1 vortex shedding was inhibited. Similar behavior was also documented by Williams & Amato (1988) using a line of unsteady pulsing jets embedded in the trailing edge of the cylinder, at a comparable Reynolds number of 370.

The present experiments covered in Chs. 3 and 4 were performed on circular cylinders executing forced rotary oscillations in a uniform flow (no mean rotation rate). The Reynolds numbers are higher than in previous investigations at $Re = 1.5 \times 10^4$ in Ch. 3 and $Re = 2.1 \times 10^4$ in Ch. 4. Okajima *et al.* approached these Reynolds numbers ($\leq 6 \times 10^3$), but their experiments examined perturbations of the flow employing peak forcing amplitudes, Ω_1, an order of magnitude lower than in the present investigations.

In Ch. 3, flow visualization data were used to characterize the wake structure, and to estimate the convection speed, spacing, and strength of the vortical structures. In addition, LDV measurements were made to estimate the cylinder drag coefficient, and wake displacement thickness. The data show that a considerable amount of control can be exerted over the wake flow by such means. In addition, a large increase, or decrease, in the associated displacement thickness, estimated cylinder drag, and mixing with the free stream was achieved, depending on the frequency and amplitude of oscillation. See also Tokumaru & Dimotakis (1991).

Chapter 4 examines a particular case of a cylinder executing forced rotary oscillations. An estimate of the unsteady, phase-averaged streamfunction was made. It was found that the forced shedding mechanism gathers vorticity close to the cylinder surface and then releases it into the flow. This is in contrast to natural (unforced) shedding, where the vorticity is released into the flow from more-or-less steady separation points, allowing the vortices to form in the wake. The speed and strength of the forced vortical structures was estimated and it was found that very little of the asymmetry (quantified by the circulation generated at the cylinder surface) is found in the wake.

1.2.3 Steady rotation

A rotating cylinder moving in a uniform stream experience a force normal to the direction of motion. Goldstein (1938) makes several historical references for both rotating spheres and cylinders and credits Magnus (1853) with the first laboratory experiments examining the lift on a rotating cylinder. Early in this century, experiments on a circular cylinder rotating about its axis in a uniform flow were performed by Reid (1924), Prandtl (1925), Thom (1926, 1931), for example. Now, on the verge of the 21st century researchers continue to find this flow interesting, *e.g.*, the experiments and simulations of Badar, *et al.* (1990) for the flow past a cylinder impulsively started in both rotation and translation.

It can be shown that the mean lift coefficient of a 2-D body can be written as

$$C_L \equiv \frac{L}{\rho U_\infty^2 a} = -\frac{\Gamma}{U_\infty a}\,, \tag{1.2.5}$$

where ρ is the fluid density, U_∞ is the free-stream velocity, a is the cylinder radius, L is the lift per unit span, and Γ is the circulation taken round a contour enclosing the lifting body. See for example Taylor (1925), Thwaites (1960, § V.9). That this circulation could be measured around contours close to the cylinder was shown experimentally by Thom (1931).

In the potential flow prototype of a rotating cylinder in a uniform free stream, the rotation of the cylinder is modeled by placing a point vortex of strength Γ at its center. When modeling a flow, Γ should be considered as a parameter to be adjusted so that the flow is properly represented; *e.g.*, to satisfy the Kutta Condition. Proposing that C_L can be made arbitrarily large by arbitrarily increasing Γ is not very helpful; Γ *is* the mean lift; *cf.* Eq. 1.2.5.

Prandtl (1925) argued that the maximum circulation, Γ_{max}, which could be realized about the rotating cylinder was equal to the circulation at which the upstream and downstream stagnation points join on the bottom of the cylinder. From the potential flow analog of that case, a value of

$$\Gamma_{max} = 4\pi U_\infty a \tag{1.2.6}$$

is used. See also the discussion in Goldstein (1938 **I**, pp. 81-84). Beyond this point, Prandtl argued that no circulation could be shed by the cylinder to infinity as it is ramped up from rest to some constant rotation rate of $\Omega_0 > 4$, fixing the total circulation at infinity and the lift of the rotating cylinder thereby. If this argument were correct, the maximum (steady state) lift coefficient that can be realized would be given by,

$$C_{L_{max}} = 4\pi \approx 12.6\,. \tag{1.2.7}$$

It is not at all clear from the discussions in the literature, but Prandtl relates the real and potential flow case of the rotating cylinder, not by matching the circulation calculated by taking a contour round the cylinder at the surface, as one would expect, but by matching the *peak* circumferential velocities in the two cases. Not coincidently, this is also the choice that "looks right."

Chapter 5 examines the effect of cylinder rotation on the flow ahead of the cylinder. In order to assess the effects of forcing, a novel method for describing the flow ahead of the cylinder, in terms of the strength and position of a virtual vortex, was employed. The strength of the virtual vortex was then related to the lift coefficient of the cylinder. Results obtained for a steadily rotating cylinder (no forced oscillations) compare favorably with similar data published in the literature. It was also found that the addition of forced rotary oscillations to the steady rotation of the cylinder helped to increase the lift coefficient in the cases where the wake would normally be separated in the steadily rotating case, and decrease it otherwise.

It is believed that this is the first investigation of the flow past a cylinder with both net rotation and oscillations.

1.3 A note on the transport of vorticity about the cylinder

The concept of separation is useful because it gives an intuitive feel for the transport of vorticity into a flow. For the generic case of flow about a bluff body in steady uniform flow, the vorticity is shed into the wake from "slowly" moving separation points. It might be appropriate to call this kind of separation *quasi-steady*. In contrast, when a body is accelerated in rotation, or translation, as in the present experiments, separations can appear, move, and disappear over length and time scales comparable those of the body motion and the surrounding flow. In the latter case it is even difficult to define "separation".

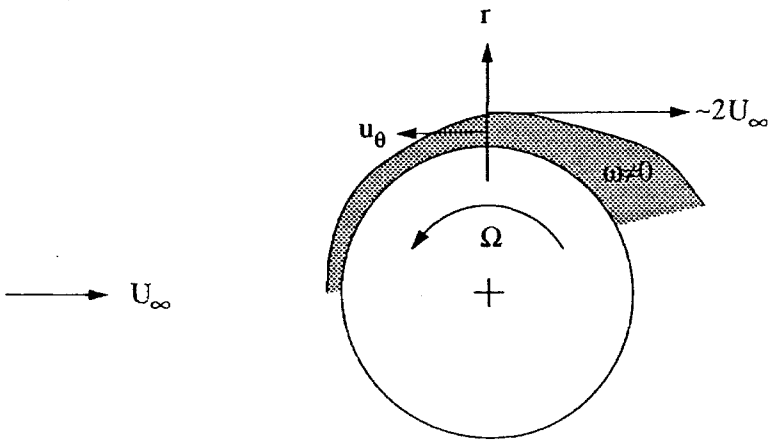

FIG. 1.2 Flow past a cylinder.

An *ad hoc* approach is to examine the transport of vorticity close to the body. In particular, for the case of a circular cylinder, the convective vorticity flux across

a θ = constant ray (traversing the boundary layer) can be written as

$$J = \int_a^{\delta} \omega\, u_\theta \, dr \ , \tag{1.3.1}$$

where δ is the boundary layer thickness. In dimensionless form

$$\frac{J}{\frac{1}{2}U_\infty^2} = 2 \int_1^{\delta/a} \frac{a\omega\, u_\theta}{U_\infty^2} \, d\left(\frac{r}{a}\right) \ . \tag{1.3.2}$$

If the vorticity in the boundary layer can be approximated by

$$\omega \approx \frac{\partial u_\theta}{\partial r} \tag{1.3.3}$$

then Eq. 1.3.2 can be approximated by

$$\frac{J}{\frac{1}{2}U_\infty^2} \approx \left(\frac{u_\theta(\delta/a)}{U_\infty}\right)^2 - \left(\frac{u_\theta(1)}{U_\infty}\right)^2 \ . \tag{1.3.4}$$

Looking at the vorticity convected in the boundary layer at $\theta = 90°$ gives an indication of the vorticity convected into the (dead water) region behind the cylinder. See Fig. 1.2.

Consider the case of a cylinder executing rotary oscillations with no mean rotation rate. The potential flow model for the flow past a circular cylinder has

$$u_\theta = -2U_\infty \quad \text{at} \quad 90° \ , \tag{1.3.5}$$

which is close to the velocity outside the boundary layer in the real case. Using Eqs. 1.3.5, 1.2.2, and 1.2.1 with $\Omega_0 = 0$ (no mean rotation rate) then yields for the vorticity convected past the 90° point,

$$\frac{J(\theta = 90°)}{\frac{1}{2}U_\infty^2} \approx 4 - \Omega_1^2 \sin^2(2\pi f t) \ . \tag{1.3.6}$$

Hence *any* rotary oscillation of the cylinder will tend to decrease the convection of vorticity past the 90° point. Note that when

$$\Omega_1^2 \sin^2(2\pi ft) \;=\; 4\;, \tag{1.3.7}$$

(instantaneously) *no* vorticity is convected past the 90° point as would be the case in potential flow. Equation 1.3.7 suggests that a value of

$$\Omega_{1_{\min}} \;=\; 2 \tag{1.3.8}$$

may be needed to effectively control this flow.

If, on average, no vorticity is to be convected past the 90° point, then Ω_1 will satisfy

$$\Omega_1 \;\approx\; 2\sqrt{2} \;\approx\; 2.8\;. \tag{1.3.9}$$

It is shown (experimentally) in Ch. 3 that $(S_f, \Omega_1) \approx (1,3)$ marks the minimum wake displacement thickness in the (S_f, Ω_1)-parameter space.

CHAPTER 2

Experimental facilities

2.1 Flow facility

The initial phase of the current experiments, *i.e.*, wake mean velocity measurements and preliminary flow visualization, was carried out in the 18″ wide by 19″ deep Low Speed Water Channel (LSWC) located in the basement of Guggenheim.* Subsequent flow visualization and lift measurements were preformed in the 20″×20″ Free Surface Water Tunnel (FSWT) in the Hydrodynamics Lab. See Ward (1976).

2.2 The cylinder apparatus

The cylinder support structure, Fig. 2.1, holds a cylinder 10″ above the bottom of the water channel, between 0.5″ thick Plexiglas fairings placed flush to the side walls of the channel. Power is transferred from the motor to the cylinder using steel reinforced neoprene timing belts. They are entirely enclosed in the fairings and do not interfere with the flow, *cf.* Figs. 2.1 and 2.2.

---

* Also known as "The Student Channel."

When choosing a motor and cylinder diameter, the minimum design goal was to be able to oscillate the cylinder with peak rotational rates greater than $\Omega_1 = 2$ (as discussed in Sec. 1.3) and at Reynolds numbers around $Re = 10^4$. It was felt that frequencies an order of magnitude faster than the natural (unforced) shedding frequency would be fast enough ($S_f \approx 2$). In addition, a five times "engineering" factor was used.

The cylinders were driven by a high performance JR16M4CH ServoDisc^{tm} DC motor, from PMI Motion Technologies, capable of tracking an arbitrary command signal, within the bandwidth and slewing rates that were investigated. This command signal was generated by a function generator, or a computer digital-to-analog converter output channel. In addition, the angular position of the cylinder could be monitored through a 13-bit M25 Series absolute position encoder from BEI Motion Systems Co.

Cylinders with a radius ranging from $0.25''$ to $2''$ and span from $17''$ to $19''$ were used. Cylinders were made out of both anodized aluminum and Plexiglas. Two $2''$ radius cylinders were used in the present experiments. One was made of smooth anodized aluminum tubing. The other was made of machined Plexiglas tubing equipped with ports so that dye could be introduced into the flow from the cylinder surface. Additional flow visualization was accomplished by introducing dye upstream of the cylinder, through hypodermic tubing.

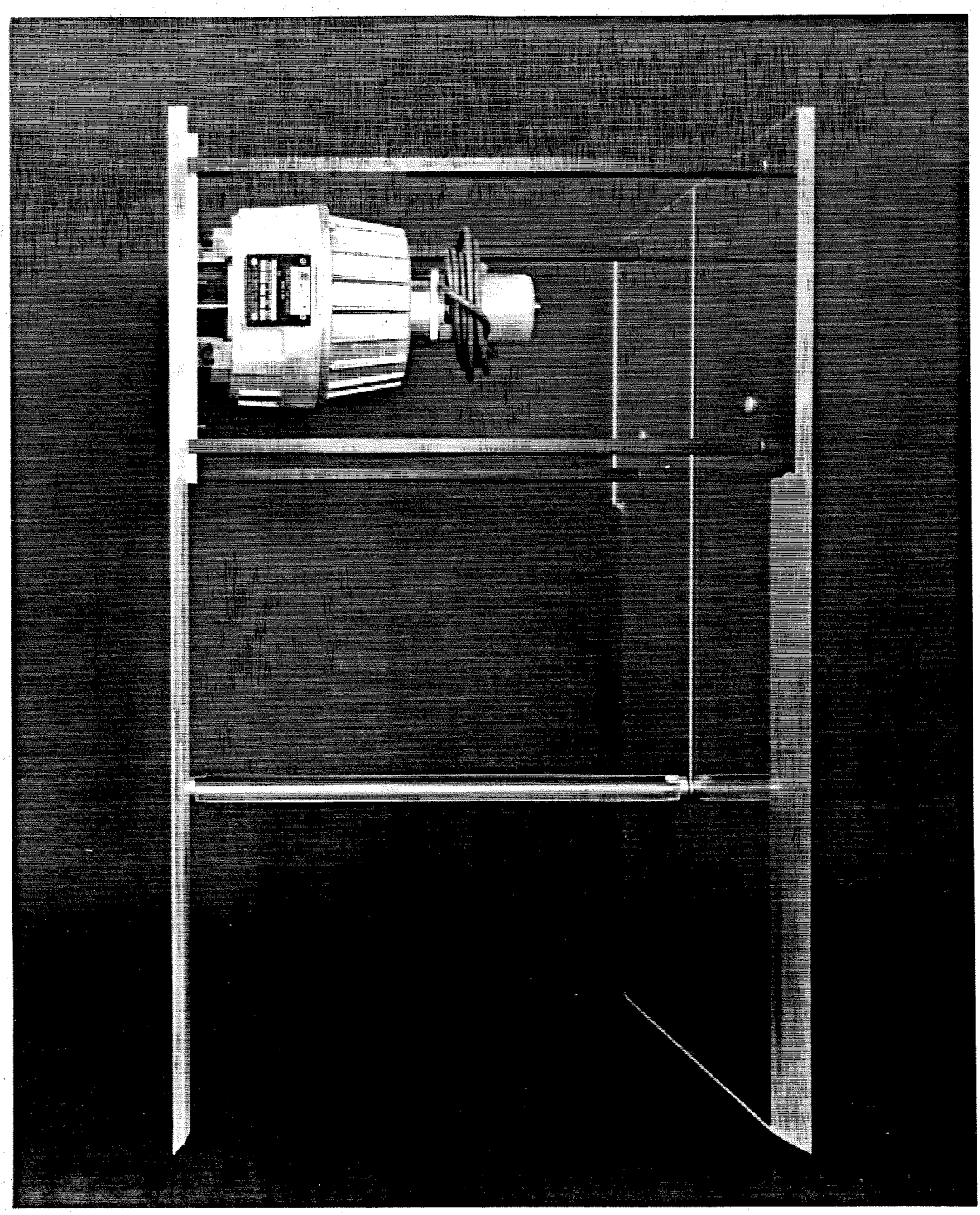

FIG. 2.1 The cylinder apparatus.

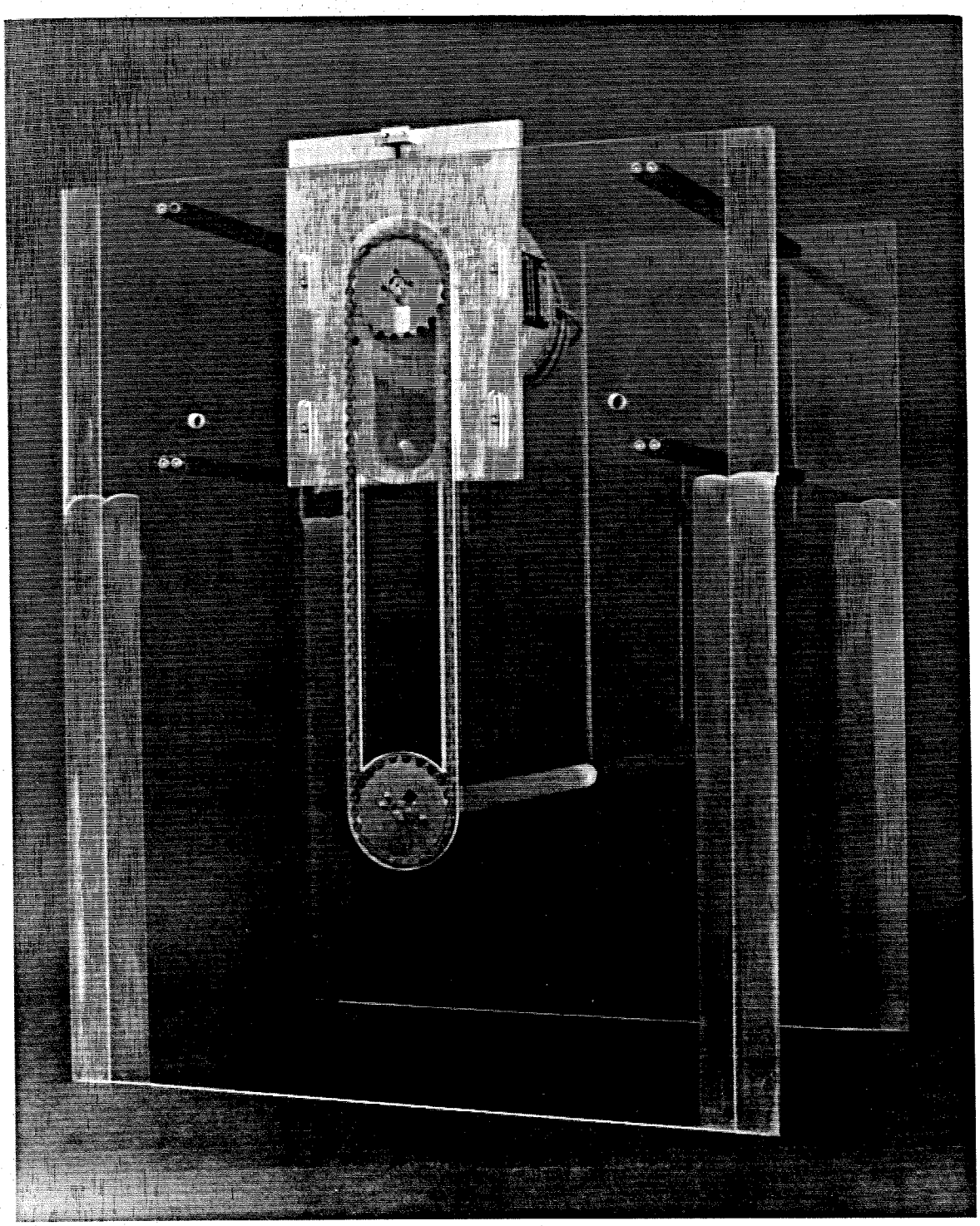

FIG. 2.2 The cylinder drive mechanism.

2.3 Measurement apparatus

Measurements were made using a number of laser Doppler velocimetry systems. More details are given in the "experimental setup" sections for each chapter. In the LSWC a u-channel Bragg cell frequency-shifted He-Ne based system was used. Translation of the LDV (and measurement volume) was effected by a manual x-y traverse system.

In the FSWT u, (u,v), and v_θ, Argon-ion based systems, derived from the LDV system of Lang (1985) were used. All but the u in the (u,v) arrangement, were Bragg cell frequency-shifted. Translation of the LDV was performed by a digital x-y-z traverse, and rotation of the focal volume for the v_θ measurements was effected by a rotatable dove prism.

The data were gathered using LSI-11 data acquisition computers, and then transferred to DEC VAX, Apple Macintosh, and NeXT NeXTstation computers for further reduction and presentation.

CHAPTER 3

Non-lifting cylinder

3.1 Preface

This chapter describes exploratory experiments, performed on circular cylinders executing rotary oscillations, in a steady uniform flow. Flow visualization data were used to characterize the wake structure and to estimate the convection speed, spacing, and strength of the vortical structures. In addition, LDV measurements were made to estimate the cylinder drag coefficient and wake displacement thickness. The data show that a considerable amount of control can be exerted over the flow by such means. In particular, a large increase, or decrease, in the resulting displacement thickness, estimated cylinder drag, and associated mixing with the free stream can be achieved, depending on the frequency and amplitude of oscillation. See also Tokumaru & Dimotakis (1991).

3.2 Experimental setup

For the experiments detailed in this chapter, Ω_0 was set to zero and Ω_1 was chosen such that within the range of parameters examined, the peak circumferential velocity of the cylinder would be comparable to the velocity just outside the boundary layer of the cylinder (approximately twice the free-stream velocity). It was anticipated that amplitudes of this magnitude, or greater, would be necessary to effect a significant change in the flow, as was discussed in Sec. 1.3.

The experiments presented in Secs. 3.3 and 3.4 examine the control parameters Ω_1 and S_f over a range of values. The free-stream velocity was approximately 15 cm/s, yielding a Reynolds number based on cylinder diameter of $Re = 1.5 \times 10^4$. In addition, wake mean and rms velocity profiles were measured at a single streamwise station, located 4.5 diameters downstream of the cylinder axis. The remaining sections in this chapter touch on some other issues pertaining to the present experiments.

The wake streamwise mean velocity measurements were performed in the GALCIT 18″ wide by 19″ deep Low Speed Water Channel, using a He-Ne based laser Doppler velocimeter (LDV). The cylinder used for the wake velocity measurements is an anodized and machined aluminum tube, 4″ in diameter, and mounted and driven by the apparatus described in Ch. 2. The command signal for the cylinder velocity was generated by a computer controlled function generator.

The (15 mW He-Ne) laser beam for the LDV velocity measurements was split into two beams of nearly equal intensity using a cube beam splitter. The beams were then Bragg cell frequency-shifted to accommodate flow reversals. The Bragg cell offset between the two beams was 100 to 200 kHz for the data presented in

this chapter. An achromat was used to focus the beams in a focal (measurement) volume located in the midspan plane of the LSWC. The light scattered from the focal volume was gathered by an achromat and focused on a photodiode with an integral low noise pre-amplifier designed by Dan Lang. The signal from the pre-amplifier was then band-pass filtered above and below the frequency corresponding to the mean flow velocity. The band-pass range was chosen to pass instantaneous velocity fluctuations. A tracking phase-locked loop designed by Dan Lang and Paul Dimotakis was then used to lock a TTL square wave to the dominant frequency. The TTL signal was then read by a counter-timer board on a data acquisition computer and stored on disk for later processing. The transmitting and receiving hardware was mounted on a manual x-z traverse (positioner).

Photographs were taken in the GALCIT $20'' \times 20''$ Free Surface Water Tunnel (FSWT) using a 35mm camera. Red dye was used in all figures except for Fig. 3.1. A blue filter was used (except for Fig. 3.1) to darken the red dye marker relative to the white background. Illumination was provided from behind by a large (backlit) white sheet of paper, suspended outside of the tunnel, behind the model. The cylinder used for the flow visualization data is a machined Plexiglas tube, $4''$ in diameter. Holes for introducing dye into the flow were drilled through the surface at midspan. Additional flow visualization was accomplished by introducing dye through hypodermic tubing into the flow ahead of the cylinder. The cylinder was mounted and driven by the apparatus described in Ch. 2. The command signal for the cylinder velocity was generated by a computer-controlled function generator.

3.3 Flow visualization

A useful picture of the control that can be exercised over the separated flow in the wake of the cylinder emerges from the flow visualization data. These demonstrate the overall narrowing, or widening, as well as the formation of distinct vortical structures in the wake, depending on the values of the control parameters S_f and Ω_1.

In Fig. 3.1, dye is introduced ahead of the cylinder by a comb of dye injectors. In the unforced case (Fig. 3.1, top), the dye can be seen to be dispersed and mixed across the full height of the test section, within a few diameters downstream of the cylinder. In contrast, the dye marker in the forced case, corresponding to a reduced wake width (Fig. 3.1, bottom), occupies approximately the same fraction of the test section height on exit as it did entering.

The data in Fig. 3.2 and Fig. 3.5 (recorded with dye issuing from the surface of the cylinder) illustrate how the wake may be made wider, or narrower, depending on the control parameters S_f and Ω_1. Weihs (1972) examined this phenomenon by considering the mutual influence of the vortices in the wake and those being shed. Although his analysis is highly idealized, considering only point vortices in potential flow, it does provide a physical argument for the various trajectories taken by the vortices. Additional flow visualization data (also recorded with dye issuing from the surface of the cylinder), at fixed $\Omega_1 = 8$ and increasing S_f, are depicted in Fig. 3.6 and Fig. 3.7.

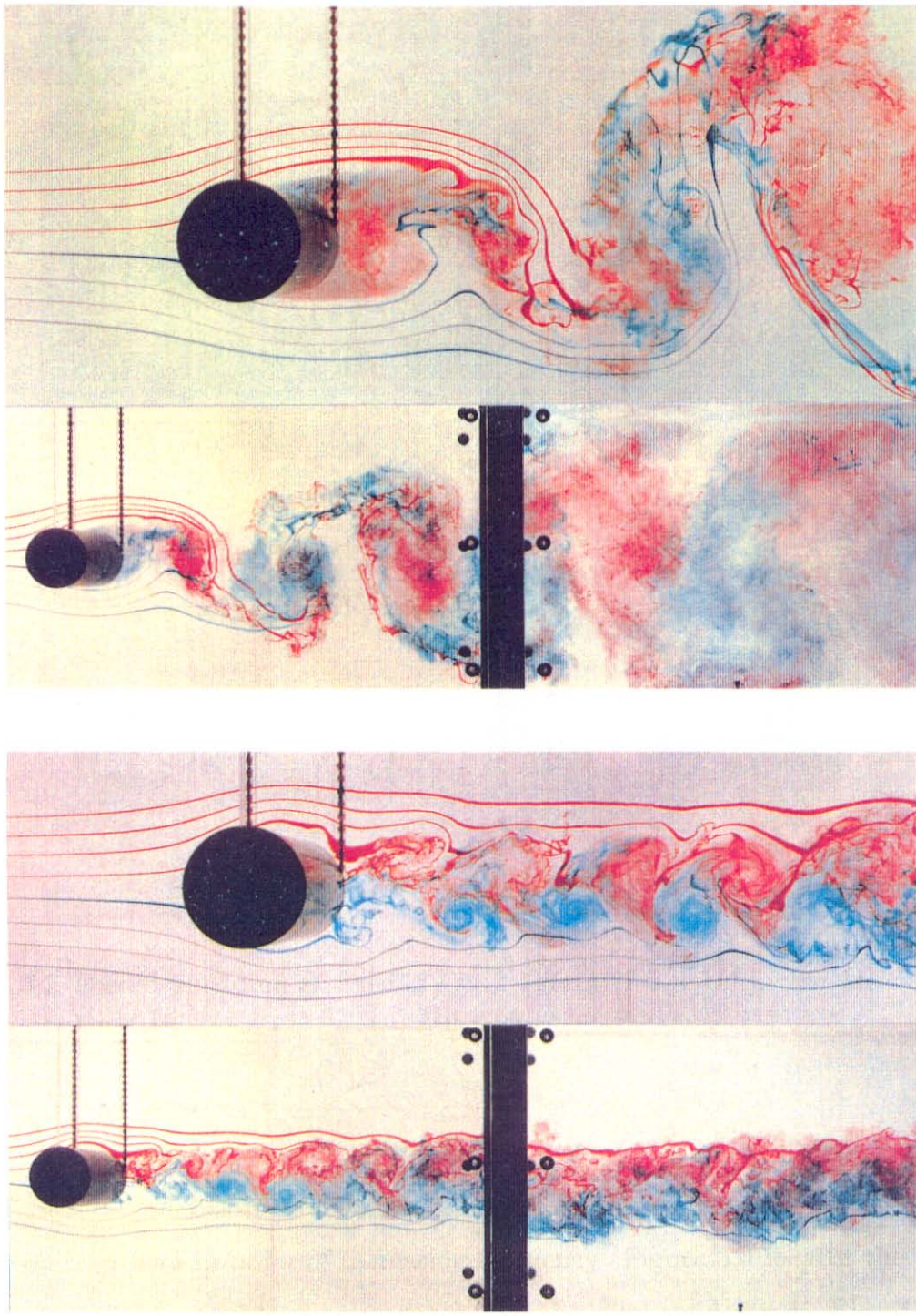

FIG. 3.1 Closeup and full flow visualization views with and without active control. Top pictures: Unforced (non-rotating) cylinder in uniform flow; bottom pictures: $S_f \approx 1$, $\Omega_1 \approx 3$.

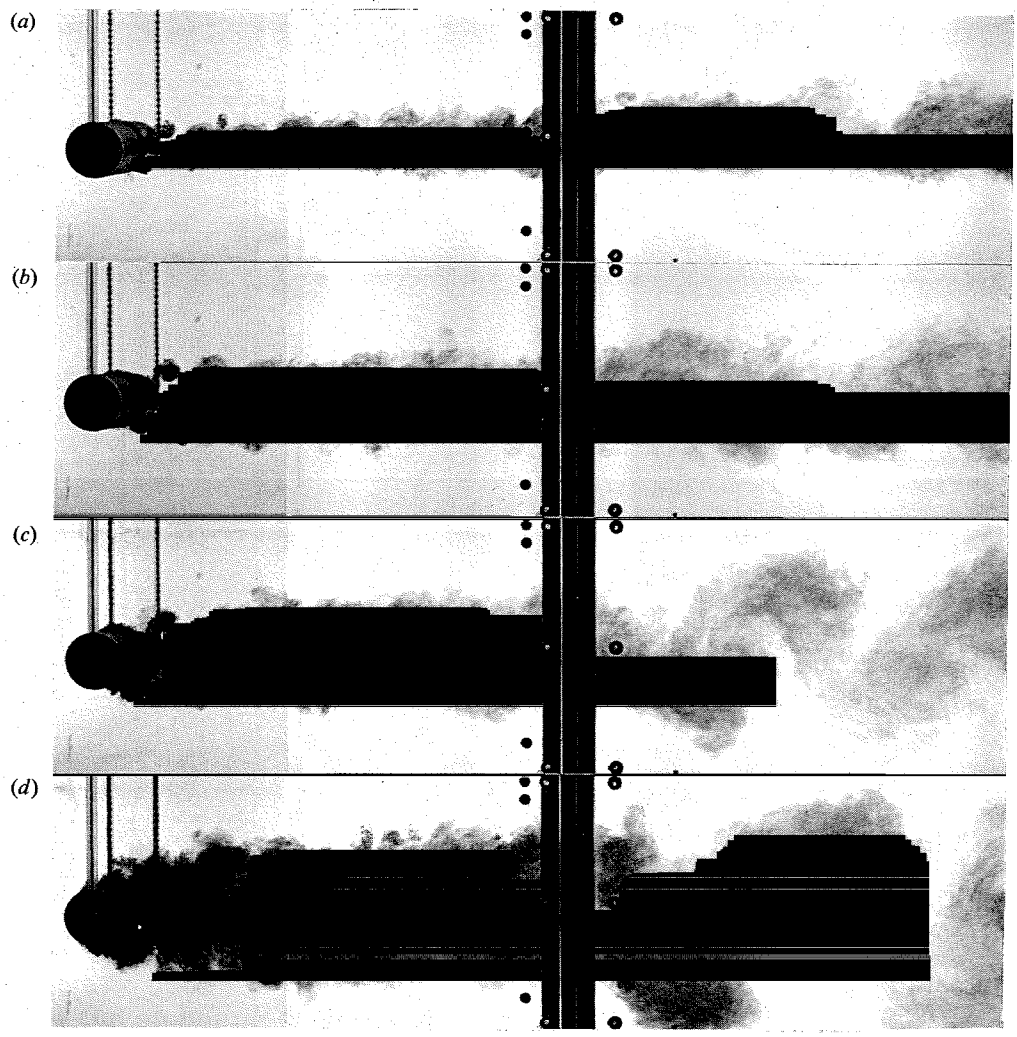

FIG. 3.2 Forced shedding at fixed $S_f = 1$ ($Re = 1.5 \times 10^4$). (a) $\Omega_1 = 8$, (b) $\Omega_1 = 16$, (c) $\Omega_1 = 32$, (d) $\Omega_1 = 64$.

3.3.1 Wake structure

Several, qualitatively different, vortex shedding modes were observed. They are presented here in order of increasing frequency. Figure 3.3 locates the various modes in the (S_f, Ω_1)-parameter space. In the dual mode (*e.g.*, Fig. 3.4), the cylinder releases two vortices of the same sign per half-cycle. This mode was not easy to set up and should not be considered robust enough for use in active program control.

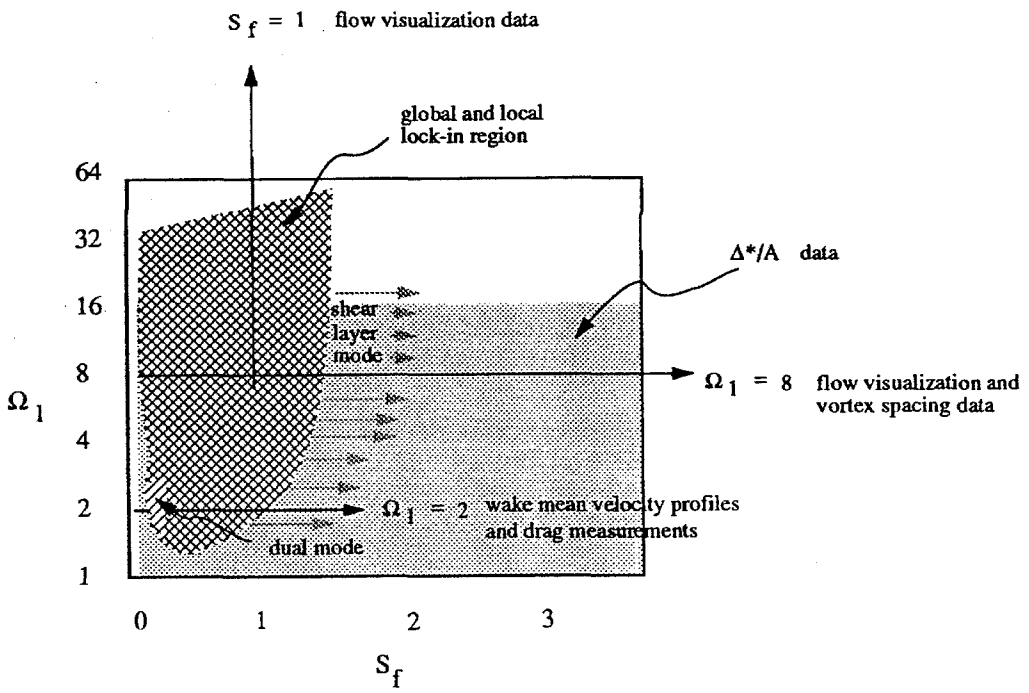

FIG. 3.3 Location of figures in the (S_f, Ω_1)-parameter space.

In the global mode (*e.g.*, Fig. 3.5), the wake structure is synchronized with the forced cylinder oscillation, and persists beyond the end of the test section. This mode was relatively easy to set up because it occurred over a wide range of forcing parameters. In the local mode (*e.g.*, Fig. 3.6), the near wake structure is synchronized, but becomes unstable and evolves into a structure with lower spatial frequency some distance downstream of the cylinder. In the shear layer mode (*e.g.*, Fig. 3.7), the wake structure is not synchronized with the forcing. The effect of forcing is primarily observed in the shear layers separating from the cylinder. Note that while the flow visualization photographs of the forced cylinder wake at the largest values of S_f (*cf.* Fig. 3.7, bottom) resemble those for the unforced case (*cf.* Fig. 3.8), it was found that the wake displacement thickness (Eq. 3.4.2) in these forced cases is still noticeably less than in the unforced case.

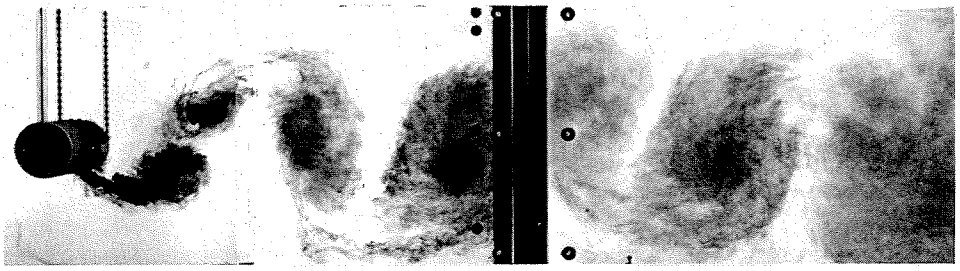

FIG. 3.4 Dual shedding: Forced shedding of two same sign vortices during a half forcing cycle, $S_f = 0.2$, $\Omega_1 = 2$, $Re = 1.5 \times 10^4$.

The transition between the global and shear layer modes occurs gradually through the local mode. Figures 3.5 to 3.7 demonstrate how the "break-up" of the synchronized structure in the local mode moves toward the cylinder with increasing S_f. The shear layer mode is then found, at even higher S_f, when none of the wake structure (save small perturbations of the separating shear layers) is shed synchronously with the forcing. This "break-up" in the flow structure in the local and shear layer modes may be attributable to the stability characteristics of the evolving mean velocity profiles (as suggested by Cimbala, Nagib & Roshko 1988, for lower Reynolds number flows, far downstream), vortex coalescence, three-dimensional effects, or some combination thereof.

Behavior similar to the dual, global, and local modes was previously observed by Roberts (1985) and Roberts & Roshko (1985) for the case of a forced wake behind a splitter plate, and Williamson & Roshko (1988) for a cylinder executing transverse oscillations in a free stream, for example.

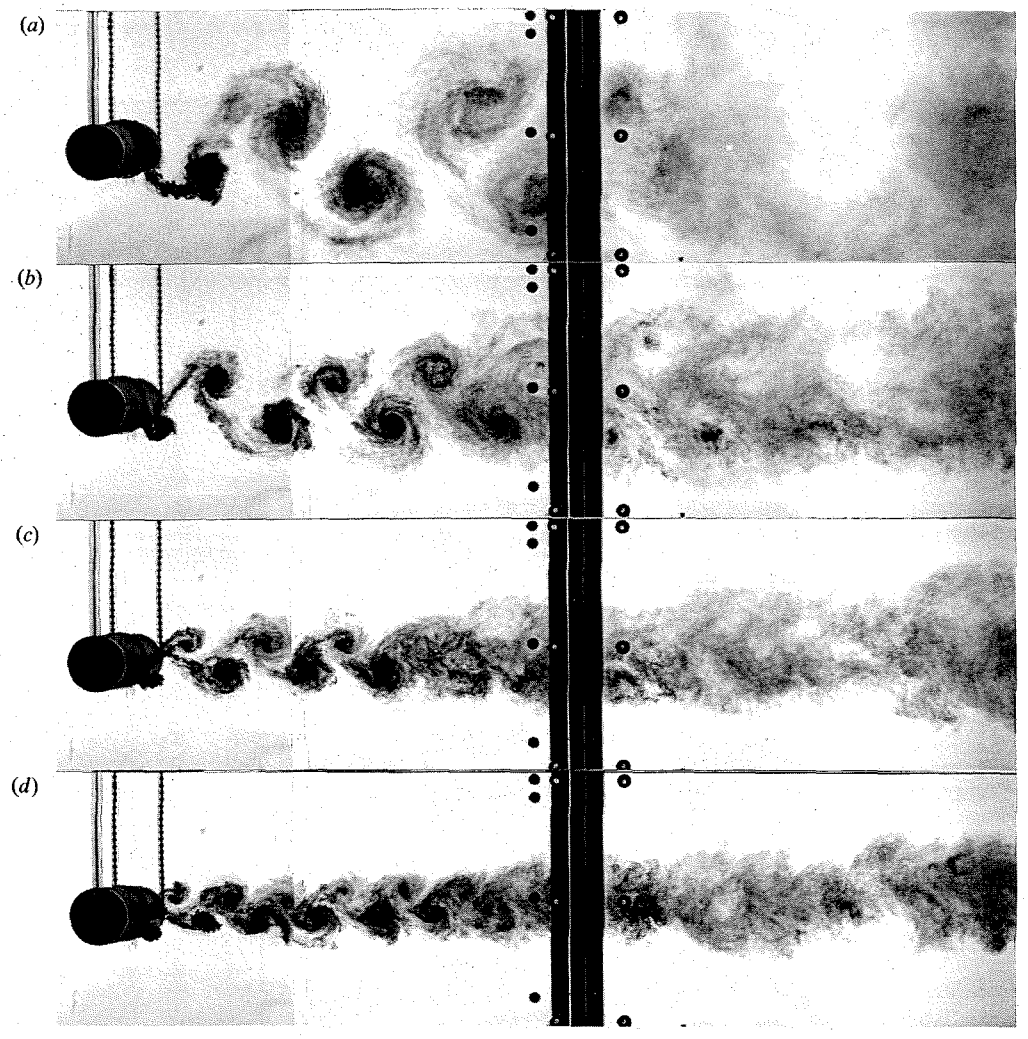

FIG. 3.5 Global locking: Global wake structure is synchronized with the forcing frequency. (a) $S_f = 0.3$, (b) $S_f = 0.5$, (c) $S_f = 0.7$, (d) $S_f = 0.9$. ($\Omega_1 = 8$, $Re = 1.5 \times 10^4$).

3.3.2 Speed and spacing of the vortical structures

Flow visualization techniques are usually considered only for qualitative analysis of flow fields. In the present experiments, however, estimation of the normalized speed (celerity) of the vortical structures relative to the cylinder, $u_v \equiv f\ell_x$, divided by the free-stream velocity,

$$\lambda_x \equiv \frac{f\,\ell_x}{U_\infty} = S_f\,\frac{\ell_x}{2\,a}\,, \tag{3.3.1}$$

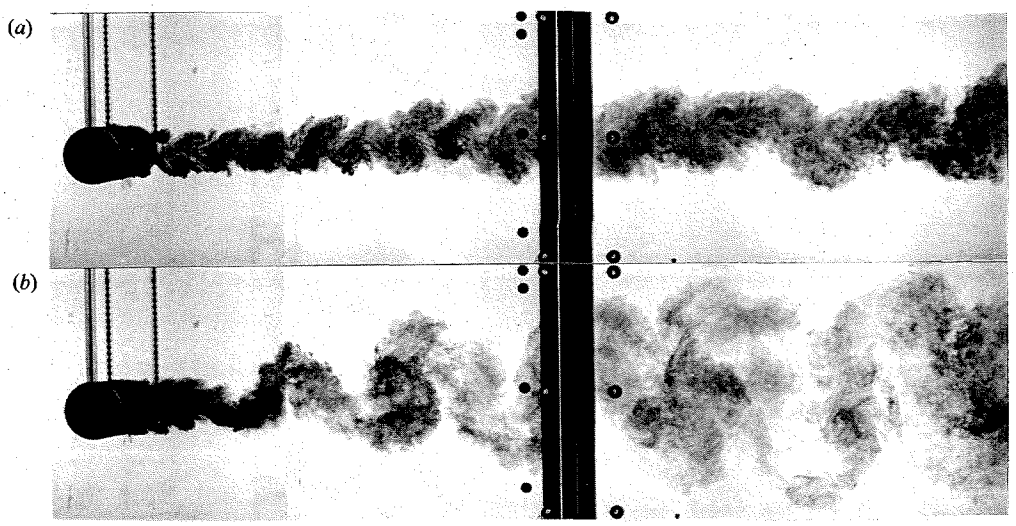

FIG. 3.6 Local locking: Local wake structure is synchronized with the forcing frequency. (a) $S_f = 1.1$, (b) $S_f = 1.5$, ($\Omega_1 = 8$, $Re = 1.5 \times 10^4$).

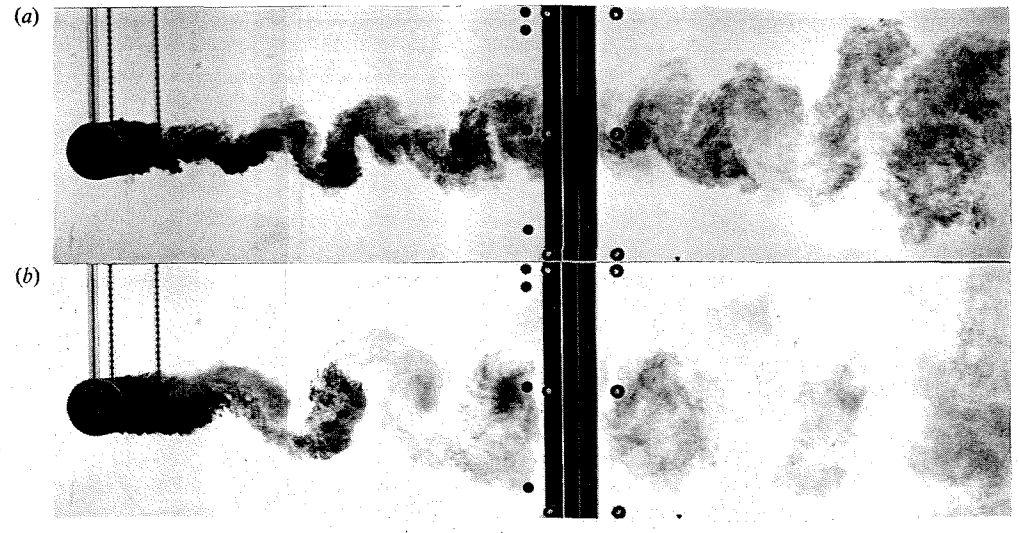

FIG. 3.7 Shear layer forcing: (a) $S_f = 2.0$, (b) $S_f = 3.3$. ($\Omega_1 = 8$, $Re = 1.5 \times 10^4$).

was straightforward, since S_f was known *a priori* and the ratios of the vortex spacing to the cylinder diameter, $\ell_x/2a$ and $\ell_y/2a$, could be obtained from photographs like those in Figs. 3.5 to 3.7. See Fig. 3.9. This analysis assumes that the dye marks the centers of the vortical structures. The normalized celerity, λ_x, is also estimated

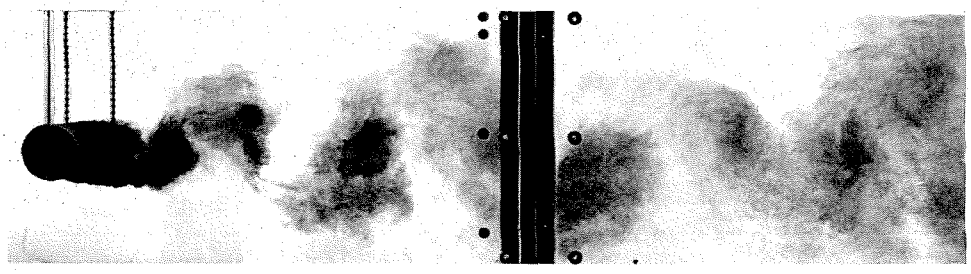

FIG. 3.8 Natural (unforced) shedding. Flow visualized with dye issuing as in Fig. 3.2 - Fig. 3.8.

in Sec. 4.3, p. 4.18, for a particular forced case, using LDV measurements. While λ_x is the normalized celerity of the vortical structures, averaged over one forcing cycle, it is also the spacing, normalized by the distance moved by the flow in one forcing cycle. The normalized transverse spacing is analogously defined as

$$\lambda_y \equiv \frac{f\,\ell_y}{U_\infty} = S_f\,\frac{\ell_y}{2\,a}\,. \tag{3.3.2}$$

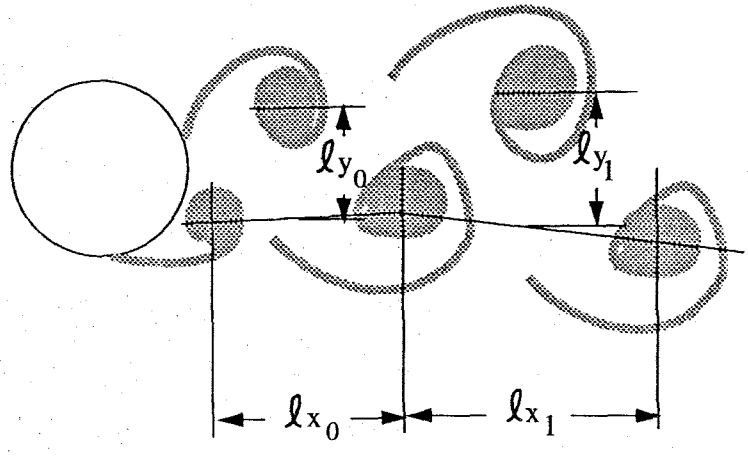

FIG. 3.9 Diagram of $(\ell_x)_0$, $(\ell_x)_1$, $(\ell_y)_0$, and $(\ell_y)_1$.

Note that a negative value of λ_x is unphysical as it indicates vortical structures moving ahead of the cylinder. Similarly, a value of $\lambda_x > 1$ is also unlikely for a wake, since it corresponds to vortical structures moving downstream faster than the free-stream velocity ahead of the cylinder. In a finite test section, however, blockage effects result in a local free-stream velocity, U_0, measured above and below the wake, that is somewhat higher than U_∞. Hence, it is not impossible for λ_x to be somewhat greater than 1.

Figures 3.10 and 3.11 shows the variation of λ_x and λ_y with S_f, just behind the cylinder. The spacing for the first two forcing periods, nearest the cylinder, are shown. The squares in these figures denote the spacing for the first pair of vortical structures, directly behind the cylinder. The circles denote the second pair. The vertical lines mark the range. The dashed vertical lines indicate where there was a rapid contraction of the spacing, because the vortical structures were being "rolled" into larger lower spatial frequency structures. This rapid contraction is not evident at the highest values of S_f, because the roll up does not occur until several more forcing periods downstream of the cylinder.

Note the decrease in λ_x around $S_f = 1$. This change is reminiscent of Tritton's (1959) high-speed and low-speed vortex shedding modes. In the global mode the vortex structures move downstream quickly (*cf.* Tritton's high-speed mode) and in the local mode the structures move downstream more slowly (*cf.* Tritton's low-speed mode). It should be noted, however, that because of the finite test section height, a larger wake displacement thickness, especially at the lower values of S_f, can exaggerate the speed of the vortical structures relative to the cylinder. It is tempting, anyway, to associate the instability in the wake structure observed above $S_f \sim 1$ with the decreased initial speed of the vortices.

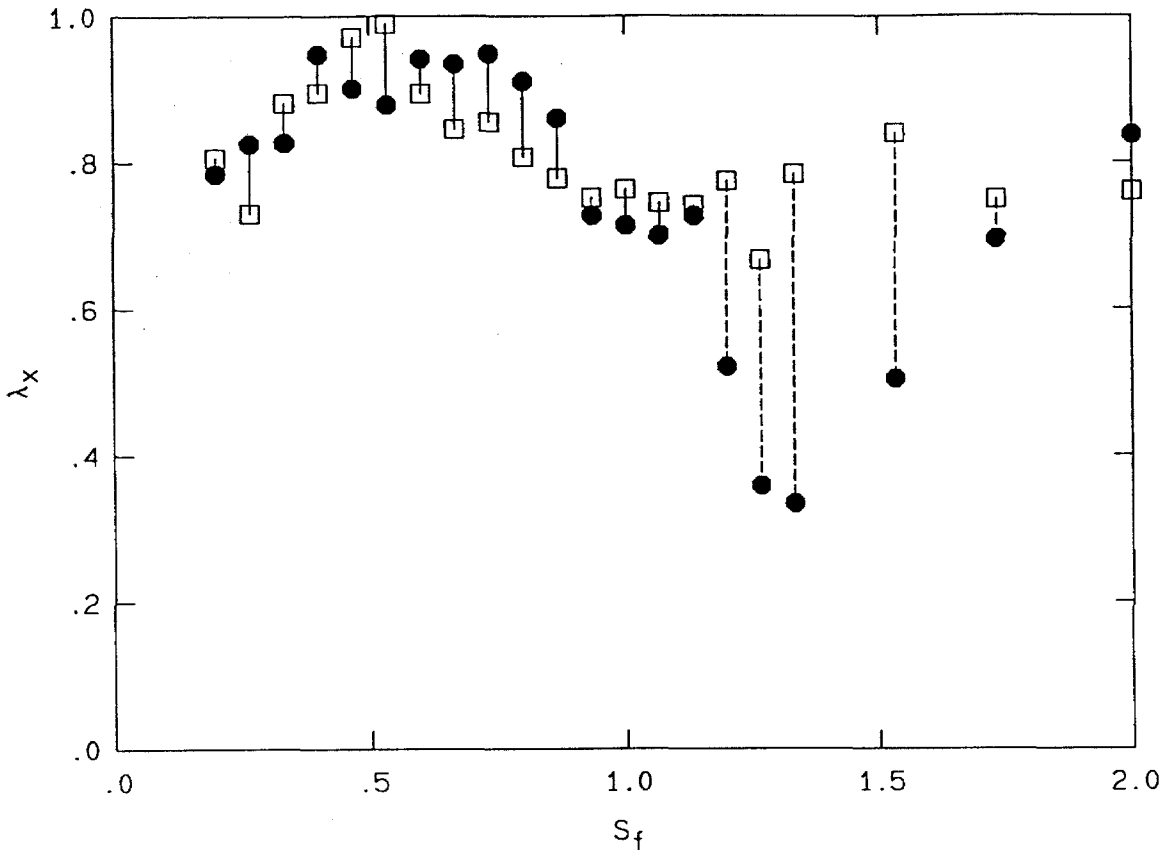

FIG. 3.10 Variation of initial λ_x with S_f ($\Omega_1 \approx 8$). Squares: λ_x for the first pair of structures, circles, for second pair.

Figure 3.12 shows the variation of the spacing ratio,

$$\frac{\lambda_y}{\lambda_x} = \frac{\ell_y}{\ell_x} ,$$

with S_f. The squares in Fig. 3.12 denote the initial spacing ratio, $(\lambda_y/\lambda_x)_0$, the circles, the spacing ratio one period farther downstream, $(\lambda_y/\lambda_x)_1$. Weihs (1972) suggested that, to first order behavior, the wake would become narrower, or wider, depending on the initial spacing ratio. For the data in Fig. 3.12, the "neutral" value of $(\lambda_y/\lambda_x)_0$, *i.e.*, when $(\lambda_y/\lambda_x)_0 = (\lambda_y/\lambda_x)_1$, which marks the switch from a "widening" wake, $(\lambda_y/\lambda_x)_0 < (\lambda_y/\lambda_x)_1$, to "narrowing" one, $(\lambda_y/\lambda_x)_0 > (\lambda_y/\lambda_x)_1$, occurs around $(\lambda_y/\lambda_x)_0 = (\lambda_y/\lambda_x)_1 = 0.41$ ($S_f \approx 0.6$). Perhaps related to the

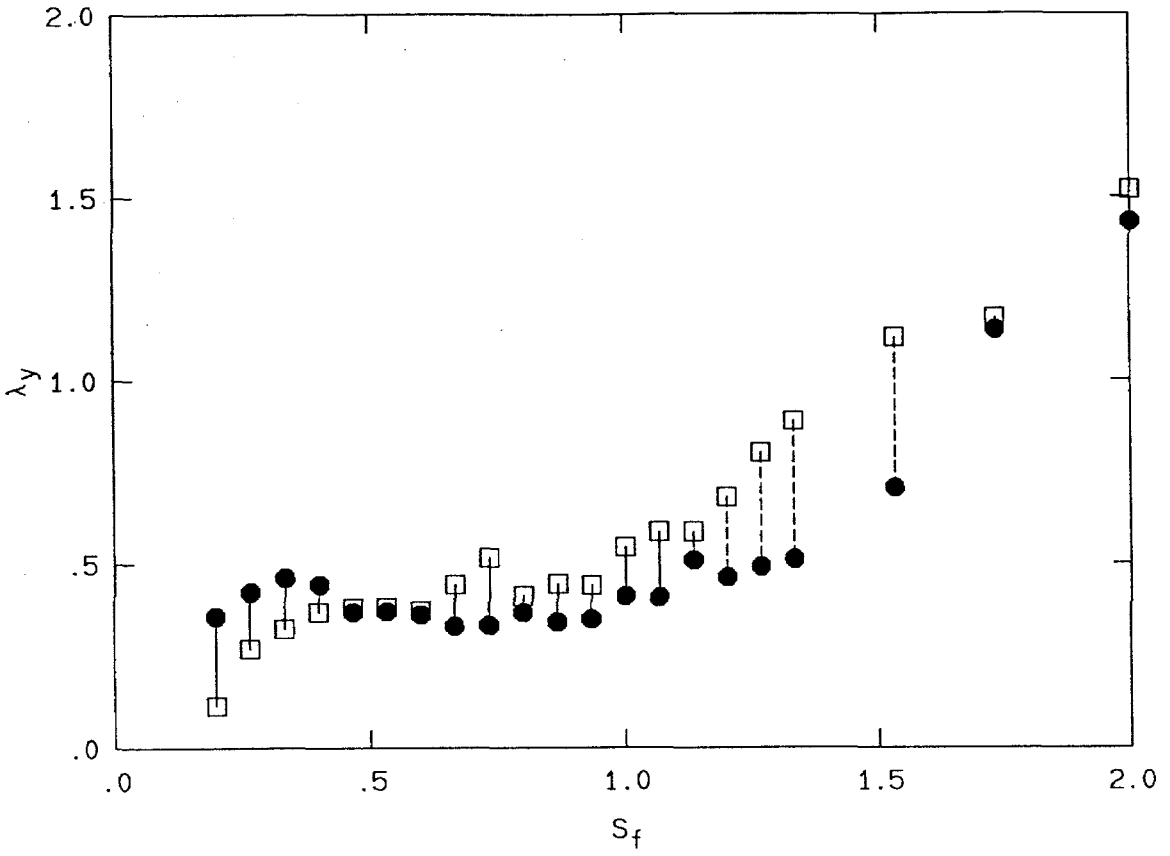

FIG. 3.11 Variation of initial λ_y with S_f ($\Omega_1 \approx 8$). Squares: λ_x for the first pair of structures, circles, for second pair.

switch in $(\lambda_y/\lambda_x)_0$ at $S_f \approx 0.6$ is the coincidence of the value of the wake displacement thickness for the forced case and the unforced case. See Fig. 3.17, at $\Omega_1 = 8$. Around $(\lambda_y/\lambda_x)_0 = 0.85$ ($S_f \approx 1.2$), the data indicate a switch back from "narrowing" to "widening." This switch marks the center of the local mode, the division between the global and the shear layer modes. Note that the terms "widening" and "narrowing" refer to the *ratio* of the transverse and streamwise spacing of the vortical structures, not the absolute spacing. The spacing of the vortical structures was also measured at a fixed $x/a = 9$, downstream of the cylinder. Figure 3.13 shows the variation of the spacing of the structures, with S_f, for $\Omega_1 = 8$, and Fig. 3.14, for $\Omega_1 = 4$. The spacing of the forced vortical structures is not shown in the figure,

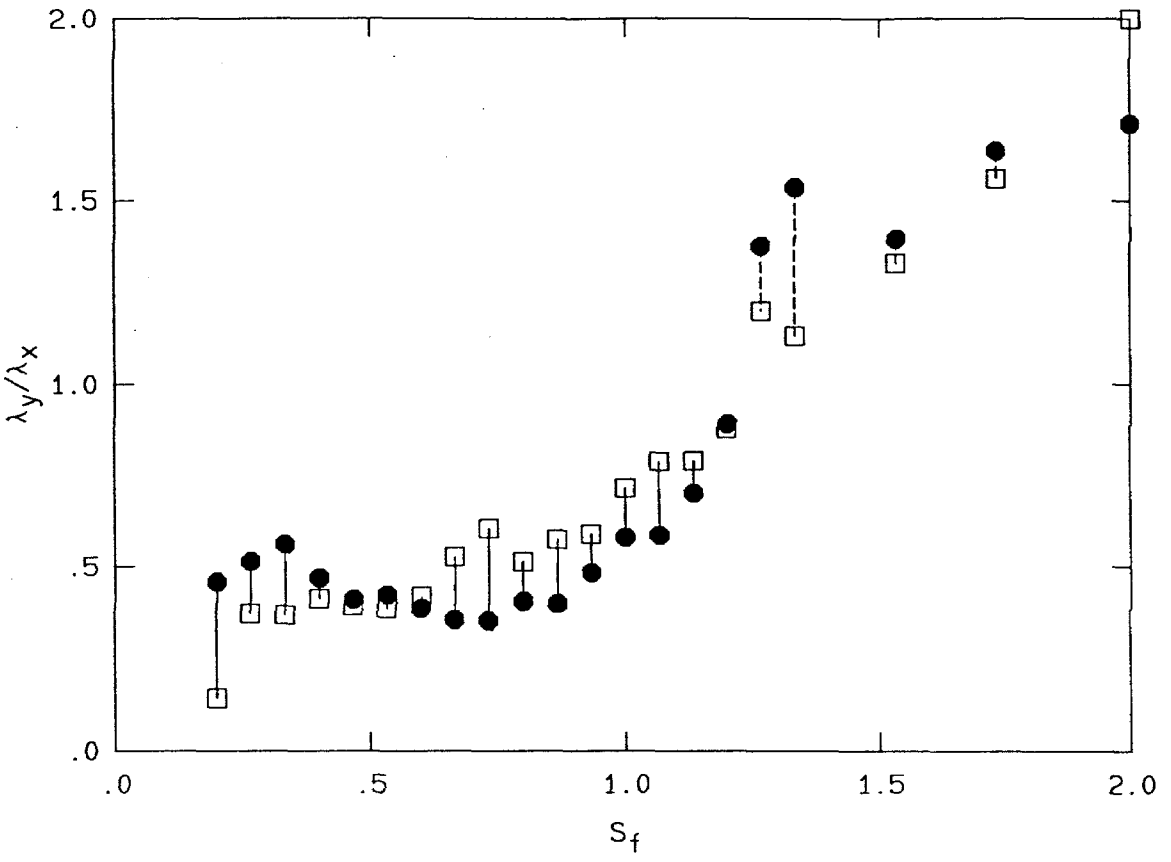

FIG. 3.12 Variation of initial ratio, λ_y/λ_x with S_f ($\Omega_1 \approx 8$). Squares: λ_y/λ_x for first pair of structures, and, circles, for the second pair.

for the higher values of S_f, because they were not discernible at $x/a \sim 9$.

Note that within the spread of the data, λ_x, λ_y, and λ_y/λ_x, at $x/a \sim 9$, seem to be constant over most of the range shown. They do seem to be a function of Ω, though. This suggests that, for a given Ω_1, the geometry of the wake structure is similar over that range. Note that the vertical spacing λ_y is depressed at the lower values of S_f. This is probably because of the finite test section height. In addition, the scatter in the data, especially in the $\Omega_1 = 4$ case, may be attributable to the subjective method of locating the centers of the vortical structures. For $\Omega_1 = 4$, the average values of λ_x, λ_y, and λ_y/λ_x were 0.96, 0.28, and 0.3 respectively. For

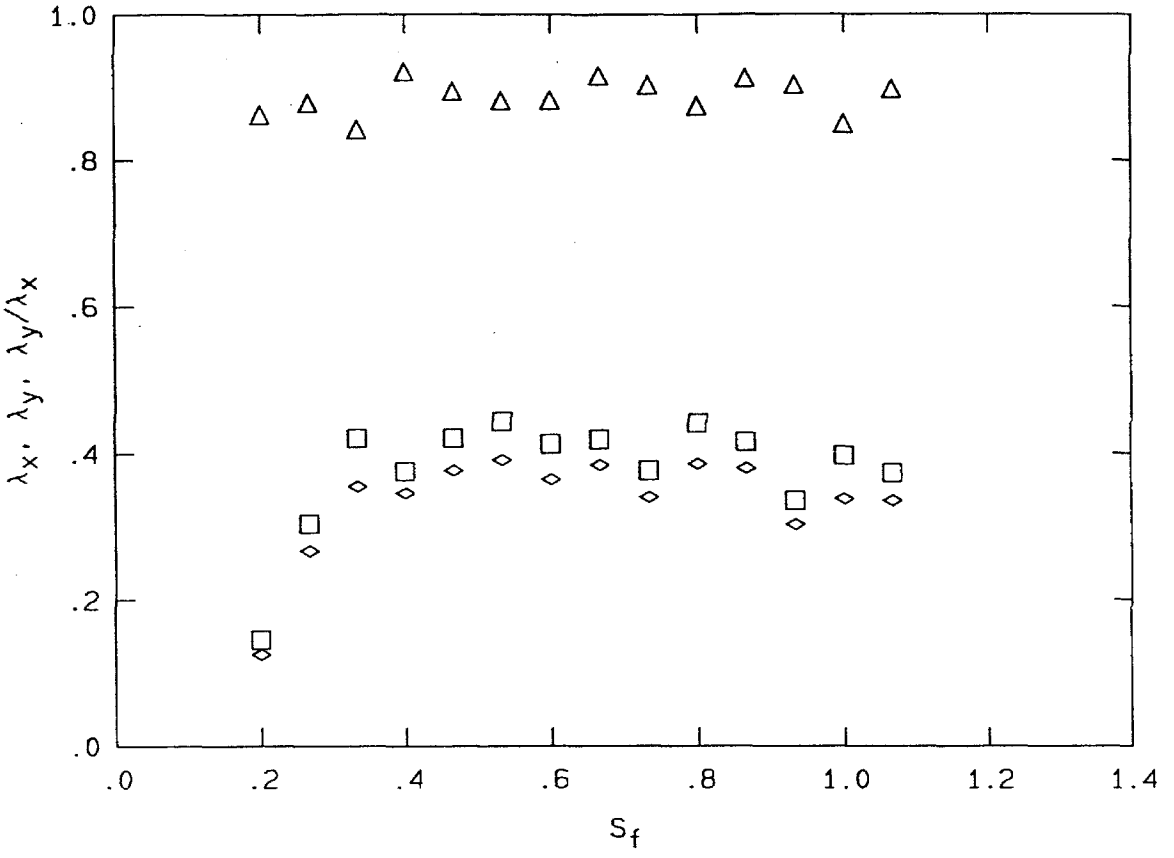

FIG. 3.13 Variation of λ_x, λ_y, and λ_y/λ_x with S_f at $x/a = 9$ with $\Omega_1 = 8$. Triangles: λ_x, squares: λ_y, and diamonds λ_y/λ_x.

$\Omega_1 = 8$, they were, 0.89, 0.37, and 0.41. Note that, at the same value of $\Omega_1 = 8$, the average value of λ_y/λ_x at $x/a = 9$ matches the "neutral" value of $(\lambda_y/\lambda_x)_0 = 0.4$ found earlier.

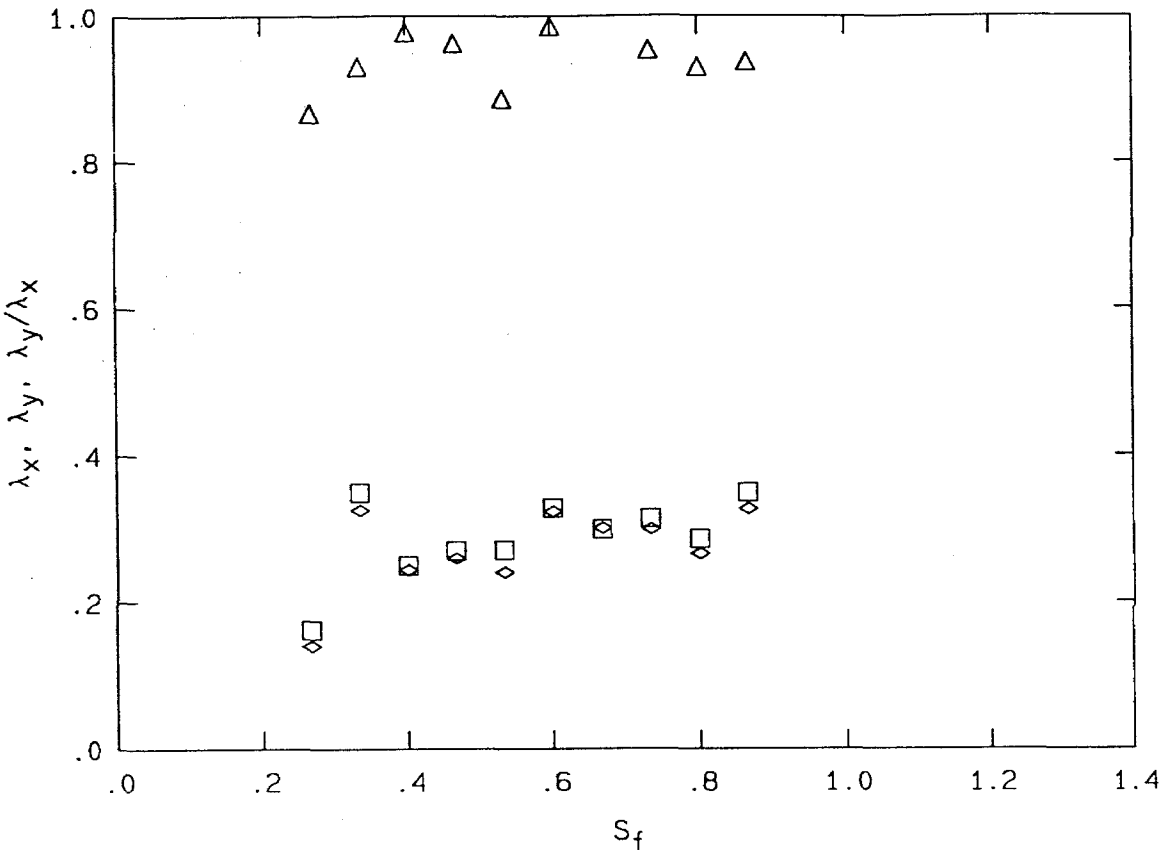

FIG. 3.14 Variation of λ_x, λ_y, and λ_y/λ_x with S_f at $x/a = 9$ with $\Omega_1 = 4$. Triangles: λ_x, squares: λ_y, and diamonds λ_y/λ_x.

3.3.3 A rough estimate of the vortex strength

A measure of the strength of the vortical structures in the wake can be obtained from their speed and spacing. A vortex street will have a self-induced velocity u_s, which will depend on the strength, Γ_v, and the streamwise and lateral spacing of vortical structures, ℓ_x and ℓ_y, and also on factors such as the presence of the cylinder, finite test section height, finite core size of the vortical structures, and viscous effects. See Goldstein (1938, §242-246) and Roshko (1954c) for similar estimates of the strength of vortical structures in a bluff body wake.

Using the potential flow model of a periodic vortex street,* of the strength of the vortical structures in the wake, it can be seen (*e.g.*, Goldstein 1938) that the strength per unit streamwise spacing of the vortical structures in the wake can be written as

$$\frac{\Gamma_v}{U_\infty \ell_x} = 2\frac{u_s}{U_\infty}\coth\left(\frac{\pi \ell_y}{\ell_x}\right) . \tag{3.3.3}$$

This expression is not valid at $\ell_y \equiv 0$, because when the structures are lined up, $u_s \equiv 0$ and Γ_v can be any value. In addition, u_s can be related to the velocity of the vortical structures, u_v, from Sec. 3.3.2, *i.e.*,

$$u_s \equiv U_0 - u_v = U_0 - f\,\ell_x . \tag{3.3.4}$$

U_0 varies with downstream position, and is not known *a priori*. Using continuity, however, and neglecting the core size of the vortical structures, U_0 can be written in terms of, Γ_v/ℓ_x, U_∞, and ℓ_y/h, *i.e.*,

$$U_0 = U_\infty + \frac{\Gamma_v}{\ell_x}\frac{\ell_y}{h} , \tag{3.3.5}$$

where h is the test section height. A little algebra, and the definitions for λ_x and λ_y, then yield

$$\frac{\Gamma_v}{U_\infty \ell_x} = 2\,\frac{1-\lambda_x}{\tanh\left(\frac{\pi\lambda_y}{\lambda_x}\right) - \frac{2\ell_y}{h}} . \tag{3.3.6}$$

Note that the singularity in this expression is directly related to the fact that the speed of the vortex street is zero for the case $\ell_y = 0$.

Figure 3.15 shows the variation of $\Gamma_v/U_\infty\ell_x$ with S_f. The dashed line in the figure is a plot of Eq. 3.3.6 assuming constant λ_x and λ_y. The rise in $\Gamma_v/U_\infty\ell_x$ at the lowest values of S_f could be an artifact of finite test section height effects, represented by the the ℓ_y/h term in Eq. 3.3.6. Similar plots for the $\Omega_1 = 4$ case were not interpretable, because the spread in the data was too large.

---

* Using such a model can only yield a relative measure of the strength of the vortices in the wake. See Sec. 4.3 for a better measure of the strength of the vortical structures, for a particular forced case.

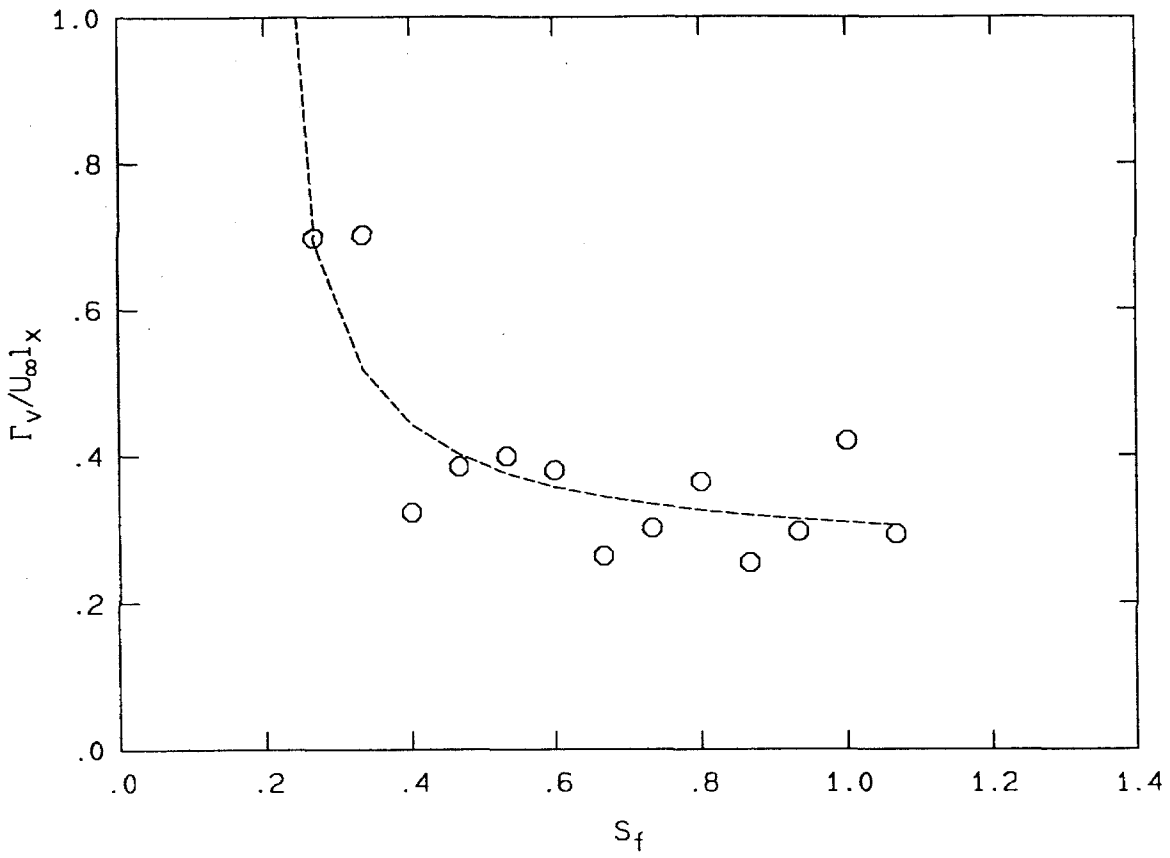

FIG. 3.15 $\Gamma_v/U_\infty \ell_x$ *vs.* S_f. ($\Omega_1 = 8$).

Similar to $\Gamma_v/U_\infty \ell_x$, a measure of the strength of an individual vortical structures can be written as

$$\frac{\Gamma_v}{U_\infty a} = 4\left(\frac{\lambda_x}{S_f}\right)\frac{1-\lambda_x}{\tanh\left(\frac{\pi\lambda_y}{\lambda_x}\right) - \frac{2\ell_y}{h}} . \tag{3.3.7}$$

Figure 3.16 shows the variation of $\Gamma_v/U_\infty a$ with S_f. The dashed line in the figure is Eq. 3.3.7, assuming constant λ_x and λ_y.

For $\ell_y/h \ll 1$, Eqs. 3.3.6 and 3.3.7 become

$$\frac{\Gamma_v}{U_\infty \ell_x} = 2\,(1-\lambda_x)\coth\left(\frac{\pi\lambda_y}{\lambda_x}\right) , \tag{3.3.8}$$

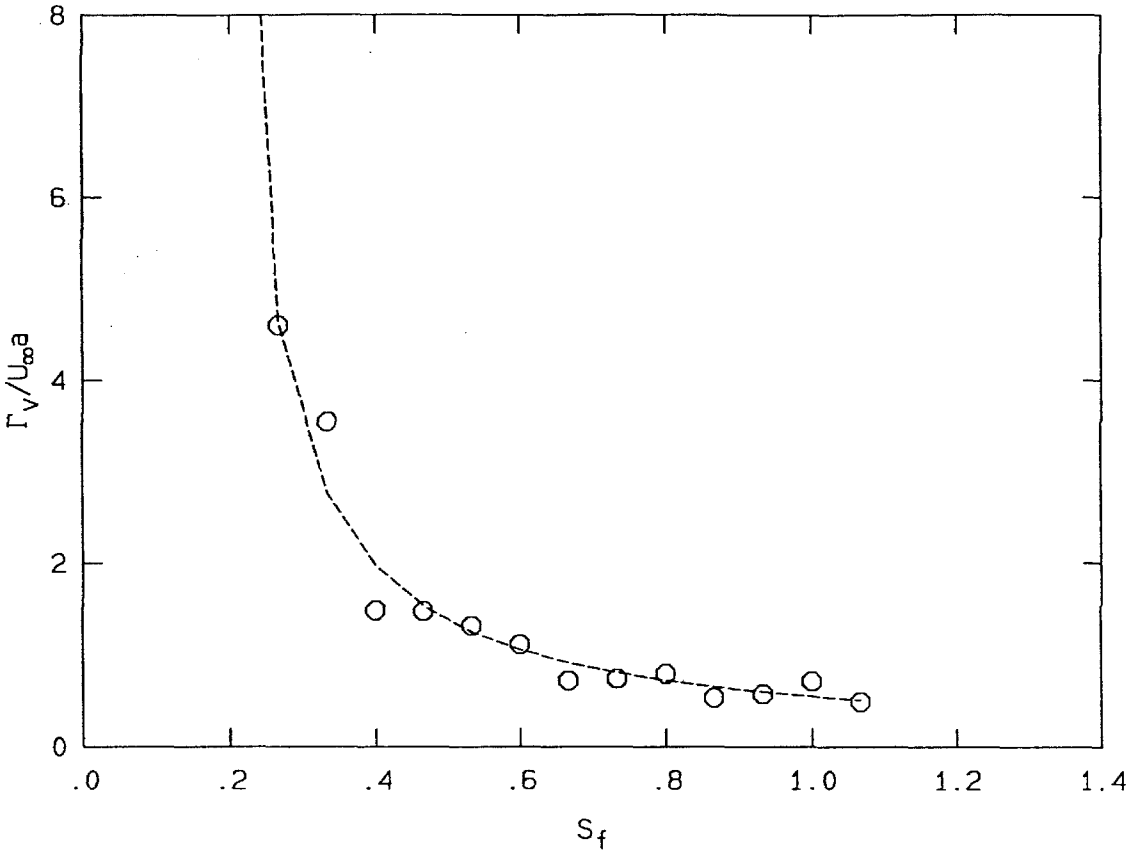

FIG. 3.16 $\Gamma_v/U_\infty a$ *vs.* S_f. $(\Omega_1 = 8)$.

and

$$\frac{\Gamma_v}{U_\infty a} = 4\frac{\lambda_x}{S_f}\,(1-\lambda_x)\coth\left(\frac{\pi\lambda_y}{\lambda_x}\right). \tag{3.3.9}$$

Though not really applicable to this idealized case, it was suggested by Roshko (1954c) that, for a real wake, the mean local velocity along the line of vortex centers, $\overline{u}_s$, be used to calculate the velocity of the vortex street relative to the fluid, where

$$\frac{\Gamma_v}{\overline{u}_s\,\ell_x} = 2 \tag{3.3.10}$$

for the potential flow model discussed here. Using $\overline{u}_s$ instead of u_s in the preceding analysis is equivalent to setting $\tanh(\pi\ell_y/\ell_x) = 1$ in the Eqs. 3.3.6 to 3.3.9. This

leads to simpler estimates,

$$\frac{\Gamma_v}{U_\infty \ell_x} \sim 2\,(1 - \lambda_x)\ , \tag{3.3.11}$$

and

$$\frac{\Gamma_v}{U_\infty a} \sim 4\,(1 - \lambda_x)\,\frac{\lambda_x}{S_f}\ . \tag{3.3.12}$$

3.3.4 Ejection of circulation into the flow

The rate at which circulation is introduced into a flow about a body can be written (*e.g.*, Leonard 1987) as

$$\left.\frac{d\Gamma}{dt}\right|_{\text{flow}} = -2\,A_{\text{body}}\,\ddot{\theta}_{\text{body}}\ , \tag{3.3.13}$$

where A_{body} is the cross-sectional area of the body and $\ddot{\theta}_{\text{body}}$ is the rotational acceleration of the body. In words, net circulation is introduced into a flow from a body only when it experiences rotary acceleration.**

Integrating Eq. 3.3.13 with respect to time yields for the case of a circular cylinder of radius a,

$$\Delta\Gamma_{\text{flow}} = -2\pi a^2\,\Delta\dot{\theta}_{\text{body}}\ , \tag{3.3.14}$$

where Δ denotes "change in." Hence, when a rotating cylinder goes from one rotation rate to another, a net circulation will be ejected from the surface. In dimensionless form this is

$$\frac{\Delta\Gamma}{U_\infty a} = -2\pi\,\Delta\Omega \tag{3.3.15}$$

** It is important to note that "flow" here refers to both the boundary layer and outer flows. To accentuate this point recall that an impulsively started and lifting airfoil has no rotational acceleration but ejects a starting vortex into the outer flow. There is no paradox because an amount of circulation equal to that shed into the outer flow is trapped in the boundary layer of the airfoil.

If all of the circulation of a particular sign created during a forcing period and due to the angular acceleration of the cylinder where put into alternating vortices Eq. 3.3.15 would indicate a vortex strength of up to

$$\frac{\Gamma_v}{U_\infty a} = 4\pi\Omega_1 \,. \tag{3.3.16}$$

For the present data $\Omega_1 = 4$ and 8. This yields values of

$$\frac{\Gamma_v}{U_\infty a} \approx 50;\ 100 \tag{3.3.17}$$

which are much larger than those presented in Fig. 3.16. That the strength of the vortical structures in Fig. 3.16 is only rough does not account for the large discrepancy between the values in Fig. 3.16 and Eq. 3.3.17. A plausible explanation for this discrepancy is that most of the vorticity generated at the cylinder surface is reabsorbed, or is cancelled, combining with vorticity of the opposite sign, before the vortical structure is shed into the wake. This is consistent with the observation that the vortical structures form very close to the cylinder and hence have time to absorb both the positive and the negative circulation generated by the cylinder's rotational acceleration. See Sec. 4.3 for a description of the flow close to the cylinder.

It is likely that the discrepancy will decrease at the lowest values of S_f, because the trend is for

$$\frac{\Gamma_v}{U_\infty a} \sim S_f^{-1} \,, \tag{3.3.18}$$

cf. Eq. 3.3.7. At the very lowest S_f, the shedding of vortices appear much like alternating "starting vortices."

3.4 Displacement thickness and drag coefficient estimation

In order to provide a more quantitative measure of the effects of forcing on the cylinder and the resulting wake, the cylinder drag and wake displacement thickness were estimated from wake streamwise mean and rms velocity profiles. For flow that is two-dimensional, the displacement thickness is normally defined as

$$\frac{\delta^*}{h} \equiv \int_0^1 \left[1 - \frac{u(\eta)}{U_0} \right] d\eta \ . \tag{3.4.1}$$

In this expression, $\eta \equiv y/h$ is the normalized vertical (cross-stream) position, $u(\eta)$ is the mean streamwise velocity, y and h are the vertical position and water channel depth respectively, and U_0 is the velocity in the (free-stream) region outside the cylinder wake and water channel boundary layers. Recall U_0 and U_∞ in Fig. 1.1. By analogy, the "displaced area" for a three-dimensional flow, can be defined as

$$\frac{\Delta^*}{A} \equiv \int_A \left[1 - \frac{u(\eta,\zeta)}{U_0} \right] d\eta \, d\zeta \ , \tag{3.4.2}$$

where A is the test section cross-sectional area, and $\zeta \equiv z/b$ is the normalized spanwise coordinate, with z the spanwise coordinate and b the water channel span. Continuity then yields for U_∞, the free-stream velocity far ahead of the cylinder,

$$U_\infty = \int_A u(\eta,\zeta) \, d\eta \, d\zeta \ . \tag{3.4.3}$$

Using Eq. 3.4.3 to simplify 3.4.2 then yields

$$\frac{\Delta^*}{A} = 1 - \frac{U_\infty}{U_0} \ . \tag{3.4.4}$$

This expression is useful in that it provides information about the flow over an entire cross-section of the water channel, while requiring only the measurement of U_0 and U_∞ (see Fig. 1.1).

In order to remove the contribution of the initial boundary layer (in the absence of the cylinder), to leading order, it is useful to compare U_0 (with the cylinder in place) with the undisturbed flow velocity in the absence of the cylinder, $\widehat{U}_0$, at the same streamwise location. This yields an expression for the approximate displaced area by the wake; *i.e.*,

$$\frac{\widehat{\Delta}^*}{A} = 1 - \frac{\widehat{U}_0}{U_0} \ . \tag{3.4.5}$$

Figure 3.17 depicts the variation of $\widehat{\Delta}^*/A$ with S_f and Ω_1. The dashed curves in this figure denote $\widehat{\Delta}^*/A$ levels equal to, or less than, those corresponding to the unforced case. The parameter space denoted by the solid lines represents an increase in $\widehat{\Delta}^*/A$ over the unforced case. The displacement area can be made substantially larger, or smaller, depending on the frequency and amplitude of oscillation. The minimum for $\widehat{\Delta}^*/A$ over the range shown occurs in the neighborhood of $S_f \approx 1$, and $\Omega_1 \approx 3$, and is roughly half that of the unforced case. Measurements for $\widehat{\Delta}^*/A$ were taken in the range $0.17 \leq S_f \leq 3.3$ in steps of about 0.17, and $0 \leq \Omega_1 \leq 16$ in steps of 1. The data presented in Figs. 3.17 and 3.18 was averaged over 2 minutes (approximately 40 natural unforced shedding cycles). Wake midspan velocity profiles were measured for S_f in the range of 0.15 to 1.4, holding Ω_1 fixed at $\Omega_1 = 2$. Figure 3.18 compares the wake profiles for several values of S_f, at $\Omega_1 = 2$.

For a finite test section and flow that is two-dimensional in the mean over a portion of the the span, it can be shown that the sectional drag coefficient can be estimated by the expression (Dimotakis 1978):

$$C_D \approx \frac{2\,h/d}{(1-\delta^*/h)^2}\left[\int_0^1 \frac{u}{U_0}\left(1-\frac{u}{U_0}\right)d\eta - \int_0^1 \frac{u'^2 - v'^2}{U_0^2}\,d\eta + \frac{1}{2}\left(\frac{\delta^*}{h}\right)^2\right] . \tag{3.4.6}$$

In this expression, u' and v' are the streamwise and cross-stream rms velocities, and δ^* is the displacement thickness defined in Eq. 3.4.1. The displacement thickness

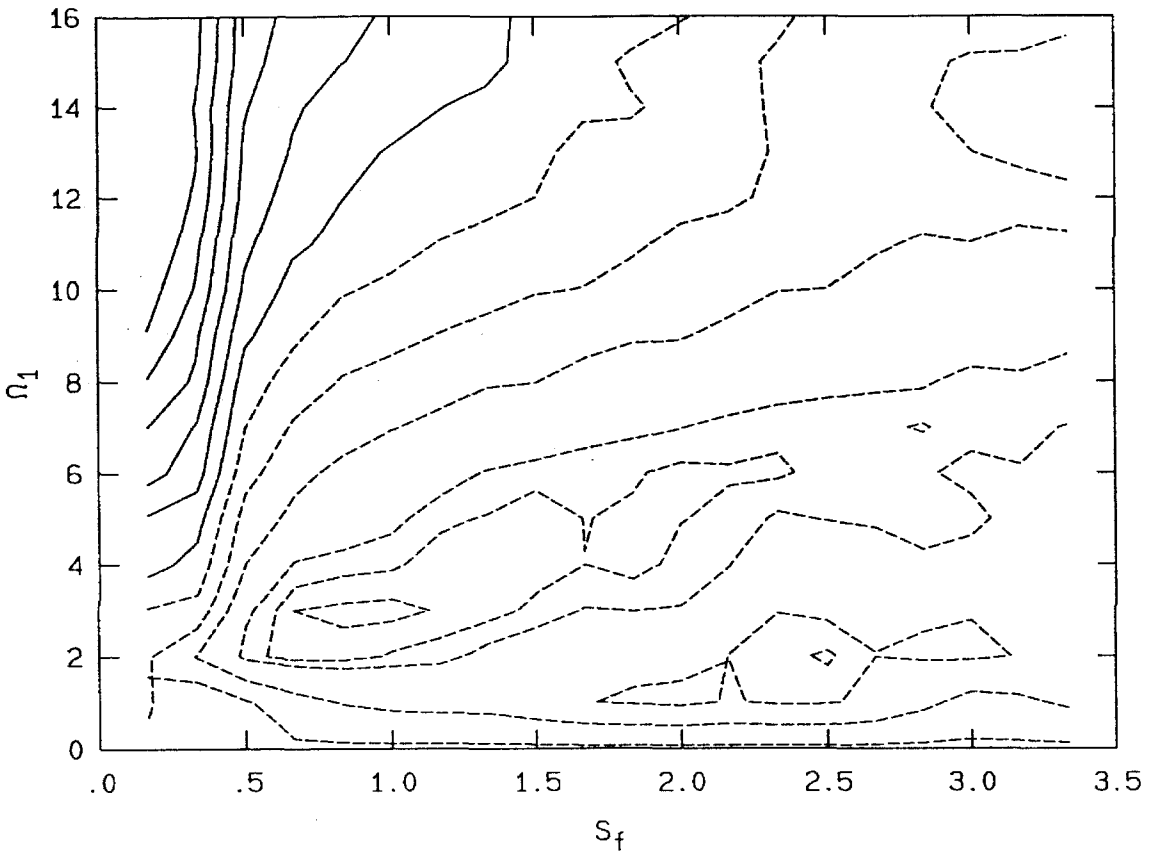

FIG. 3.17 Variation of $\widehat{\Delta}^*/A$ with S_f and Ω_1. Dashed lines mark the region where the wake displacement thickness is less than in the unforced case (note the minimum around $S_f = 1$ and $\Omega_1 = 3$). Solid lines mark the region where it is greater than or equal to the unforced case.

and drag coefficient estimates summarized in Figs. 3.19 and 3.20 were calculated from midspan mean velocity profiles, using Eqs. 3.4.1 and 3.4.6, neglecting the fluctuating terms, which are not only small, but very nearly cancel (Dimotakis 1978). As can be seen, there is a broad minimum in C_D and δ^*/h around $S_f = 1$. The estimated C_D for the unforced case is a factor of six greater than for this forced case. Similarly, there is a factor of five reduction in δ^*/h. Note that the value of δ^*/h for a particular S_f and Ω_1 is generally less than the corresponding value of $\widehat{\Delta}^*/A$, indicating an increase in δ^*/h outside the midspan region. Since C_D

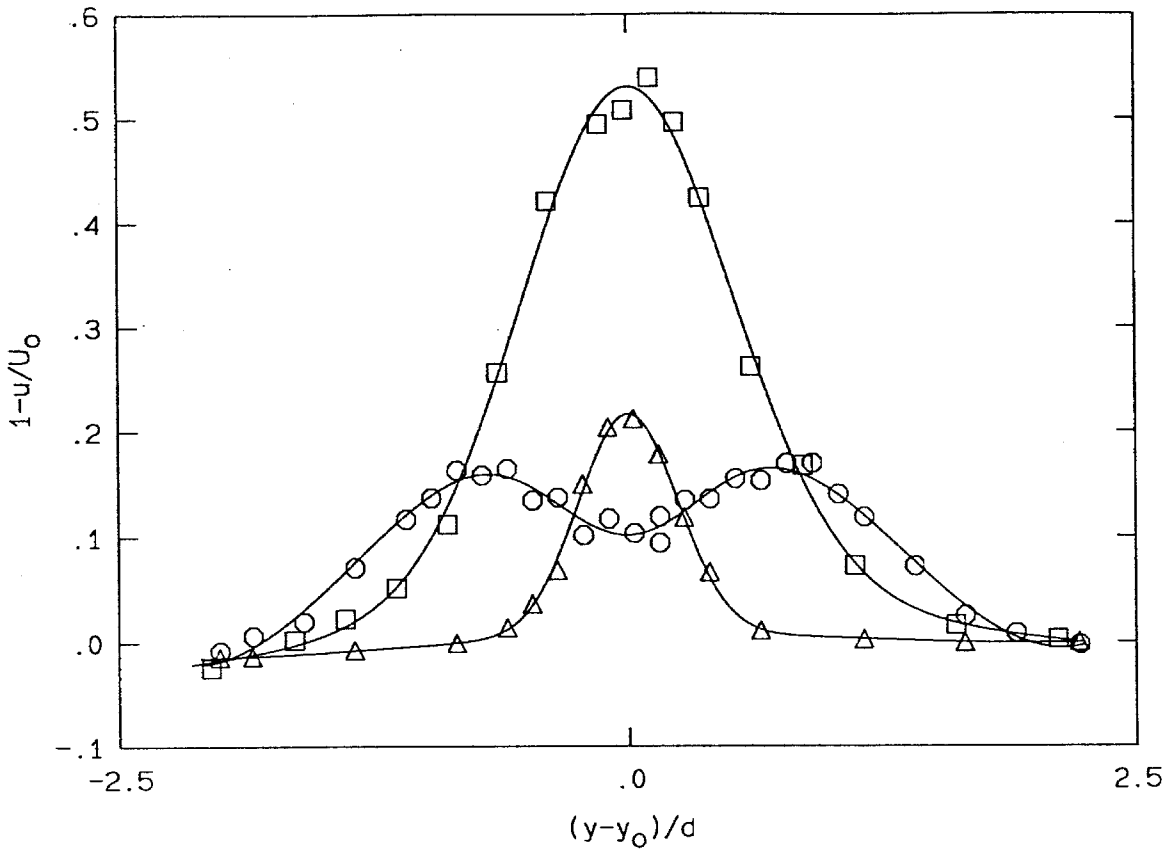

FIG. 3.18 Cylinder wake mean velocity profiles, measured at midspan ($\Omega_1 = 2$). Squares: unforced, circles: $S_f \approx 0.2$, and triangles: $S_f \approx 1$.

increases with δ^*/h it should also increase outside this midspan region. A spanwise variation in δ^*/h may be attributed to the interaction of the sidewalls with the shed vortices. See Roberts (1985), Roberts & Roshko (1985), Koochesfahani (1987), and Kurosaka *et al.* (1988).

Figure 3.21 shows the correlation between the calculated sectional drag coefficients and sectional wake displacement thicknesses. The dashed line in that figure denotes the approximate relationship (*e.g.*, Batchelor 1970, §5.12),

$$C_D \approx \frac{\delta^*}{a}, \tag{3.4.7}$$

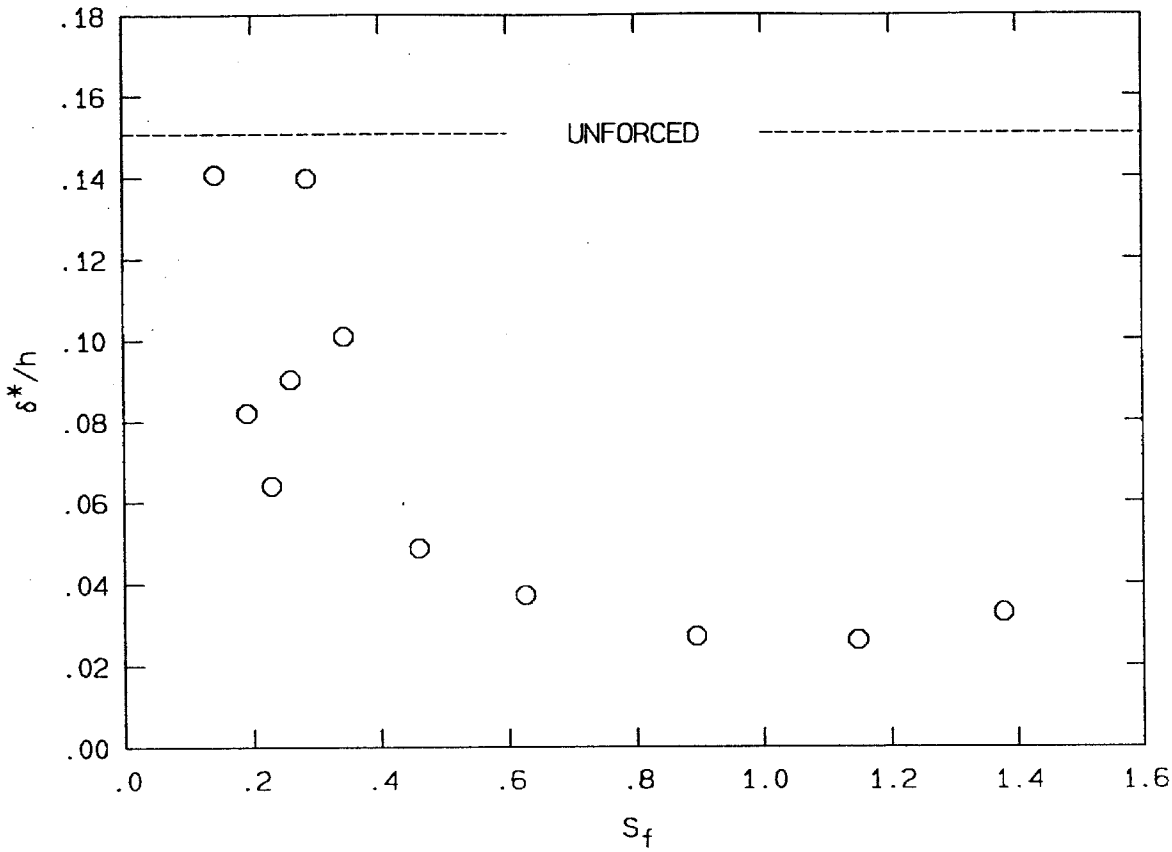

FIG. 3.19 Cylinder wake displacement thickness variation with S_f ($\Omega_1 = 2$).

for wake profiles taken far downstream of the cylinder.

Another local minimum exists near $S_f \approx 0.2$. The flow visualization in Fig. 3.4 suggests that this corresponds to the dual mode in which the cylinder releases *two* vortices of opposite sign during each half-cycle. When one of these two vortices shed from the bottom appears on top, a dip is observed in the corresponding velocity profile. See circles in Fig. 3.18. This phenomenon was only observed in a small region of the (S_f, Ω_1)-parameter space.

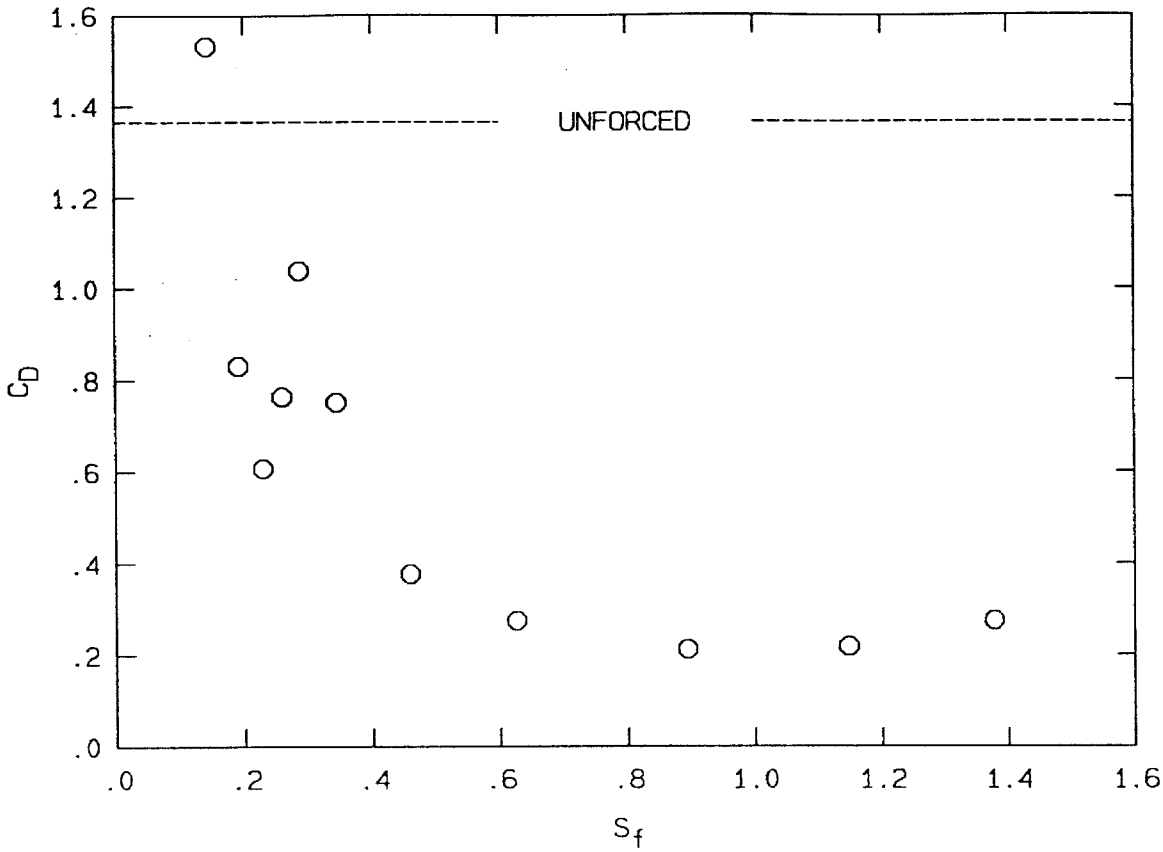

FIG. 3.20 Drag coefficient variation with S_f ($\Omega_1 = 2$).

3.5 A note on the interpretation of linear stability analyses

This section was originally written in response to a reviewer of the paper "Rotary oscillation control of a cylinder wake," by Tokumaru & Dimotakis (1991). It is included here as a point of interest.

There has been much interest in the use of linear stability analyses to describe unforced bluff body flows. See Koch (1985), Triantafyllou *et al.* (1986), Monkewitz & Nguyen (1987), Provansal *et al.* (1987), Chomaz *et al.* (1988), Monkewitz (1988), and Karniadakis & Triantafyllou (1989). Using linear theory, it has been noted that the response to periodic forcing of the absolutely unstable near wake region of a

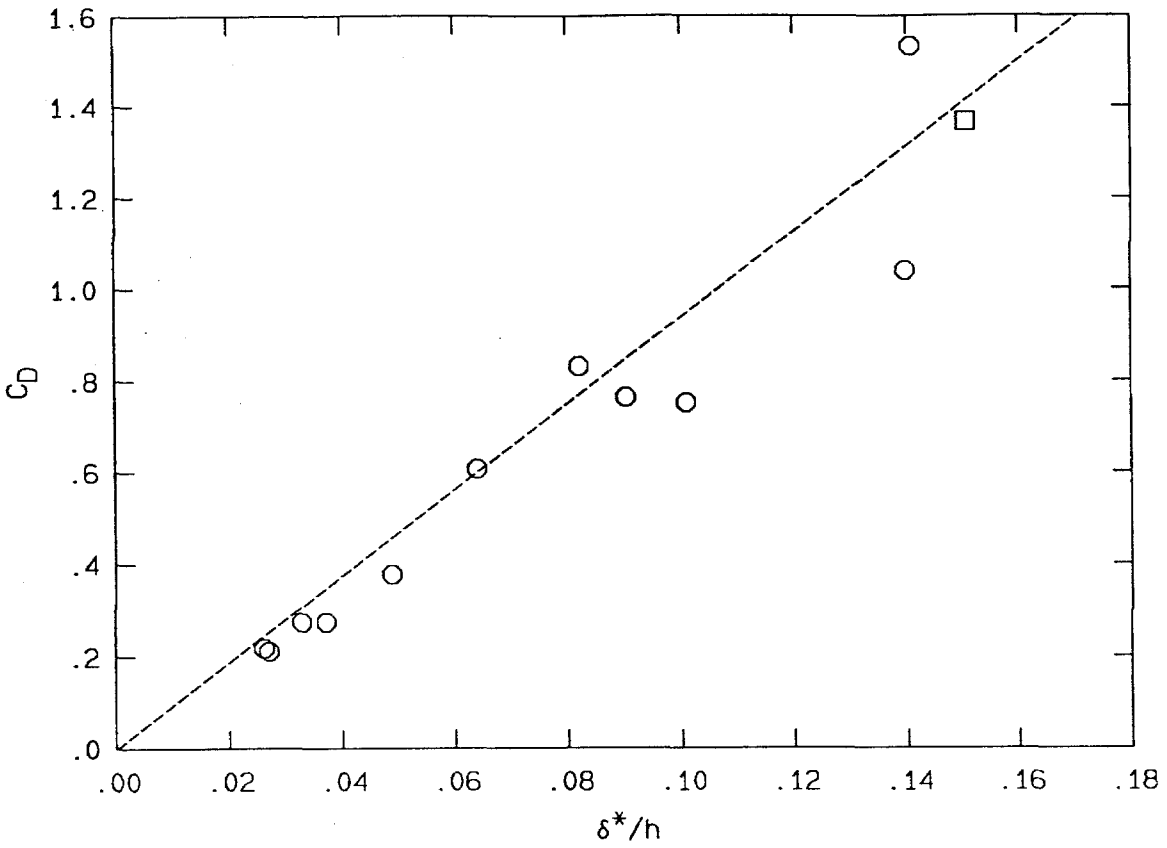

FIG. 3.21 C_D *vs.* δ^*/h. Circles: forced ($\Omega_1 = 2$), square: unforced ($\Omega_1 = 0$).

bluff body will be overwhelmed by the "intrinsic" vortex shedding mode observed in the absence of external forcing. See Huerre & Monkewitz (1985), Monkewitz & Nguyen (1987), Chomaz *et al.* (1988), and Karniadakis & Triantafyllou (1989). This argument is based on a linearized model and suggests that the periodic response will be overwhelmed because the transient response grows exponentially in time while the forcing is only periodic in time. Since the system cannot be considered linear for large excursions from the "base" state, however, this argument can only be relied upon for infinitesimal forcing amplitudes and short times. It is not surprising, perhaps, that this interpretation of the results of linear theory is not in accord with experiments and simulations which show that finite amplitude forcing of the wake of a bluff body can result in a wake structure that is synchronous with the forcing,

over a range of forcing frequencies and amplitudes; *e.g.*, Koopman (1967), Provansal *et al.* (1987), and Karniadakis & Triantafyllou (1989).

Provansal *et al.* (1987), examined the (nonlinear) Landau stability model (Landau 1944, Stuart 1958, 1960) and showed how it could be used to describe qualitatively the conditions necessary for synchronization at small but finite forcing amplitudes, at Reynolds numbers in the vicinity of the onset of vortex shedding. See also Landau & Lifshitz (1987, §26 & §30). Evidently, while the linear stability analysis, and hence the notion of the bluff body wake as a globally unstable flow with a region of absolute instability, is useful in describing the system dynamics, given an *a priori* knowledge of the final averaged flow (Karniadakis & Triantafyllou, 1989), *prediction* of the final dynamic state, especially in the presence of finite external forcing, requires a different approach.

CHAPTER 4

A particular forced case

In this chapter, a particular case of a cylinder executing forced rotary oscillations in a uniform stream is examined. An estimate of the unsteady, phase-averaged streamfunction was made. The speed and strength of the shed vortical structures was also estimated.

4.1 Experimental setup

The experiments documented here were performed in the $20'' \times 20''$ Free Surface Water Tunnel at GALCIT. The cylinder used for the near wake velocity measurements is an anodized and machined aluminum tube, $4''$ in diameter, and mounted and driven by the apparatus described in Ch. 2. The command signal for the cylinder velocity was generated by a computer controlled function generator. The position of the cylinder output by the BEI 13-bit absolute position encoder was read using the computer's parallel interface.

Velocities were measured using a one-channel, Bragg cell frequency-shifted laser Doppler velocimeter with a translatable (and rotatable) focal volume. A Lexel Model 85 Argon-ion laser operating in single line mode (514.5 nm) at about 200 mW was used for the LDV. The laser beam for the LDV velocity measurements was split into two beams of nearly the same intensity using a cube beam splitter. The beams were then Bragg cell frequency-shifted to allow for flow reversals. The Bragg cell

offset between the two beams was 200 kHz for the data presented in this chapter. A Dove prism was introduced in line after the Bragg cells for the purpose of rotating the orientation of the measurement volume. An achromat was used to focus the beams in a focal (measurement) volume located in the midspan plane of the water tunnel. The light scattered from the focal volume was gathered by an achromat and focused on a photodiode with an integral low noise pre-amplifier designed by Dan Lang. The signal from the pre-amplifier was then band-pass filtered above and below the frequency corresponding to the mean flow velocity. The band-pass range was chosen to pass instantaneous velocity fluctuations. A tracking phase-locked loop designed by Dan Lang and Paul Dimotakis was then used to lock a TTL square wave to the dominant frequency. The TTL signal was read by a counter-timer board on a data acquisition computer and stored on disk for later processing. The transmitting and receiving hardware was mounted on a motor driven x-y-z traverse (positioner).

4.2 Measurement details

For all the data presented in this chapter, $S_f = 0.94$, $\Omega_1 = 2$, and $Re = 2.1 \times 10^4$. This Reynolds number was chosen to be higher than in Ch. 3 to shorten the time scale of the flow dynamics, and hence also of the experiment. The tangential velocity, $v_\theta(r, \theta)$ was measured along eleven θ = constant rays in the upper half plane, at 15 degree intervals. Along most of these rays, v_θ was measured in steps $\delta r/a = 0.01$, beginning near the cylinder surface, for $1.01 \leq r/a \leq 1.15$, where r/a is the normalized radial position. Then in steps of $\delta r/a = 0.025$ for $1.15 \leq r/a \leq 1.25$, steps of $\delta r/a = 0.05$ for $1.25 \leq r/a \leq 1.5$ and finally in steps of $\delta r/a = 0.25$ for $1.5 \leq r/a \leq 2.5$. Figure 4.1 shows the θ = constant measurement rays. The velocities at each location were measured at $f\,\delta t = 0.02$ time intervals. At each

location, 41 forcing periods were averaged at constant forcing phase, yielding 50 realizations of the flow averaged at constant forcing phase. The velocity field in the lower half plane was taken to be the same as that at the top, but a half forcing period out of phase.

Before the velocity data were averaged at constant phase, they were smoothed in *time* using a gaussian filter with a 3 dB cutoff around five times the forcing frequency. No other explicit smoothing was performed, but, because of the wide spacing of the θ = constant rays, there was an implicit smoothing of data interpolated in between.

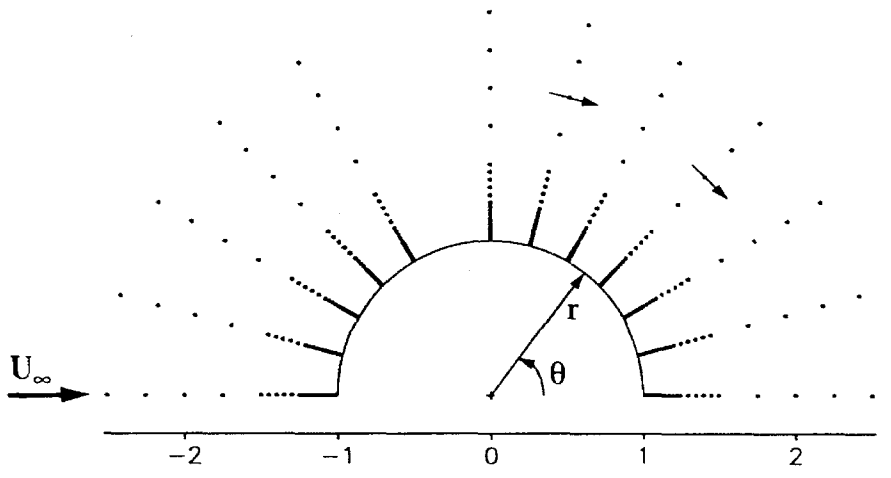

FIG. 4.1 Measurement locations.

4.2.1 Streamfunction

Calculation of the stream function was straightforward. Given that the stream function Ψ is known at some point in the flow $\mathbf{x}_0$, and the velocity normal to any path C connecting the two points $\mathbf{x}$ and $\mathbf{x}_0$, $u_n \equiv \mathbf{u} \cdot \mathbf{n}$, is also known, the (dimensionless) stream function $\psi(\mathbf{x})$ can be calculated, for two-dimensional flows, by the expression

$$\psi\left(\mathbf{x}/a\right) \equiv \frac{\Psi(\mathbf{x})}{U_\infty a} = \int_C \frac{u_n}{U_\infty} \frac{dl}{a} + \psi_0\left(\mathbf{x}_0/a\right) \ . \tag{4.2.1}$$

Further, since the stream function is constant along a solid boundary surface, it is convenient to begin integrating from there, and to choose some constant $\psi(\mathbf{x}_0/a) = \psi_0$ on that surface. For the present experiments, Eq. 4.2.1 was written as

$$\psi(r/a) = \int_1^{r/a} \frac{v_\theta(r/a)}{U_\infty} \, dr/a \ . \tag{4.2.2}$$

It should be noted that for a number of the measurements, the boundary layer near the wall could not be resolved with the present setup, because of large gradients in the velocity, and difficulties in positioning the measurement volume. This did not cause large errors in the calculation of ψ, however, because the velocity at the wall was known *a priori*. For the integration of Eq. 4.2.2, a (straight) line was fit between the velocity at the wall, and the nearest measured velocity.

The forced shedding process for $S_f \approx 1$ and $\Omega_1 \approx 2$ is illustrated in Figs. 4.3 to 4.12. The illustrations on the top denote fluid marked with dye introduced just ahead of the ten o'clock position on the cylinder. They were traced from a video tape of the flow. The circles with the Ω in them indicate the direction and magnitude (arbitrary scale) of the rotation rate. The illustrations on the bottom

show the stream lines calculated from data averaged at constant forcing phase. Brief notes on the averaged constant-phase streamline data are contained in the captions of the Figs. 4.2 - 4.12*. Figure 4.2 illustrates the average, over all forcing phases, of the stream function.

The stream function data were first estimated by integrating along θ = constant rays. Between the measurement points, the streamfunction was estimated using spline interpolation, first along the rays, and then between them. The streamline plots were generated using a contour plotting routine with points interpolated on a 300×400 rectangular grid.

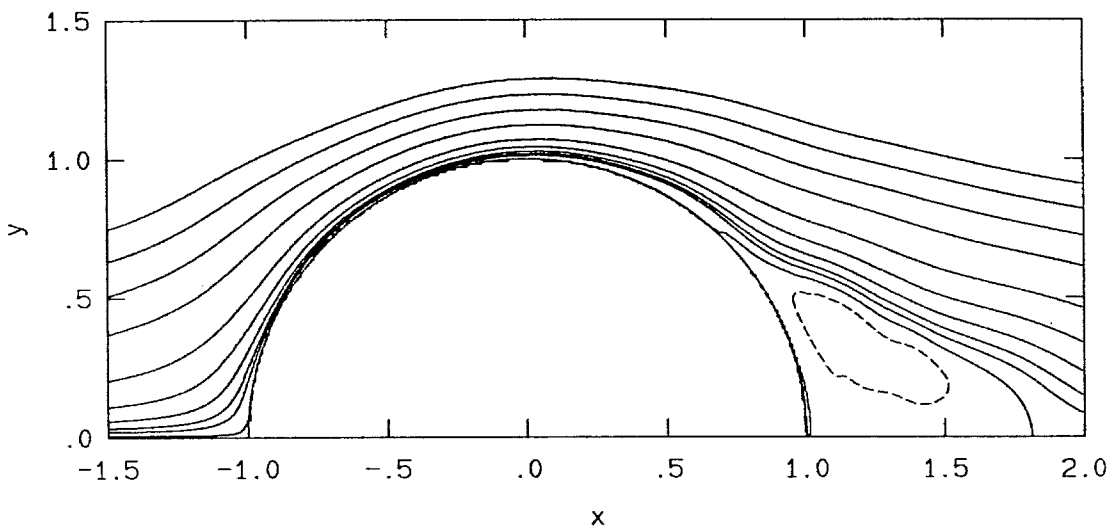

FIG. 4.2 Streamlines averaged over all phases. Note the delayed average separation point and the small averaged "recirculation" region realized in this forcing regime. This looks very much like the (unforced) time averaged flow around the cylinder at higher Reynolds numbers ($> 5 \times 10^5$), which also has a similar drag coefficient of about 0.2 to 0.3.

In Figs. 4.3 - 4.12, the flow visualization data are illustrated on the top and the phase averaged stream line pattern calculated from ldv data are on the bottom.

* The entire set of 50 phase averaged realizations of the flow is included in Appendix B.

The dot in the figures mark the approximate cylinder position, the arrows, the direction of rotation, and the shaded regions, the range of motion.

It appears that the forced shedding mechanism outlined here replaces the natural shedding mechanism with one that gathers vorticity close to the cylinder surface, and *then* releases a vortical structure into the flow. This would suggest that the formation of vortical structures in the forced case is *less* affected by the stability characteristics of the flow downstream of the cylinder. This is in contrast to observations of unforced vortex shedding which show that vorticity is introduced into the flow from more-or-less steady separation points, with the resulting vortical structures forming in the wake of the cylinder.

When comparing the streamline patterns in this chapter and Appendix B with simulations, several factors should be considered. As can be seen from Fig. 4.1, the spatial resolution of the data for $r/a > 1.5$ corresponds to only a handful of measurement locations per vortical structure in that region. The continuity of the velocity field, however, diminishes this problem. As stated in Sec. 4.2, the data in the lower half plane was taken to be the same as in the upper half plane, but a half forcing cycle out of phase. Because of asymmetries in the flow, this match (at $y = 0$) is not perfect and causes small "glitches" in the streamline pattern around the joint between the upper and lower half planes. Comparing streamline patterns a half period apart gives an indication of the asymmetry in the data. Because the present data was measured at midspan, there is no out-of-plane velocity, in the mean. This does not, however, remove three-dimensional effects like vortex stretching and instantaneous out-of-plane flow.

Because of factors such as these, comparisons of the present data with simulations will not be perfect. It should be emphasized that the basic mechanisms

gathering vorticity close to the cylinder (allowing it to mix and cancel) and then ejecting it into the flow, should not be strongly affected by these factors. A simulation that captures the behavior of the unsteady boundary layer in this flow will likely have results similar to the present data.

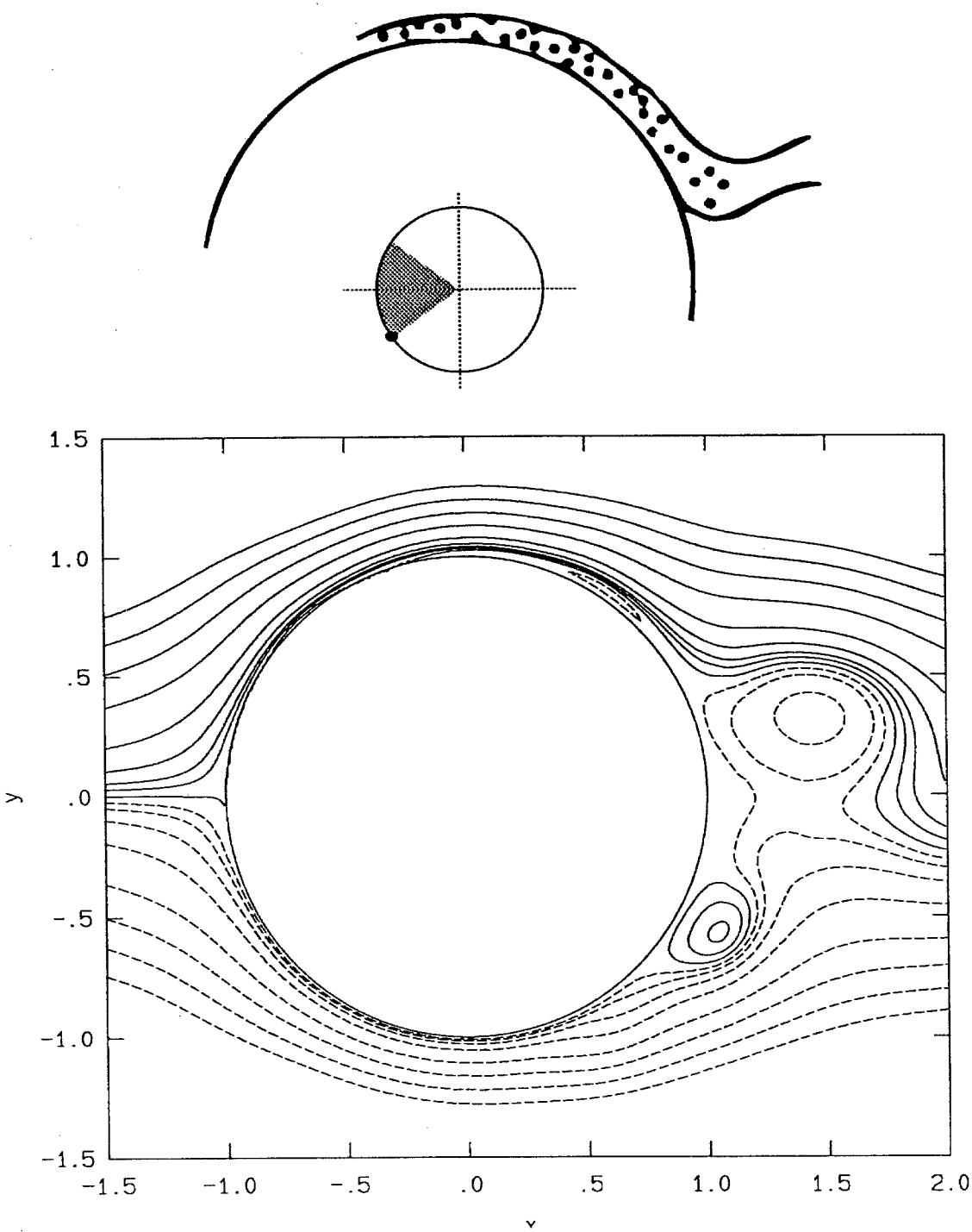

FIG. 4.3 $ft = 0.0$. At this point, the cylinder has just finished shedding a vortex (at $x/a = 1.5$), and the kernel (bump) of the next vortex to be shed can be seen at about 45 degrees on the cylinder surface.

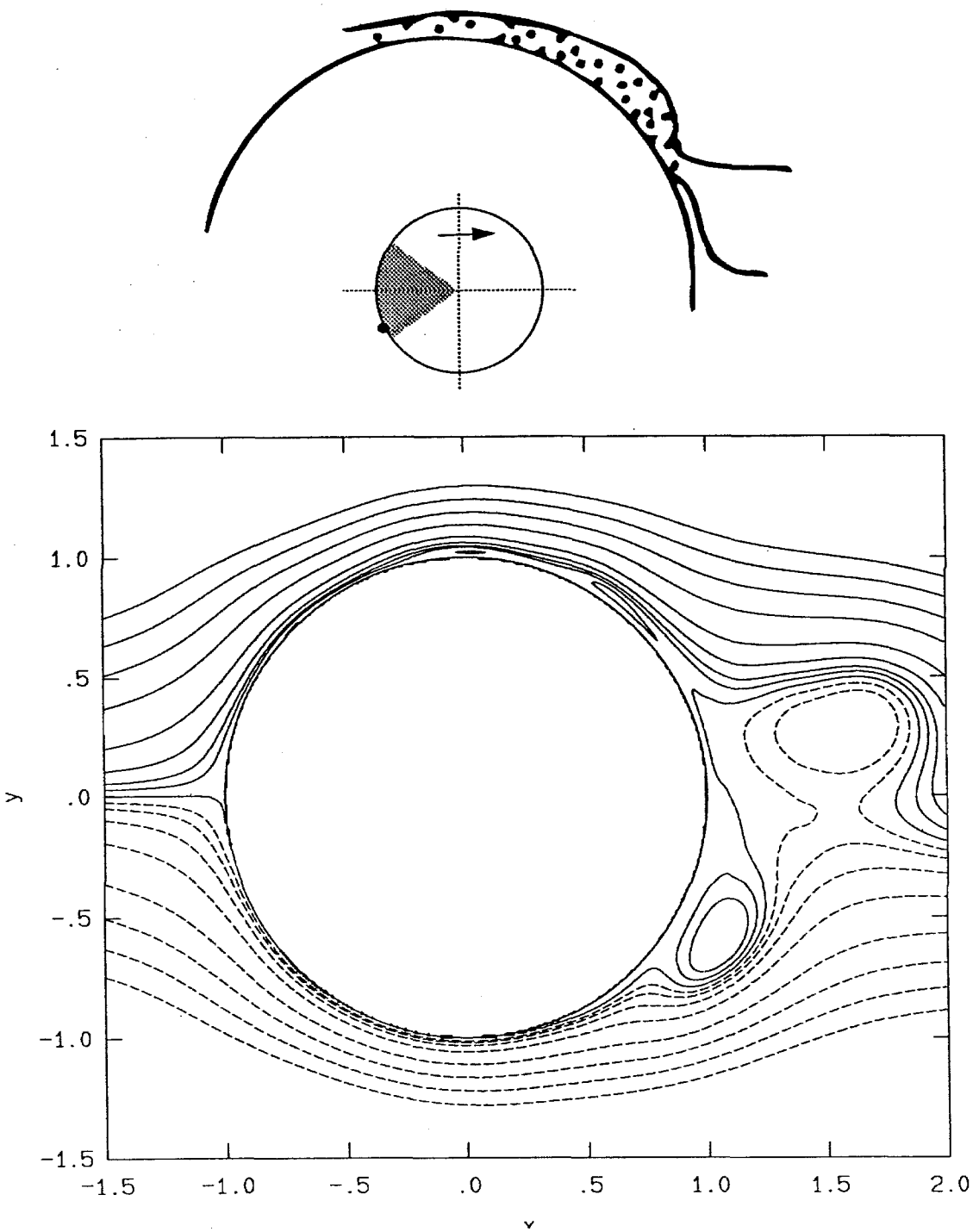

FIG. 4.4 $ft = 0.1$. The bump has grown larger, note also the beginnings of a second bump on the cylinder surface at about 90 degrees.

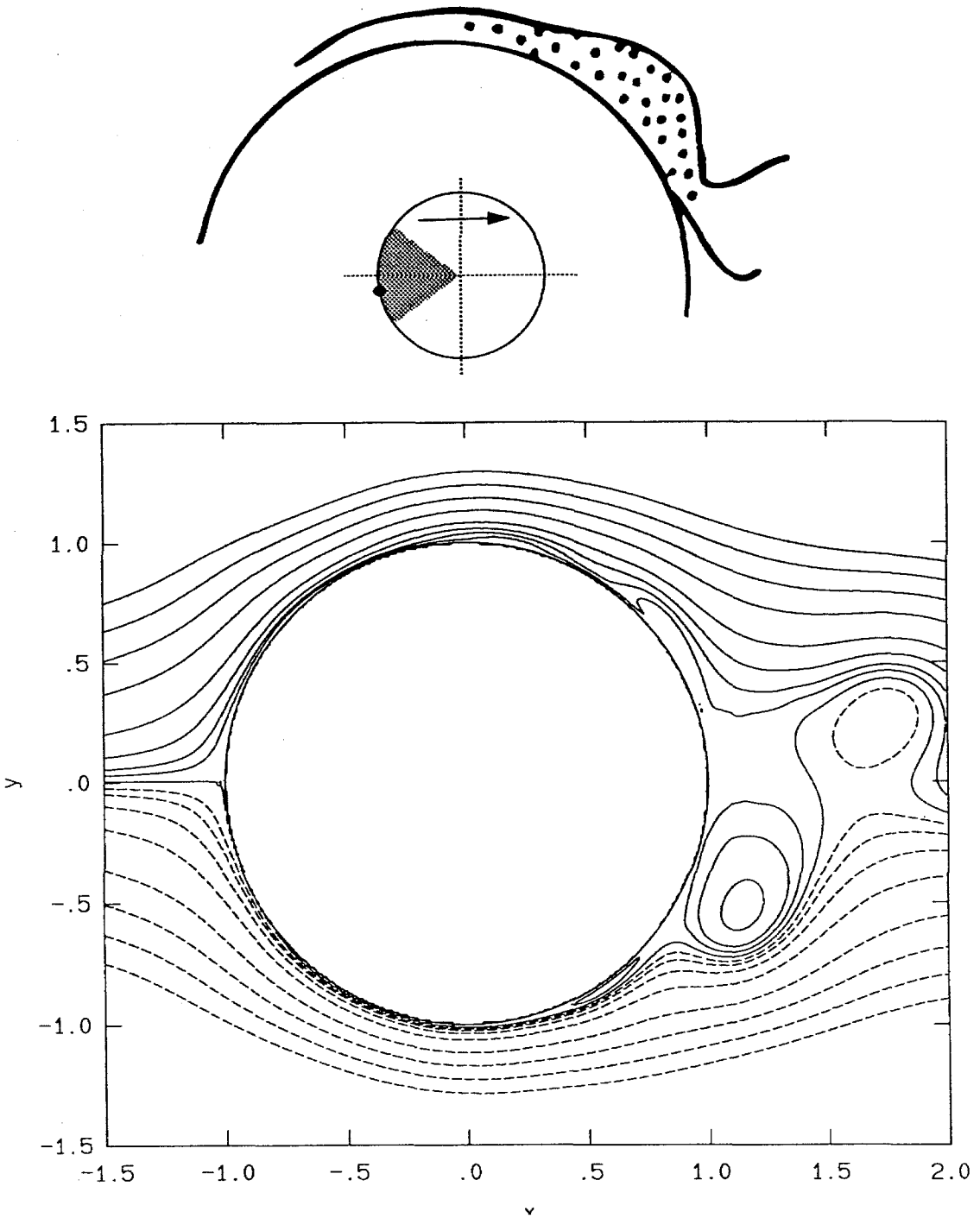

FIG. 4.5 $ft = 0.2$. Figure 4.5. Both the main bump and secondary bump have grown larger, and moved around the cylinder in the clockwise direction. Note that there is also a large vortical structure being shed off the lower surface at this time.

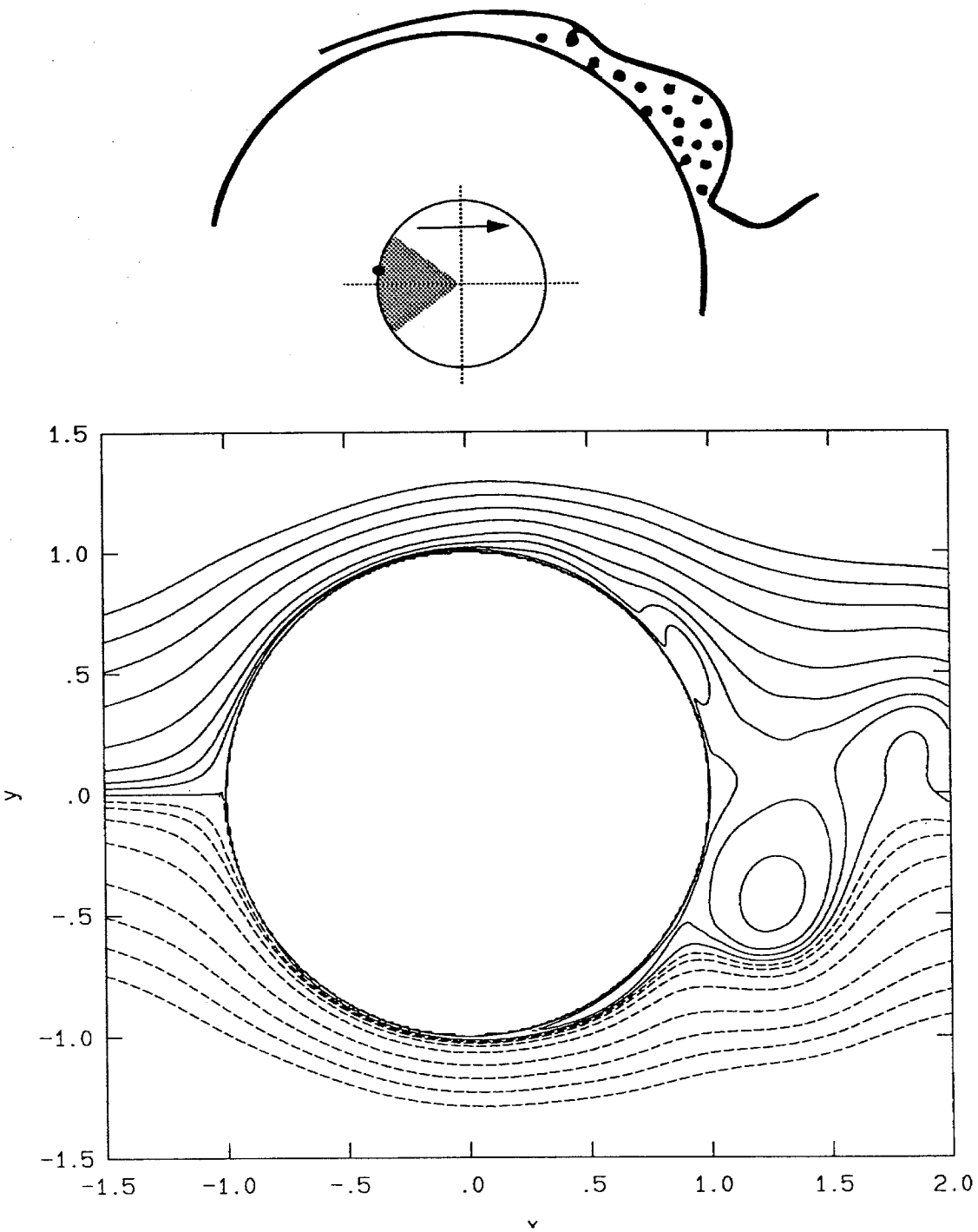

FIG. 4.6 $ft = 0.3$. The bumps continue to grow. Note that the main bump seems to be held in place relative to the cylinder surface, possibly by the flow induced by the previously shed vortices. Note that the cylinder motion is in the clockwise direction which, intuitively, would tend to have the opposite effect.

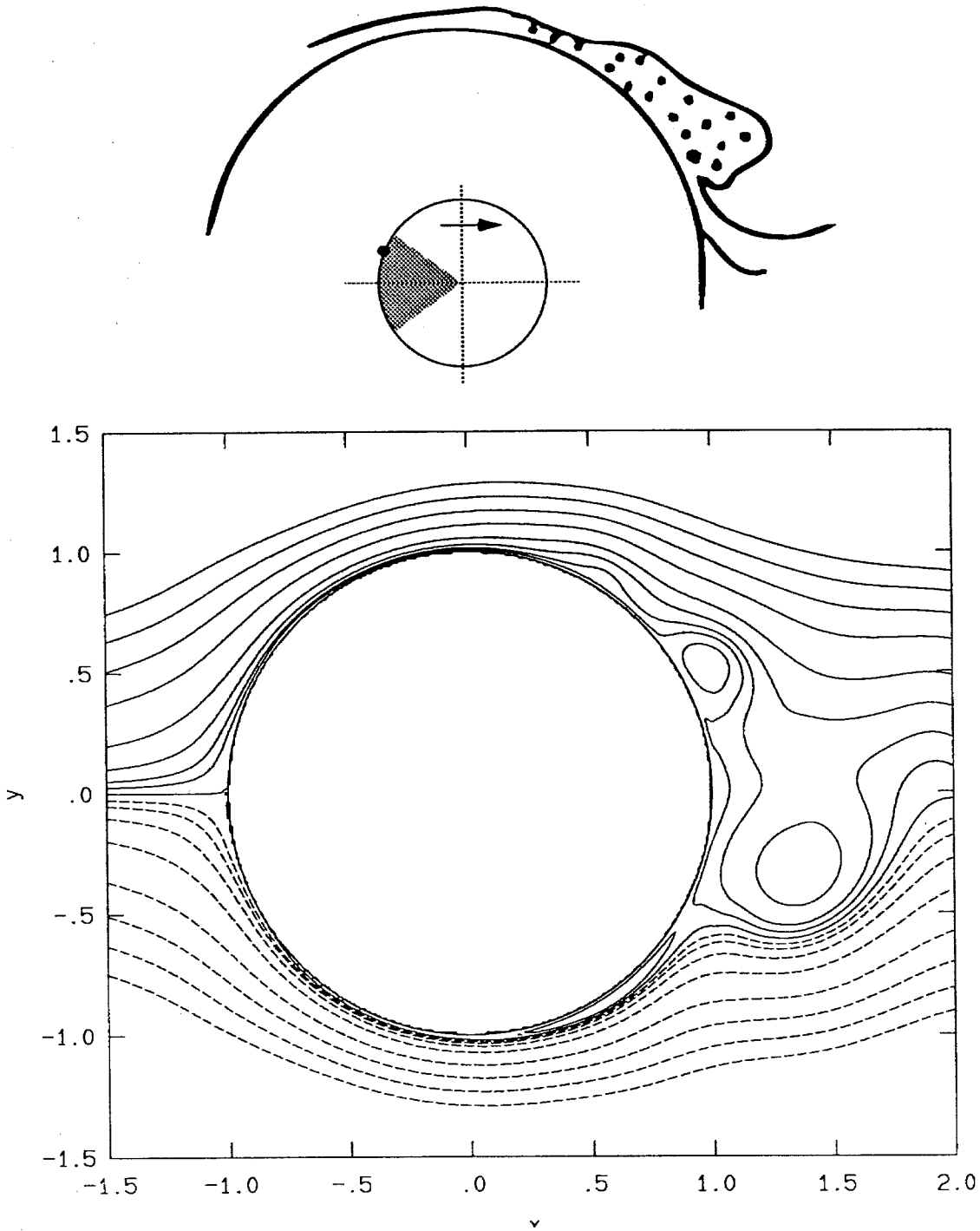

FIG. 4.7 $ft = 0.4$. Again, the bumps continue to grow, but now are becoming more rounded. The large bump almost looks as if it is being "pinched" into the flow.

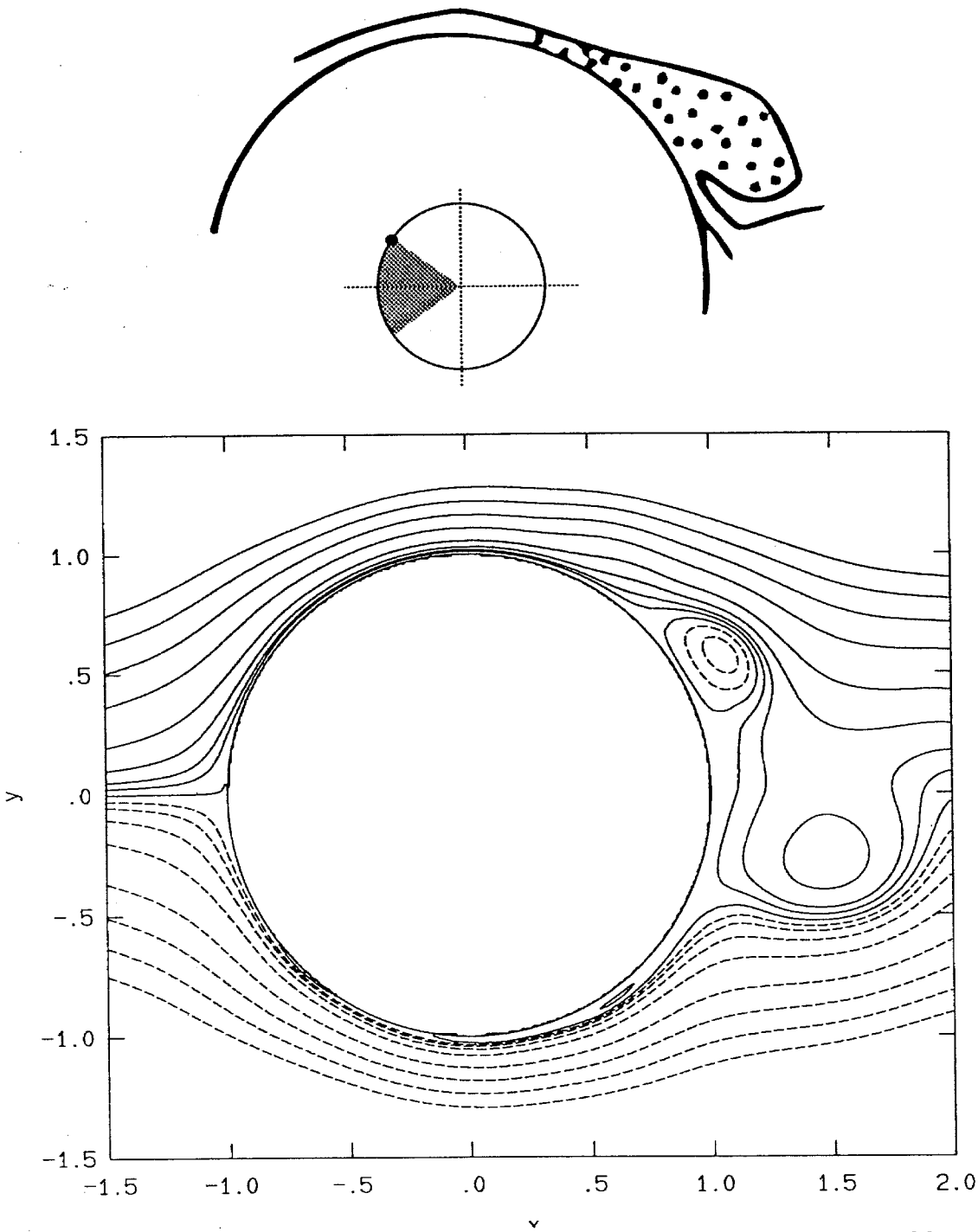

FIG. 4.8 $ft = 0.5$. The presence of the secondary bump is less noticeable; most likely it has been merged with the primary structure.

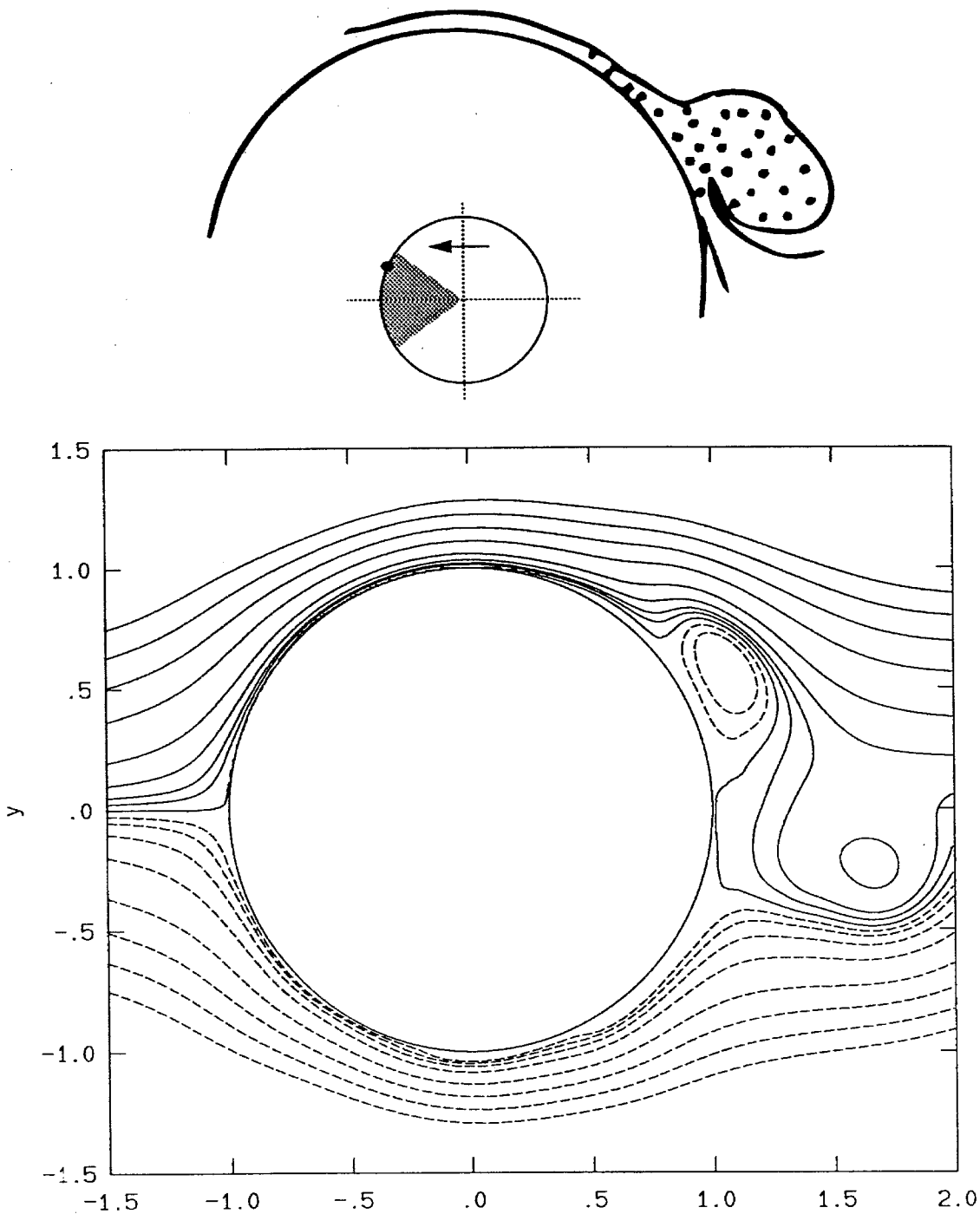

FIG. 4.9 $ft = 0.6$. The cylinder begins to move in the opposite direction to the flow on that side. This appears to be when the vortex begins to be released into the flow.

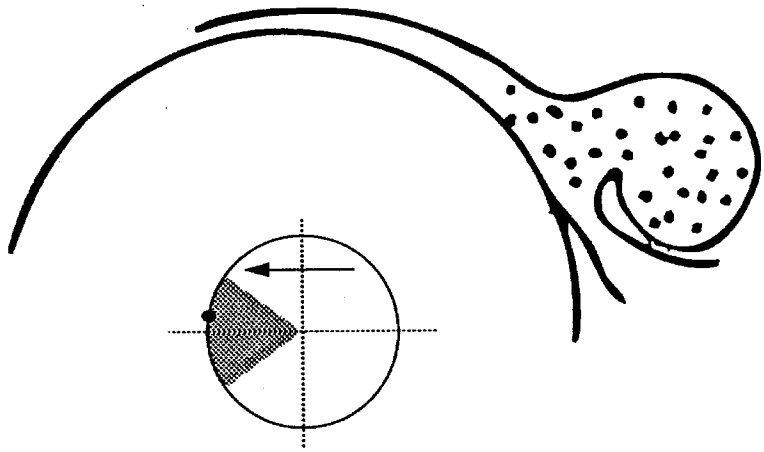

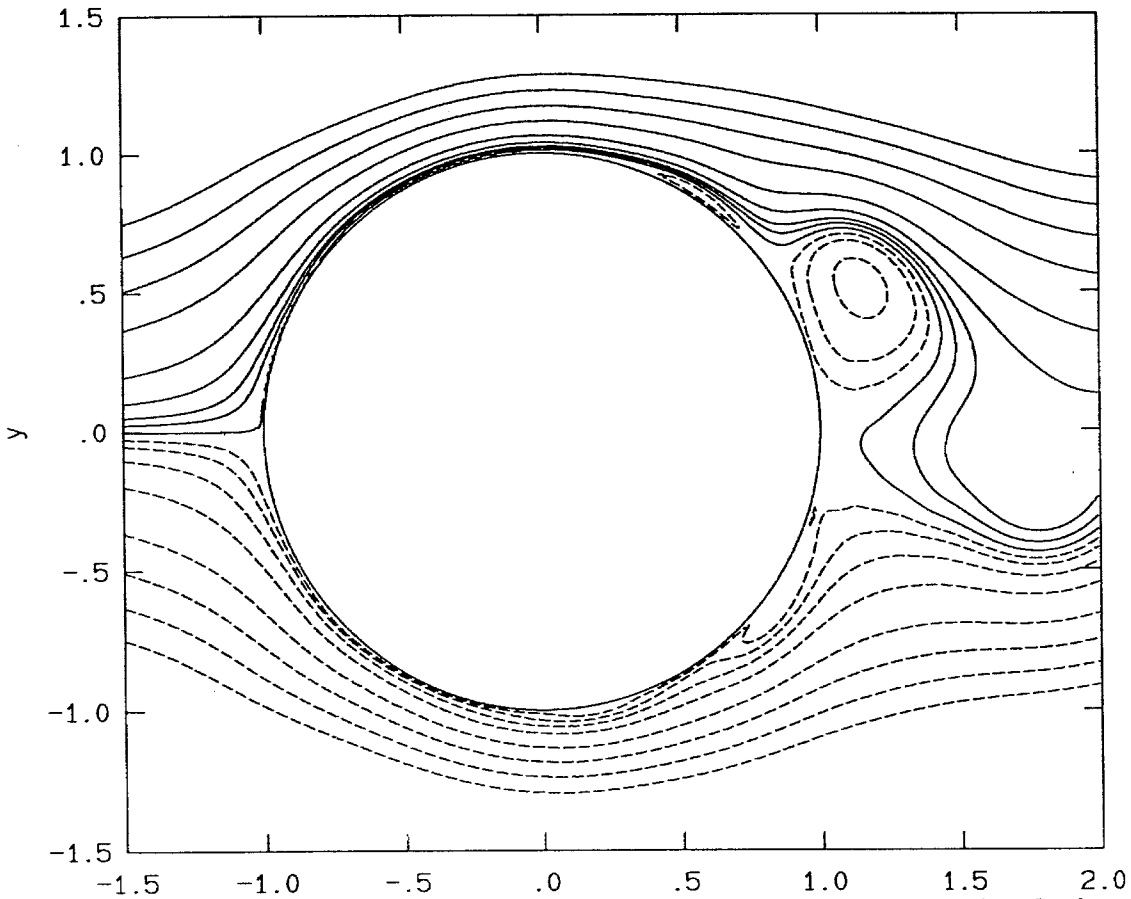

FIG. 4.10 $ft = 0.7$. Note the beginnings of the next vortex to be shed.

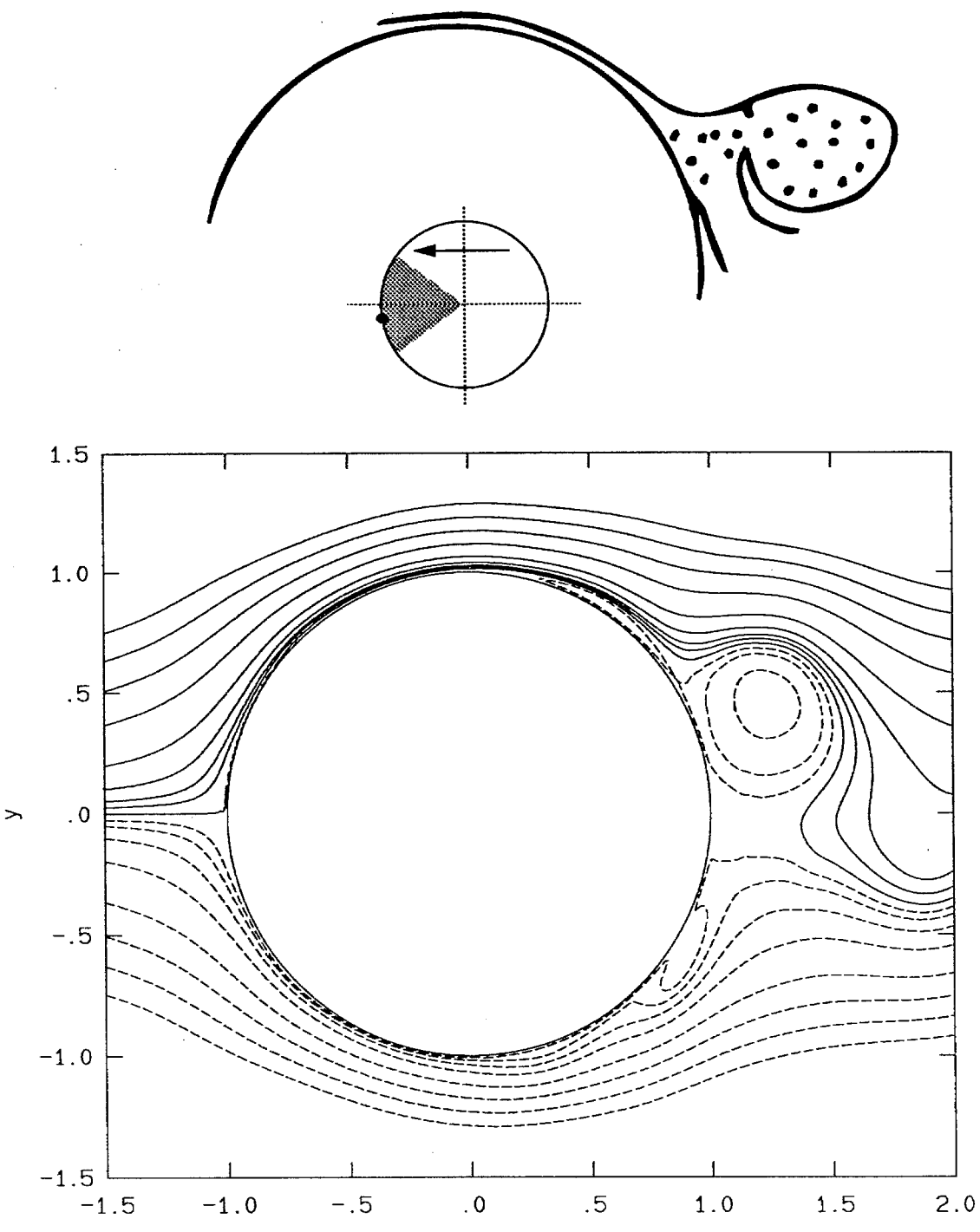

FIG. 4.11 $ft = 0.8$. The main vortex begins to move off to the right. The next vortex to be shed continues to be held in place both by the vortices which have been shed, and the rotation of the cylinder.

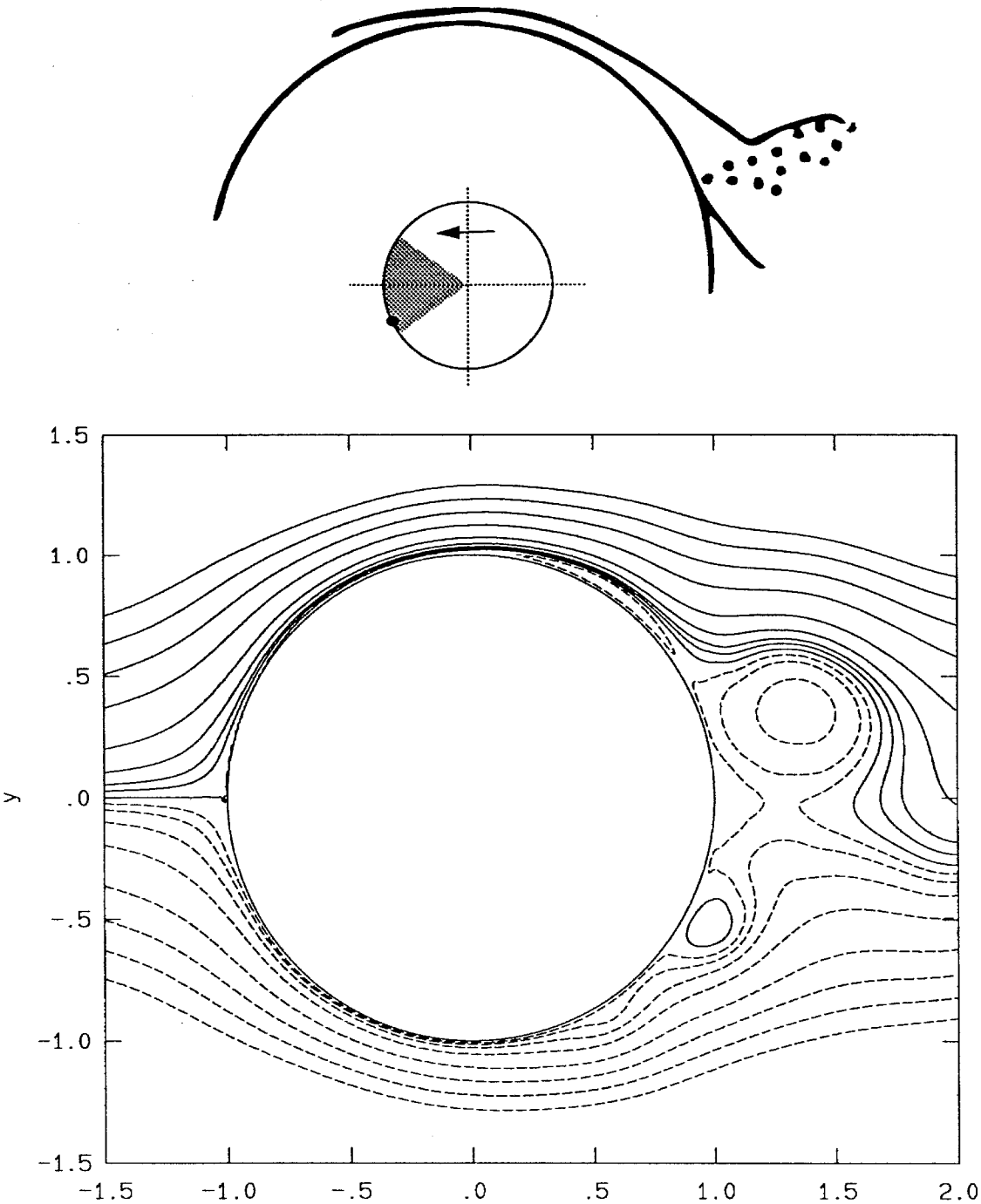

FIG. 4.12 $ft = 0.9$. The main vortex continues to move off to the right.

4.3 Strength of shed vortices

Section 3.3.3 proposed a measure of the strength of the vortical structures shed into the wake. In this section, another estimate for the circulation of the vortical structures is made by measuring the circulation of the flow about the cylinder,

$$\Gamma_c(r) \equiv r \int_{C(r)} v_\theta(r,\theta)\, d\theta \ ,$$

for varying phase, ft, and radius of integration, r. The associated dimensionless quantity is

$$\frac{\Gamma_c(r)}{U_\infty a} \ .$$

Figure 4.15 shows the variation of $\Gamma_c/U_\infty a$ with ft and r/a.

The circulation in an annulus between two circles of radii r_1 and r_2 can be written as

$$\frac{\Gamma_v}{U_\infty a}\Big|_{r_1}^{r_2} = \frac{\Gamma_c(r_2)}{U_\infty a} - \frac{\Gamma_c(r_1)}{U_\infty a} \ . \tag{4.3.1}$$

Hence, an estimate for the strength of a vortical structure (residing in an annulus) is

$$\frac{\Gamma_v}{U_\infty a} = \frac{\Gamma_c(r_{\max})}{U_\infty a}\Big|_{\max} - \frac{\Gamma_c(r_{\min})}{U_\infty a}\Big|_{\min} \ , \tag{4.3.2}$$

where $r_{\max}$ and $r_{\min}$ are chosen to maximize Eq. 4.3.2 in the wake. The data in Fig. 4.13 is typical of the variation of $\Gamma_c/U_\infty a$ with radius of integration r/a at a constant phase. Figure 4.14 is the streamline pattern related to the data in Fig. 4.13. From data like Fig. 4.13, the estimated strength of the vortical structures is

$$\frac{\Gamma_v}{U_\infty a} \approx 1 \tag{4.3.3}$$

In addition, from the slope of the contours in Fig. 4.15,

$$\frac{d(r/a)}{d(ft)} = 2\frac{\lambda_x}{S_f} \ ,$$

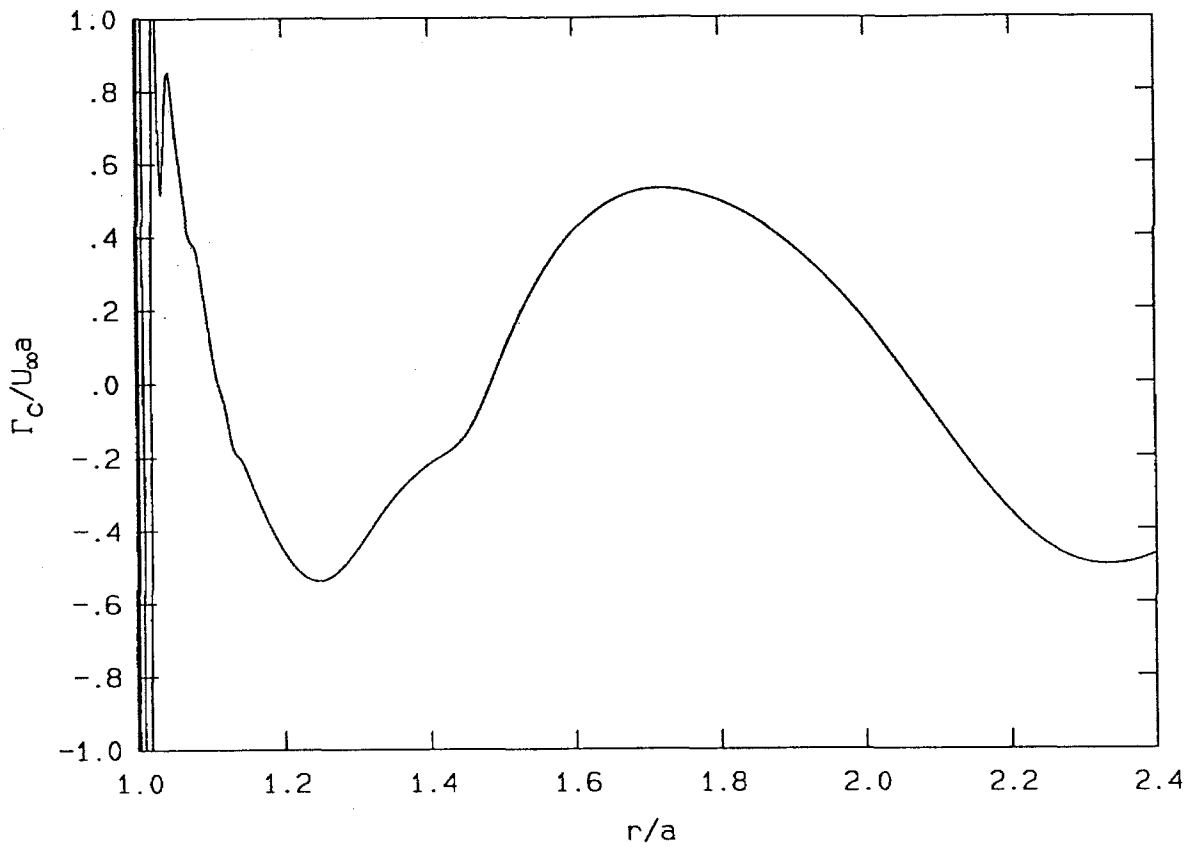

FIG. 4.13 *Variation of the normalized circulation, $\Gamma_c/U_\infty a$, taken round contours of varying radius, r/a ($ft = 0.54$). The rise in the curve between $r/a = 1.2$ and 1.7 marks a patch of positive (clockwise) circulation and the drop between $r/a = 1.7$ and 2.3 a negative (counter-clockwise) patch. cf.* Fig. 4.14.

it is found that the average (normalized) convection speed of the vortices in the near wake, based on the slope of the $\Gamma_c/U_\infty a = 0$ contour, is

$$\lambda_x \approx 0.6 , \qquad \text{for} \qquad \frac{r}{a} > 1.2 . \tag{4.3.4}$$

The transverse spacing of the vortices was difficult to estimate but appeared to be in the range

$$0.2 < \lambda_y < 0.3 , \tag{4.3.5}$$

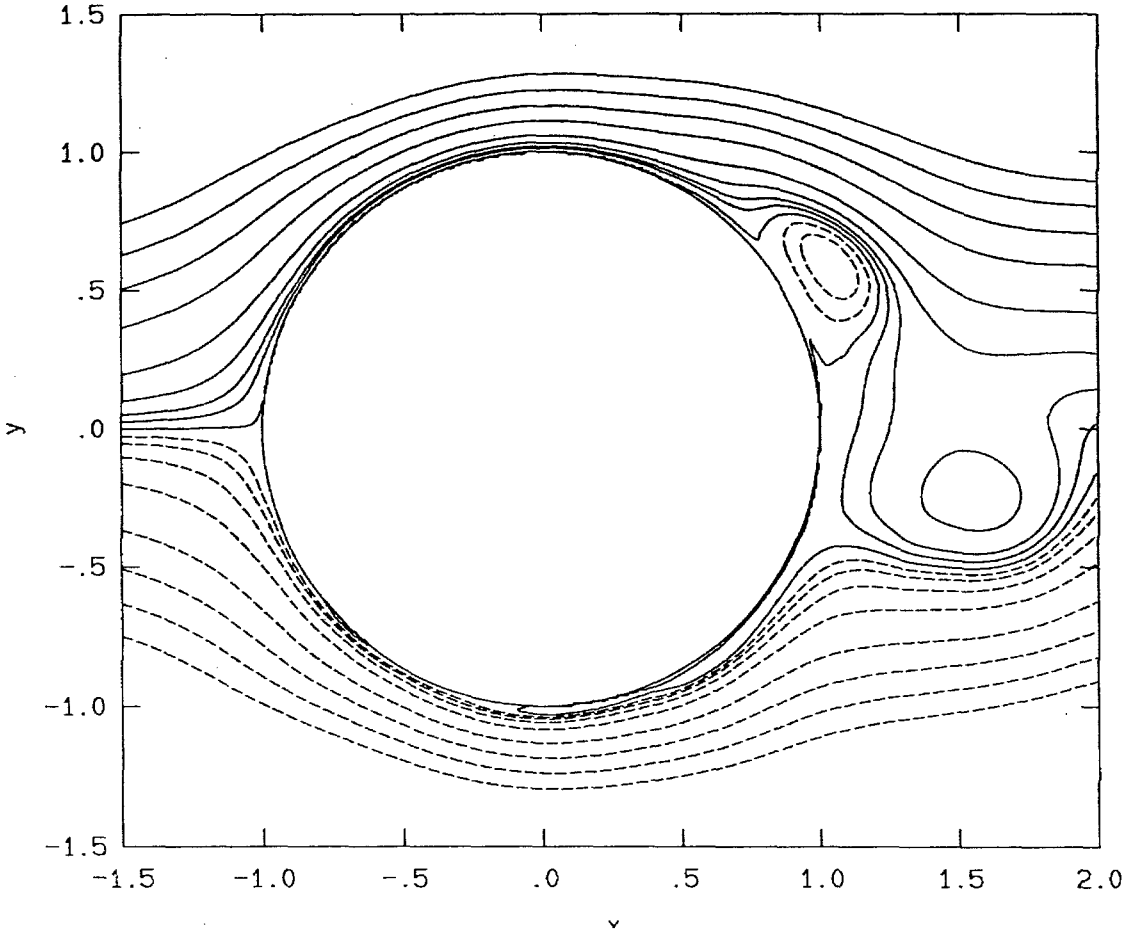

FIG. 4.14 Streamline pattern associated with the data in Fig. 4.13 ($ft = 0.54$).

Interestingly, using the method of Sec. 3.3.3, p. 3.17, for the periodic vortex street yielded estimates close to Eq. 4.3.3. Using Eq. 3.3.7, and λ_x and λ_y from Eqs. 4.3.4 and 4.3.5, yielded an estimate for the strength of the shed vortical structures,

$$1.1 < \frac{\Gamma_v}{U_\infty a} < 1.4 , \tag{4.3.6}$$

and similarly for the simplified estimate, Eq. 3.3.12, which takes no account of the

transverse spacing, a value

$$\frac{\Gamma_v}{U_\infty a} \approx 1.0 \,. \tag{4.3.7}$$

What is remarkable is that very little of the circulation, calculated at the cylinder surface, actually finds its way into the flow. If all of the circulation of a particular sign created during a forcing period and due to the angular acceleration of the cylinder where put into alternating vortices Eq. 3.3.16 would indicate a vortex strength of up to

$$\frac{\Gamma_v}{U_\infty a} = 4\pi\,\Omega_1 \approx 25 \tag{4.3.8}$$

for the data in this chapter. For the forced case presented in this chapter, the strength of the vortical structures shed into the wake is only about 4% of this value.

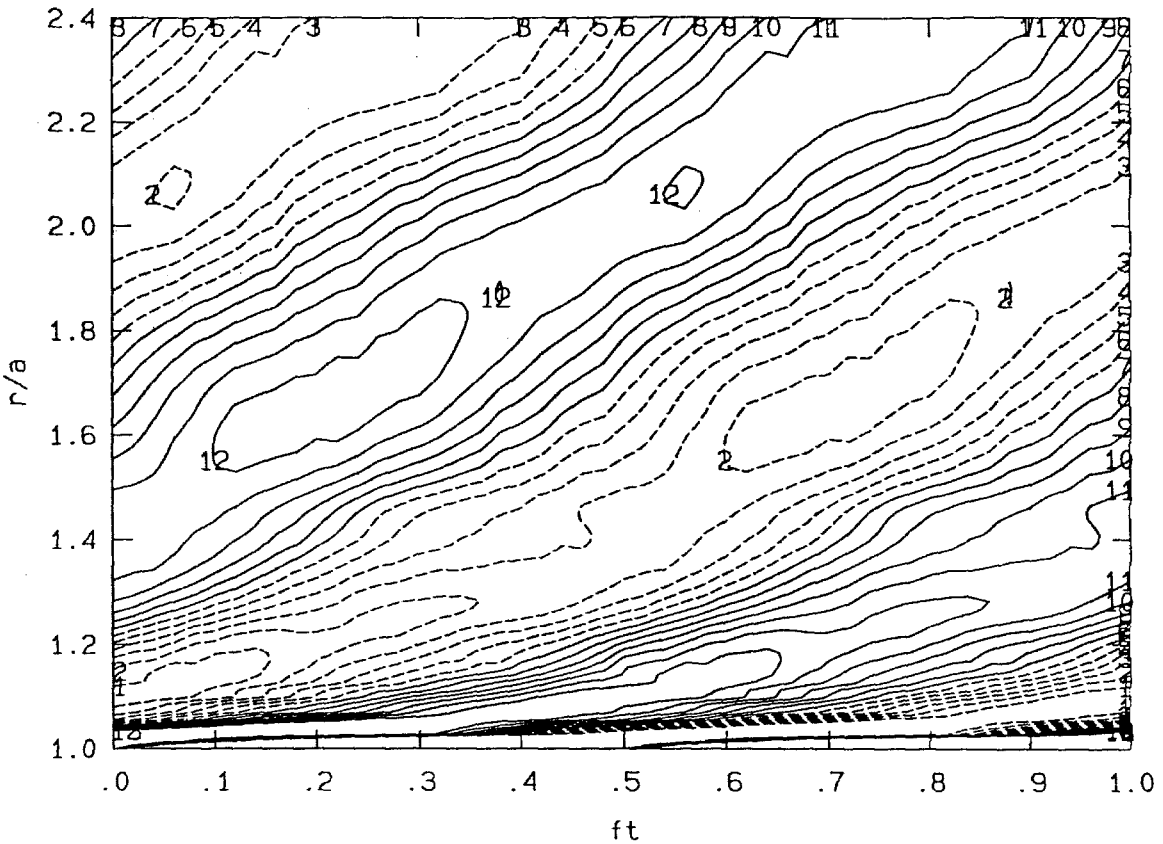

FIG. 4.15 $\Gamma_c/U_\infty a$ *vs.* r/a and ft. The dashed lines denote net counter-clockwise rotation; the solid lines, clockwise. The value $\Gamma_c/U_\infty a$ at contour level '1' $= 0.6$, '2' $= 0.5$, '3' $= 0.4$ ..., down to, '13' $= -0.6$. Contour level '7', solid line, marks the zero contour.

CHAPTER 5

Lifting cylinder

5.1 Preface

In this chapter, a novel method for estimating the lift on the cylinder is presented. The data calculated using this method compare favorably with similar data published for steadily rotating cylinders. In addition, the effect of superimposing forced rotary oscillations on the steady rotation of the cylinder is also presented; *i.e.*, a cylinder rotary motion of,

$$\dot{\theta}(t) = \frac{U_\infty}{a} \left[\Omega_0 + \Omega_1 \sin(2\pi f t) \right] , \tag{5.1.1}$$

where $\dot{\theta}$ is the angular velocity of the cylinder, Ω_0 and Ω_1 are the normalized amplitudes of the steady and oscillating components of the rotation, and f is the forcing frequency.

5.2 Experimental Setup

The experiments documented in this chapter were performed in the GALCIT $20'' \times 20''$ Free Surface Water Tunnel (*cf.* the LSWC used for the wake measurements in Ch. 3).

The cylinder used for the near wake velocity measurements is machined Plexiglas cylinder, $1''$ in diameter ($AR = 18.7$), and mounted and driven by the apparatus described in Ch. 2. The command signal for the cylinder velocity was generated by a computer-controlled function generator. The position of the cylinder output by the BEI 13-bit absolute position encoder was read using the computer's parallel interface.

Velocities were measured using a two-channel (u, v), laser Doppler velocimeter. The optics, traverse and analog/digital LDV processor, outlined below, are from Lang's (1985) thesis. The u-channel was only used to measure the free stream velocity. The v-channel velocities were used to estimate the lift coefficient. The v-channel was Bragg cell frequency-shifted. A Lexel Model 85 Argon-ion laser operating in single line mode (514.5 nm) at about 200 mW was used for the LDV. The laser beam for the LDV velocity measurements was split into four beams of nearly equal intensity using two cube beam splitter in series mounted in series at $+45°$ and $-45°$ respectively. The beams for the v-channel were then Bragg cell frequency-shifted to allow for flow reversals. The Bragg cell offset between the two beams was 300 kHz for the data presented in this chapter. Each of the four beams was then aligned (to insure that they intersect in a single focal volume) by passing them through wedge prisms. An achromat was used to focus the beams in a focal (measurement) volume located in the midspan plane of the FSWT. The light scattered from the focal volume was gathered by an achromat and focused on a pho-

todiode with an integral low noise pre-amplifier designed by Dan Lang. The signal from the pre-amplifier was then band-pass filtered above and below the frequency corresponding to the mean flow velocity to isolate the u-velocity and around the Bragg offset to isolate the v-velocity. The band-pass ranges were chosen to pass instantaneous velocity fluctuations and were non-overlapping.

For the data in Figs. 5.2, 5.3, and 5.4, the u- and v-channel outputs from the band pass filters were then passed thorough a pair of transimpedance amplifiers (Lang 1985) before being sent to the analog/digital LDV processor (Lang 1985). The signals were then processed by an analog and digital LDV processor and the velocity data was stored to disk using data acquisition software written by Dan Lang. See Lang (1985) for a complete description of the analog/digital signal processing hardware. Each data point in Fig. 5.2 is an average over about 10,000 (instantaneous) velocity measurements.

For the data in Figs. 5.5, 5.7, 5.8, and 5.9, a pair of tracking phase-locked loops designed by Dan Lang and Paul Dimotakis were used to lock TTL square waves to the dominant u- and v-channel frequencies from the band-pass filters. The TTL signals were then read by a (multiple) counter-timer board on a data acquisition computer and stored on disk for later processing.

Flow visualization was accomplished by introducing red dye into the flow ahead of the cylinder through a hypodermic tube. A blue filter was used to darken the red dye marker relative to the white background. Photographs were taken using a 35mm camera. Illumination was provided from behind by a large (backlit) white sheet of paper suspended, outside the water tunnel, behind the model.

5.3 Lift estimation by the virtual vortex method

Since the cylinder in the present experiments experiences no net rotational acceleration it cannot shed any (net) vorticity into the wake, in the mean. It follows that the net circulation in the wake cannot contribute to Γ. As a consequence, the vorticity contributing to Γ must be restricted to a relatively small neighborhood around the cylinder. This suggests that the effect on the flow, some distance from the lifting body, can be approximated, in a multipole expansion sense, by a single virtual vortex of strength Γ. It is also reasonable to expect that this virtual vortex resides somewhere within the cylinder boundaries.

Ideally, in an infinite domain, the velocity $v(x, y = 0)$, a distance x upstream of a vortex center is

$$v = -\frac{\Gamma}{2\pi x} . \tag{5.3.1}$$

Using Eqs. 1.2.5 and 5.3.1, v can be written in terms of the lift coefficient, C_L. For the infinite domain case this can be written as

$$\frac{v(x)}{U_\infty} = \frac{C_L}{2\pi}\frac{x}{a} . \tag{5.3.2}$$

Because of the finite height of the test section, a proper account should include spatially periodic image vortices located above and below the cylinder. See Fig. 5.1. Equation 5.3.1 is then replaced by

$$v = -\frac{\Gamma}{2h}\,\mathrm{csch}\left(\pi\frac{x - x_0}{h}\right) , \tag{5.3.3}$$

where h is the test section height and x_0 is the streamwise position of the virtual

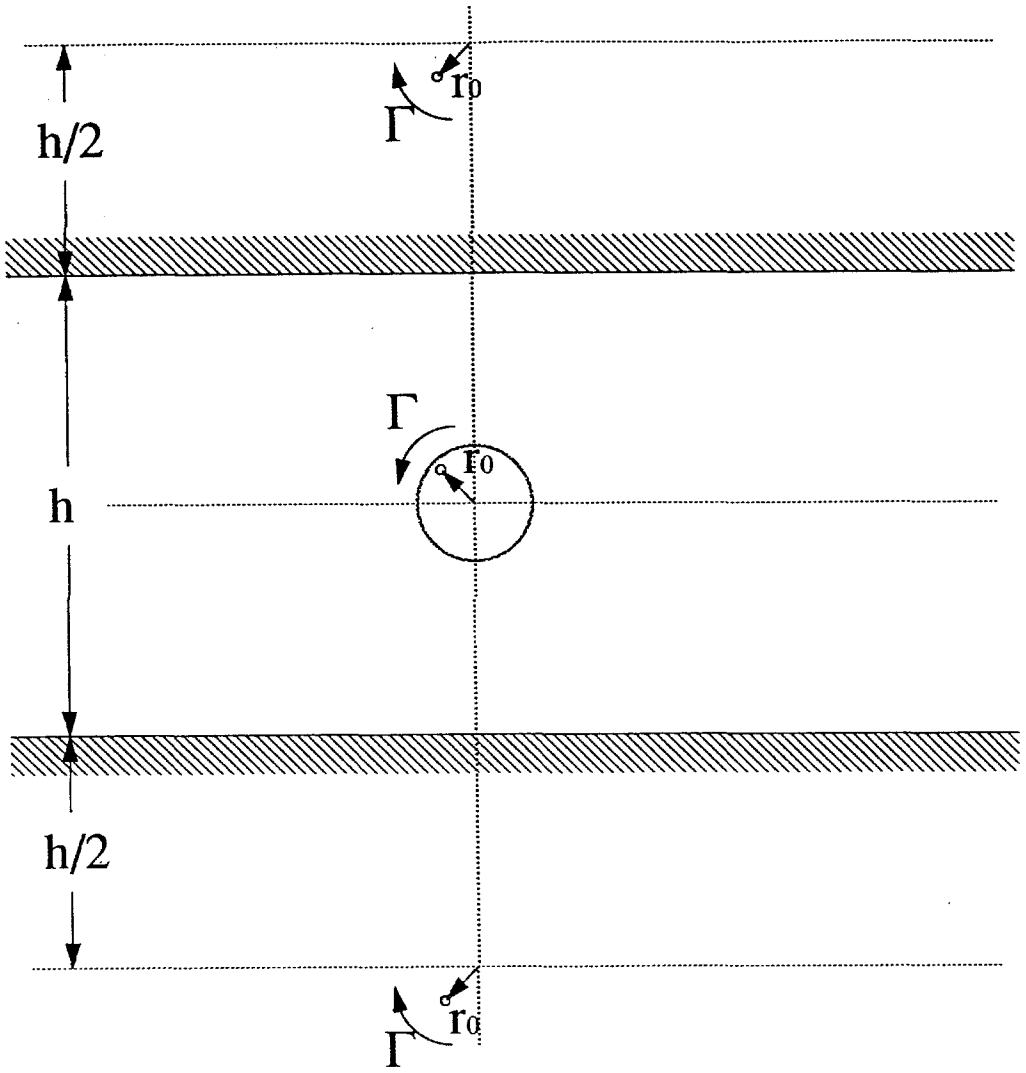

FIG. 5.1 Diagram of periodic image vortices. Only the image vortices immediately above and below are pictured. The shaded circle denotes the cylinder (not to scale), and the smaller circles the virtual vortex and its images.

vortex.* Rearranging Eq. 5.3.3 yields,

$$\frac{2h\,v}{\Gamma} = -\operatorname{csch}\left(\pi\,\frac{x-x_0}{h}\right)\,, \tag{5.3.4}$$

* A transverse displacement of the virtual vortex from the cylinder axis, y_0, is a higher order effect.

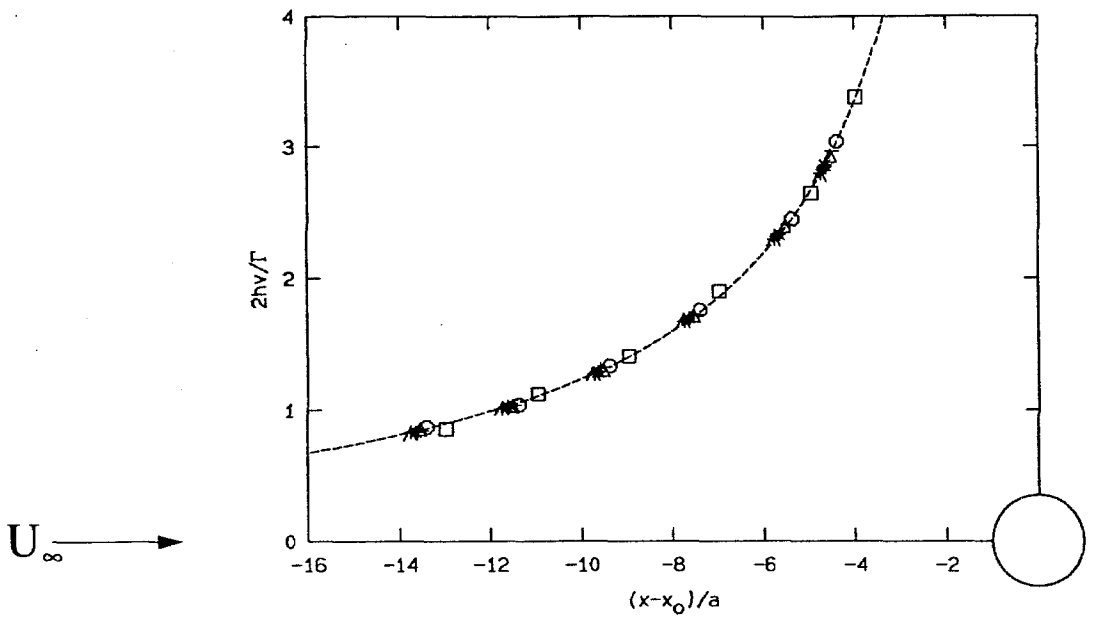

FIG. 5.2 Normalized transverse velocity ahead of a cylinder executing steady rotation ($\Omega_1 = 0$): $2h\,v/\Gamma$ *vs.* $(x - x_0)/a$, $Re = 3.8 \times 10^3$. $\Omega_0 = 0.5$ (□), 1.5 (○), 2 (△), 2.5 (+), 3 (→), 4 (◇), 5 (*), 6 (∧), 8 (|), 10 (−), and $\Omega_1 = 0$. The dashed line is $\mathrm{csch}(\pi(x - x_0)/h)$.

or, using Eq. 1.2.5,

$$\frac{v}{U_\infty} = \frac{a}{2h}\, C_L\, \mathrm{csch}\left(\pi \frac{x - x_0}{h}\right) . \tag{5.3.5}$$

The transverse velocity was measured at several locations ahead of the cylinder axis, for a range of $0.5 \leq \Omega_0 \leq 10$. The validity of Eq. 5.3.3 as a model for the decrease in the velocity ahead of the cylinder is demonstrated in Fig. 5.2, a plot of $2hv/\Gamma$ *vs.* $(x - x_0)/a$. The parameters h, a, and x were known *a priori* and v/U_∞ was measured. Γ and x_0 were determined using Eq. 5.3.5 and a version of the Levenberg-Marquardt nonlinear least-squares fit routine from Press *et al.* (1986). Figure 5.3 compares the data of Reid (1924) with C_L determined from the

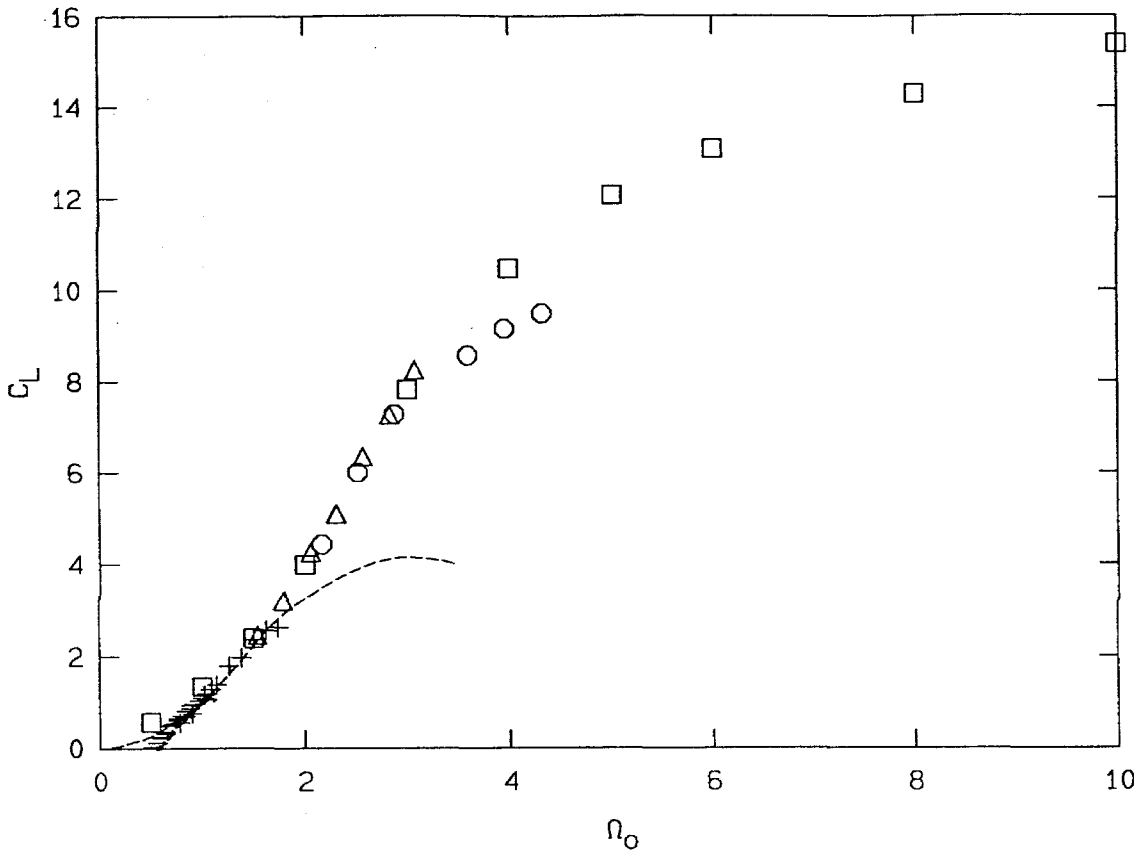

FIG. 5.3 C_L based on data fit in Fig. 5.2 $Re = 3.8 \times 10^3$, $\Omega_1 = 0$, $AR = 18.7$ (□). Data of Reid (1924) $AR = 13.3$, $Re = 4.0 \times 10^4$ (○), $Re = 5.6 \times 10^4$ (△), $Re = 7.9 \times 10^4$ (+), $Re = 1.2 \times 10^5$ (→). Data of Prandtl $AR = 4.7$, $Re = 5.2 \times 10^4$ (– – –).

nonlinear least squares curve-fit.

The curve-fit data also show that the centroid of the virtual vortex, x_0, is slightly ahead of the cylinder axis. See Fig. 5.4. The centroid appears to be slightly ahead of the cylinder *body*, *i.e.*, $x_0/a > 1$, at the lowest value of Ω_0 (=0.5). Ideally, this should not occur. The velocities being measured in that case, however, are small ($0.004 < v/U_\infty < 0.02$) and errors of this order cause anomalies in the fit parameters.

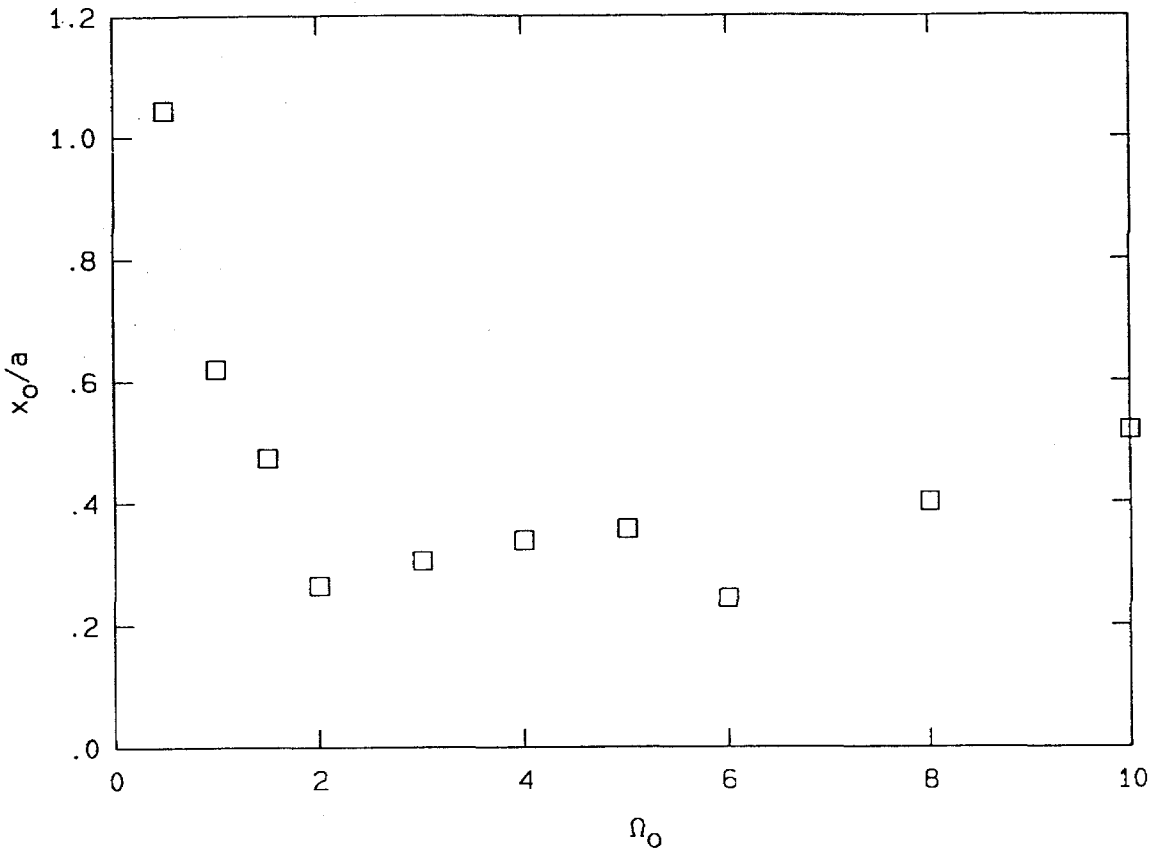

FIG. 5.4 Centroid of the virtual vortex, x_0, based on the data fit in Fig. 5.2.

In the following sections, C_L is estimated using a single velocity ahead of the cylinder, and taking the centroid of the virtual vortex to be on the cylinder axis. In addition, the other parameters were set at $x/a = 10$, $h/a = 40$, $x/h = 0.25$ and $a/h = 0.025$.

5.4 Steady rotation: $\Omega_1 = 0$.

Figure 5.5 shows the lift calculated using Eq. 5.3.5 with $x_0 = 0$ and v/U_∞ measured at $x/a = 10$. The published data of Prandtl (1925) and Reid (1924) are shown for reference. Note that the present data seem to overestimate C_L at the lowest values of Ω_0. This may partially be attributable to the fact that the origin of the virtual vortex is not on the cylinder axis. However, the fact that the data of Prandtl (1925) and Reid (1924) show a *negative* C_L, at the lowest values of Ω_0, suggests that the lower Reynolds number in the present experiments may also be a factor. Note that Tritton (1977) reports that a *sphere* also experiences a lift in the "wrong" direction at low rotation rates and higher Re because of a turbulent separation on the side of the sphere moving opposite to the flow. As can be seen from the data, Fig. 5.5, larger cylinder aspect ratios (AR) yield larger maximum lift coefficients ($C_{L_{\max}}$). Compare the data in the present experiments employing a cylinder with a larger $AR = 18.7$ with the data of Reid ($AR = 13.3$) and Prandtl ($AR = 4.7$).

Recall that Goldstein (1938), in an interpretation of an intuitive argument given by Prandtl (1925), suggested that $C_{L_{\max}} = 4\pi \approx 12.6$. The present data which show the estimated C_L exceeding 4π casts doubt on this proposed upper limit. Note that the value of C_L measured at the highest value of Ω_0 exceed "$C_{L_{\max}}$" by almost 25%. In addition, the trend suggests that the estimated C_L can be made even larger by increasing Ω_0 beyond 12.

It should be noted that in real flow, diffusion and unsteady flow processes can transport vorticity away from the cylinder at start-up, weakening Prandtl's proposed $C_{L_{\max}}$ (Eq. 1.2.7). A more plausible explanation is that three-dimensional (end) effects will tend to reduce the mean spanwise lift measured at a particular

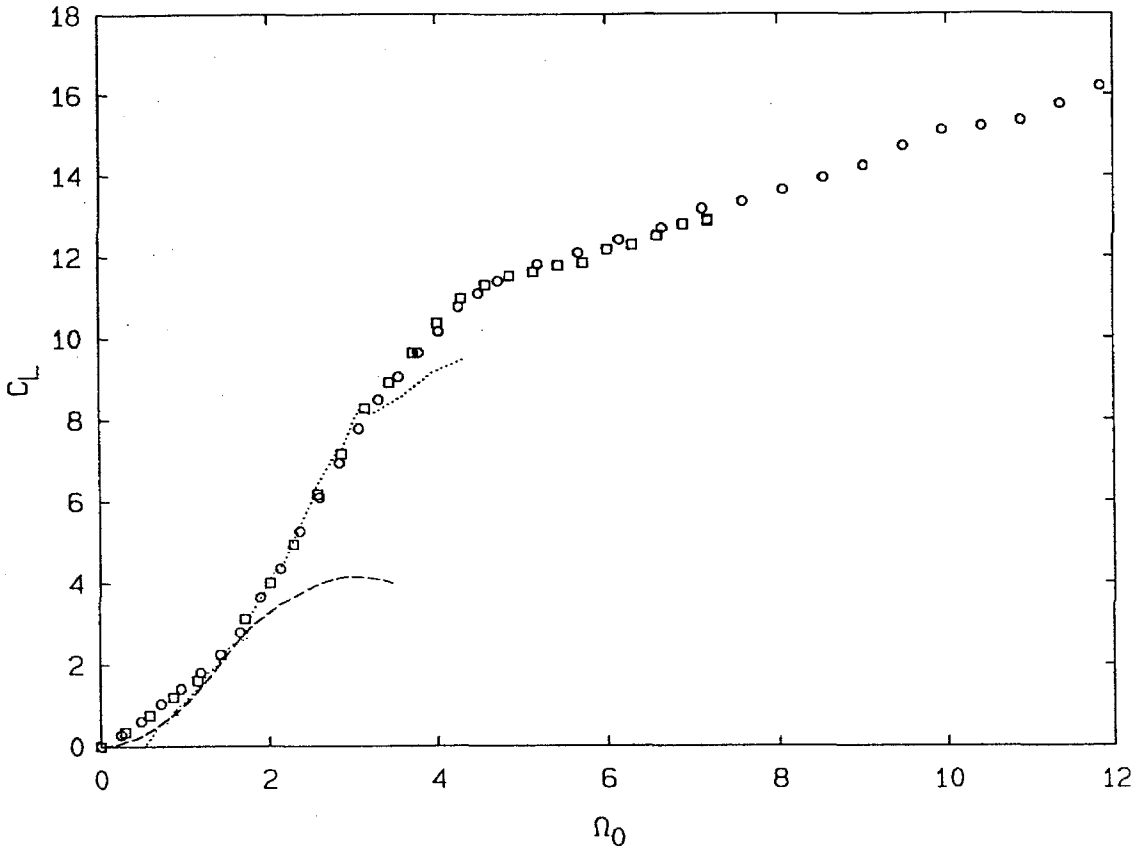

FIG. 5.5 Comparison with published data of C_L *vs.* Ω_0 for steadily rotating cylinders whose ends are flush with the test section walls. Present data (circles) $Re = 4.2 \times 10^3$, (squares) $Re = 6.8 \times 10^3$, $AR = 18.7$, in water. Data of Reid, (dots) $Re = 4.0 \times 10^4 < Re < 1.2 \times 10^5$, $AR = 13.3$, in air. Data of Prandtl (dashes), $Re = 5.2 \times 10^4$, $AR = 4.7$, in air.

rotation rate to below that which could be attained in a two-dimensional flow. Thom (1926) showed that the sectional lift coefficient decreased toward the ends of a rotating cylinder. It is interesting that Goldstein also relates how Prandtl, in one of his experiments, associated the limiting of $C_{L_{\max}} (= 4)$ with a separation of the flow from the side walls of the test section. To remedy this situation, Prandtl added co-rotating end disks to the cylinder and then observed an increased $C_{L_{\max}} (= 10)$. No further note was made of the end effects for that configuration.

5.5 Rotation with forced oscillations: $\Omega_1 \neq 0$, $S_f = 0.7$.

For the data presented in this section, the forcing Strouhal number,

$$S_f \equiv \frac{2af}{U_\infty} ,$$

was fixed at a value of 0.7, while the steady and fluctuating components of the rotary motion were varied.

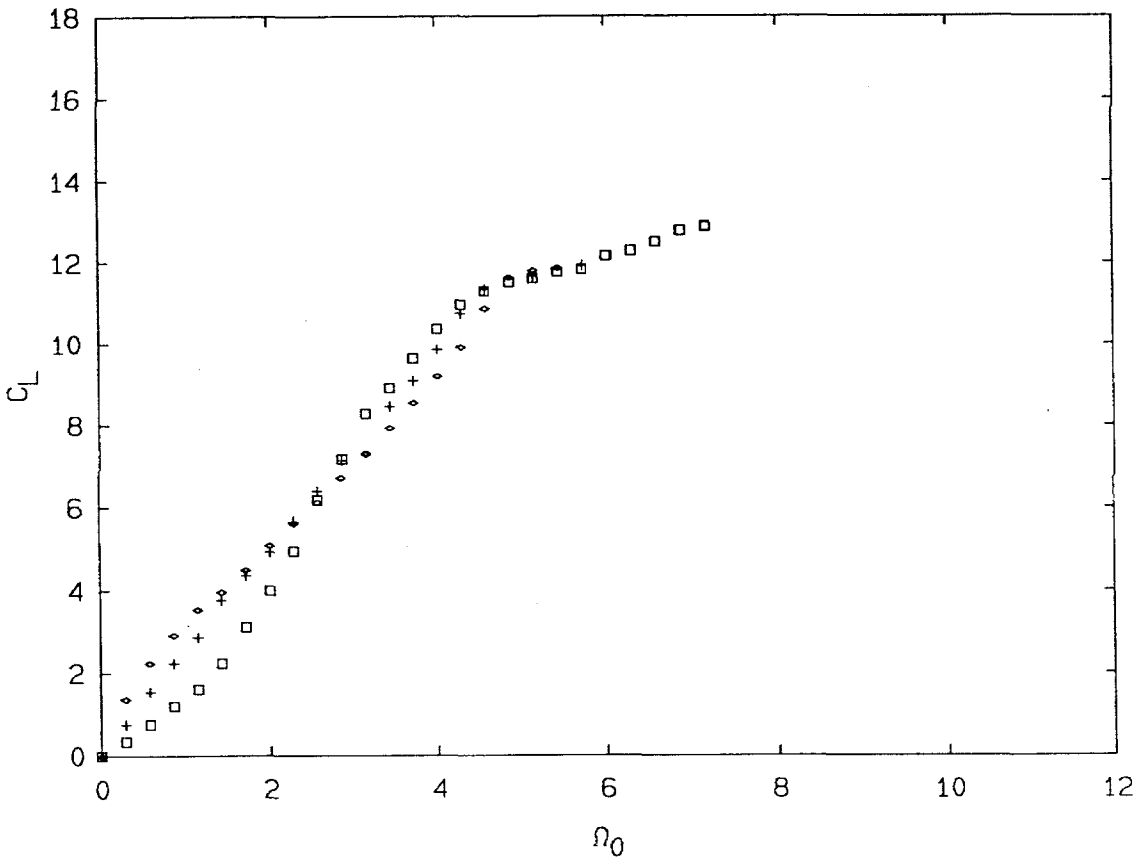

FIG. 5.7 Comparison of C_L *vs.* Ω_0 data for several amplitudes of oscillations, with constant forcing frequency and Reynolds number ($S_f = 0.7$, $Re = 6.8 \times 10^3$). Squares: $\Omega_1 = 0$, crosses: 1.2, and diamonds: 2.3.

FIG. 5.6 Flow visualization for various mean rotation rates (Ω_0). With oscillations (left, $\Omega_1 = 2.1$, $S_f = 0.7$), and without (right, $\Omega_1 = 0$), *cf.* stars and circles in Fig. 5.8. From top to bottom, the mean (normalized) rotation rate is $\Omega_0 = 0$, 1, 2, 3, 4, and 5. $Re = 4.1 \times 10^3$. Note that the picture on the top right corner is the unforced (non-rotating) case.

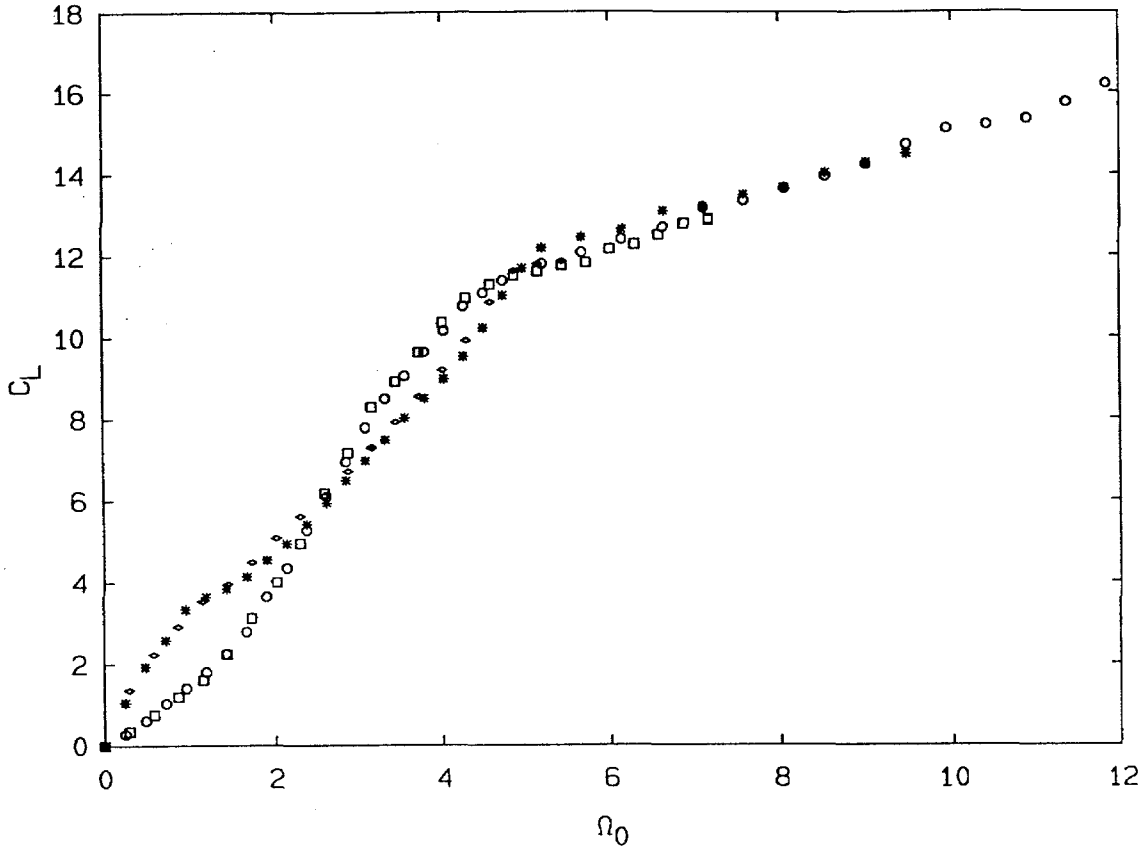

FIG. 5.8 Comparison of C_L *vs.* Ω_0 data for the steady case and an oscillating case, at two Reynolds numbers. Steady rotation: (circles) $Re = 4.2 \times 10^3$, $\Omega_1 = 0$, (squares) $Re = 6.8 \times 10^3$, $\Omega_1 = 0$. Net rotation with oscillations. (stars) $Re = 4.2 \times 10^3$, $\Omega_1 = 2.1$, $S_f = 0.7$, (diamonds) $Re = 6.8 \times 10^3$, $\Omega_1 = 2.3$, $S_f = 0.7$.

It was found that forced rotary oscillations increased C_L for $0 < \Omega_0 < 2.5$ and decreased it for $2.5 < \Omega_0 < 4.5$. See Fig. 5.7. It is no coincidence that for the steadily rotating case, $\Omega_1 = 0$, the cylinder has noticeable vortex shedding for $\Omega_0 < 2.5$, and none for $\Omega_0 > 2.5$. Flow visualization (Fig. 5.6) shows that for $\Omega_0 < 2.5$, forced oscillations of the cylinder help close the wake, creating a flow that, on average, is closer to potential. In contrast, for $2.5 < \Omega_0 < 4.5$, where the wake would normally close with steady rotation alone, oscillations hinder this effect. The data for the three cases presented in Fig. 5.7 coincide for $\Omega_0 > 4.5$, *i.e.*,

the oscillations of the cylinder have little effect on the lift beyond this point.

There is a cross-over region of the C_L *vs.* Ω_0 curve at Ω_0 between 2 and 4. The data in Figs. 5.7 and Fig. 5.8 suggest that C_L in that region is not a strong function of the forcing amplitude or the Reynolds number. While there is an indication in Fig. 5.6 (c) that the forced oscillation frequency (S_f) and the natural shedding frequency (S_n) are close below the cross-over region ($\Omega_0 < 2.5$), estimates of C_L varied little with S_f in that region. See Fig. 5.9 (squares).

As can be seen in Fig. 5.8, the data for $Re = 4.2 \times 10^3$, and $Re = 6.8 \times 10^3$ are close, except for a slightly delayed break in the lift curve around $\Omega = 4.5$ for $Re = 4.2 \times 10^3$. This is possibly due to a delayed boundary layer separation from the test section walls in the latter case.

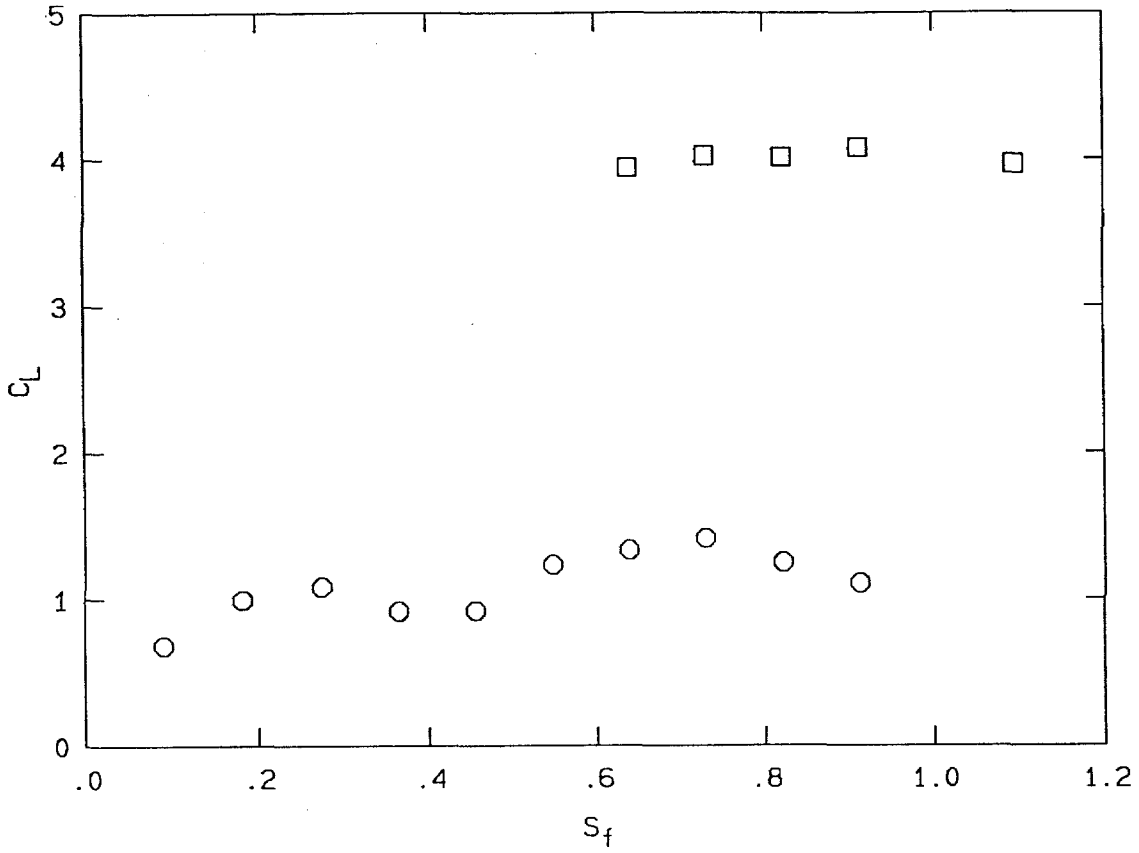

FIG. 5.9 The effect on C_L of varying S_f. Circles: $\Omega_0 = 0.3$, squares: $\Omega_0 = 1.4$ ($Re = 6.8 \times 10^3$, $\Omega_1 = 2.3$).

CHAPTER 6

Conclusions

The type of active program control of the flow described in the present experiments relies on the forces between the cylinder and the surrounding flow. It is this interaction that regulates the ejection of circulation into the separated flow region and actuates the entire flow field. This is exemplified by the control of the wake structure demonstrated in Chs. 3 - 5 as well as the up-stream influence characterized in Ch. 5. In addition, the way this type of control exploits the natural tendency to have vortical structures in the flow is in contrast to the more traditional control philosophy that unsteadiness is something that should be canceled, *e.g.*, the feed-forward control employed by Liepmann, Brown & Nosenchuck (1982) and Liepmann & Nosenchuck (1982), and the feedback control employed by Ffowcs-Williams & Zhao (1989).

In Ch. 3, the efficacy of oscillatory cylinder rotation as an actuation mechanism for actively controlling the cylinder wake was examined. It was found that considerable control could be exercised over the structure in the wake with such forcing. In particular, a large increase, or decrease, in the resulting displacement thickness, estimated cylinder drag, and associated mixing with the free stream can be achieved, depending on the frequency and amplitude of oscillation. Not surprisingly, the present results show that working in a control domain in which the structures shed are synchronous with the forcing provides the greatest control authority over the wake structure. In addition, while these results were obtained for

moderate Reynolds numbers, *i.e.* $Re \sim 10^4$, there are indications that the description of the flow phenomena presented here is qualitatively the same over a large range of Reynolds numbers. The streamline data in Ch. 4 show that under control (forcing), the vortical structures are formed very close to the cylinder. This is an indication that the formation of the wake structure, under control, has more to do with the controlled ejection of circulation, and the associated forces on the body, than with the stability characteristics of some generic unforced wake. This forced shedding is in contrast to the natural (unforced) shedding of vortices, where the structures form only after the vorticity has been shed into the wake, from more-or-less steady separation points. Hence, it is possible that the stability characteristics of the wake can play a more significant role in the unforced case than in the forced. In addition, it is shown that under control, very little of the circulation introduced at the cylinder wall appears in the wake. Evidently, most of the positive and negative vorticity introduced into the boundary layer fluid combines before the fluid is allowed to enter the wake.

The virtual vortex method explored in Ch. 5 was found to be successful in characterizing flow ahead of the cylinder. In addition, the method yields estimates for C_L which which agree with the data published by Thom (1924) for lift coefficients greater than 2, *i.e.*, $\Omega_0 > 1$. While the method seems to overestimate C_L at the smaller values of $\Omega_0 < 1$, it is not certain whether this is due to a failure in the method, a difference in Re between the experiments, or a pronounced variation of the sectional lift coefficient along the cylinder span (Thom 1926). The C_L calculated at the larger values of Ω_0 were also found to be greater than in the published data, but this was probably due to the larger aspect ratio of the cylinder in the present experiments. In addition, the maximum (obtainable) lift coefficient proposed by Prandtl (1925), was exceeded in the present experiments, possibly because Prandtl's arguments neglected unsteady effects. Finally, it was found that the

addition of forced rotary oscillations to the steady rotation of the cylinder increased C_L in cases where the wake would normally be separated (in the steadily rotating case), but decreased it otherwise.

APPENDIX A

Forces on a body

This appendix was extracted form notes collected over the course of the present investigations. This particular segment of the notes was chosen because it lends support to the "virtual vortex method" used in Ch. 5. In addition, it shows how the unsteady circulation around the body is related to the unsteady forces.

A.1 Forces in three-dimensional flow

The unsteady force on a body moving through an incompressible flow (For steady case see Milne-Thomson 1968, p. 672), can be written as

$$\mathbf{F}_B = -\rho \frac{d}{dt} \int_V \mathbf{u}\, dV + \int_\sigma [-p\,\mathbf{n} - \rho\,\mathbf{u}(\mathbf{u}\cdot\mathbf{n}) + \mu\,\boldsymbol{\omega}\times\mathbf{n}]\, dS\,, \qquad \text{(A.1.1)}$$

where, V is a volume surrounding, but not including, the body, σ is the surface enclosing V and the body, ρ is the fluid density, $\mathbf{u}$ is the velocity, p is the pressure, μ is the viscosity, $\boldsymbol{\omega} \equiv \nabla \times \mathbf{u}$ is the vorticity, and $\mathbf{n}$ is the outward normal to the surface σ. See Fig. A.1.

If β, the Bernoulli constant, is defined as

$$\beta \equiv p + \frac{1}{2}\rho\,(\mathbf{u}\cdot\mathbf{u}) - p_\infty - \frac{1}{2}\rho\,(\mathbf{U}_\infty\cdot\mathbf{U}_\infty)\,, \qquad \text{(A.1.2)}$$

Eq. A.1.1 can be rewritten as

$$\mathbf{F}_B = -\rho \frac{d}{dt} \int_V \mathbf{u}\, dV + \int_\sigma \left[-\beta\mathbf{n} + \frac{1}{2}\rho\,(\mathbf{u}\cdot\mathbf{u})\,\mathbf{n} - \rho\mathbf{u}(\mathbf{u}\cdot\mathbf{n}) + \mu\,\boldsymbol{\omega}\times\mathbf{n}\right] dS\,. \qquad \text{(A.1.3)}$$

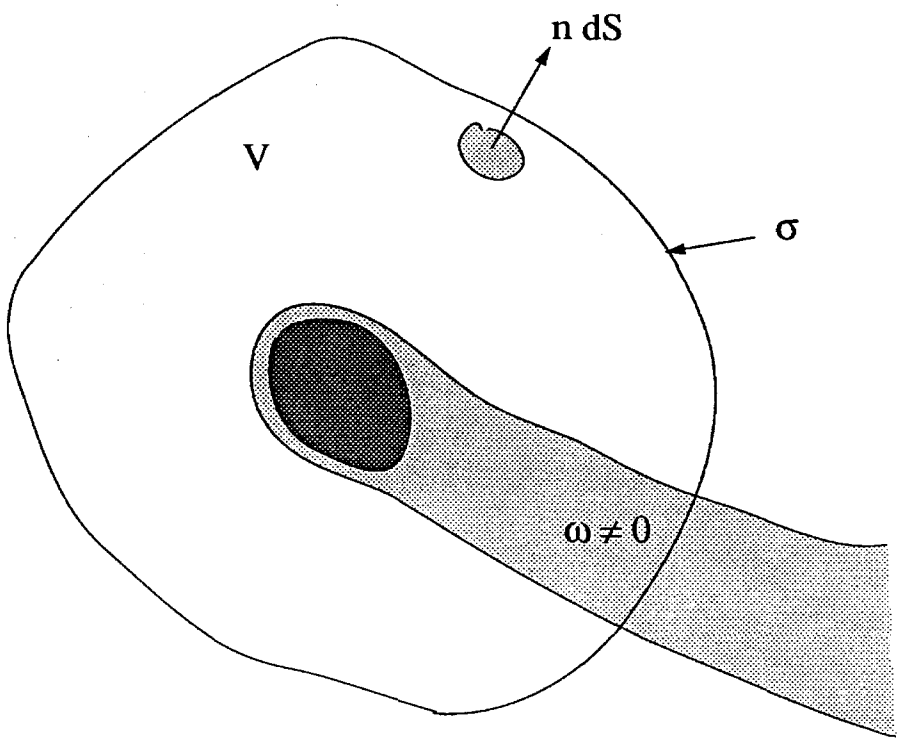

FIG. A.1 3-D Geometry.

Note that the nonlinear terms in Eq. A.1.3 can be written (Milne-Thomson 1968, p.68) as

$$\int_\sigma \mathbf{u}\,(\mathbf{u}\cdot\mathbf{n})\;dS - \int_\sigma \frac{1}{2}\,(\mathbf{u}\cdot\mathbf{u})\,\mathbf{n}dS \;=\; \int_V \boldsymbol{\omega}\times\mathbf{u}\,dV + \int_V \mathbf{u}(\nabla\cdot\mathbf{u})\;dV\;. \quad \text{(A.1.4)}$$

Then, noting also that the last term in Eq. A.1.4 is zero in incompressible flow, we have

$$\mathbf{F}_B \;=\; -\rho\frac{d}{dt}\int_V \mathbf{u}\,dV \;+\; \int_\sigma [-\beta\mathbf{n} + \mu\,\boldsymbol{\omega}\times\mathbf{n}]\;dS \;+\; \rho\int_V \mathbf{u}\times\boldsymbol{\omega}\,dV\;. \quad \text{(A.1.5)}$$

In order to extract the "classic" Lift$=\rho U_\infty\Gamma$ from the momentum equation, it is useful to subtract the free-stream velocity, $\mathbf{U}_\infty$, from the velocity field. Let

$$\mathbf{u}_0 \;\equiv\; \mathbf{u} \;-\; \mathbf{U}_\infty\;. \quad \text{(A.1.6)}$$

Noting that

$$\boldsymbol{\omega} \;=\; \nabla \times \mathbf{u} \;=\; \nabla \times (\mathbf{u}_0 + \mathbf{U}_\infty) \;=\; \nabla \times \mathbf{u}_0 \tag{A.1.7}$$

and also that the vector circulation may be defined as

$$\boldsymbol{\Gamma} \;\equiv\; \int_V \boldsymbol{\omega}\, dV \;=\; \int_V \nabla \times \mathbf{u}_0 \, dV \;, \tag{A.1.8}$$

the last term in Eq. A.1.5 can be written as

$$\begin{aligned} \int_V \mathbf{u} \times \boldsymbol{\omega}\, dV \;&=\; \int_V (\mathbf{U}_\infty + \mathbf{u}_0) \times \boldsymbol{\omega}\, dV \\ &=\; \mathbf{U}_\infty \times \int_V \boldsymbol{\omega}\, dV \;+\; \int_V \mathbf{u}_0 \times \boldsymbol{\omega}\, dV \\ &=\; \mathbf{U}_\infty \times \boldsymbol{\Gamma} \;+\; \int_V \mathbf{u}_0 \times (\nabla \times \mathbf{u}_0)\; dV \;. \end{aligned} \tag{A.1.9}$$

It is desirable to write the force in terms of surface integrals, so note that re-applying the identity (Eq. A.1.4) to $\mathbf{u}_0$, with $\nabla \cdot \mathbf{u}_0 \equiv 0$, yields for the last term in Eq. A.1.9

$$\int_V \mathbf{u}_0 \times (\nabla \times \mathbf{u}_0)\, dV \;=\; -\int_\sigma \mathbf{u}_0\, (\mathbf{u}_0 \cdot \mathbf{n})\, dS \;+\; \int_\sigma \frac{1}{2}\, (\mathbf{u}_0 \cdot \mathbf{u}_0)\, \mathbf{n}\, dS \;. \tag{A.1.10}$$

For ease of notation define the surface integral

$$\boldsymbol{\Sigma} \;\equiv\; \int_\sigma \frac{\mathbf{u}_0}{U_\infty} \left(\frac{\mathbf{u}_0}{U_\infty} \cdot \mathbf{n} \right) \frac{dS}{b\,a} \;-\; \frac{1}{2} \int_\sigma \left(\frac{\mathbf{u}_0}{U_\infty} \cdot \frac{\mathbf{u}_0}{U_\infty} \right) \mathbf{n}\, \frac{dS}{b\,a} \tag{A.1.11}$$

such that Eq. A.1.10 can be written as

$$\int_V \mathbf{u}_0 \times (\nabla \times \mathbf{u}_0)\, dV \;=\; -\rho\, U_\infty^2\, b\, a\, \boldsymbol{\Sigma} \tag{A.1.12}$$

where $2\,b\,a$ * is the frontal area of the body. This then yields for the force on a body in incompressible flow,

$$\mathbf{F}_B \;=\; -\rho\, \frac{d}{dt} \int_V \mathbf{u}_0\, dV \;+\; \int_\sigma \left[-\beta \mathbf{n} + \mu\, \boldsymbol{\omega} \times \mathbf{n} \right] dS \;+\; \rho \mathbf{U}_\infty \times \boldsymbol{\Gamma} \;+\; \rho\, U_\infty^2\, b\, a\, \boldsymbol{\Sigma} \tag{A.1.13}$$

---

* For the case of a circular cylinder, a is the radius and b is the span.

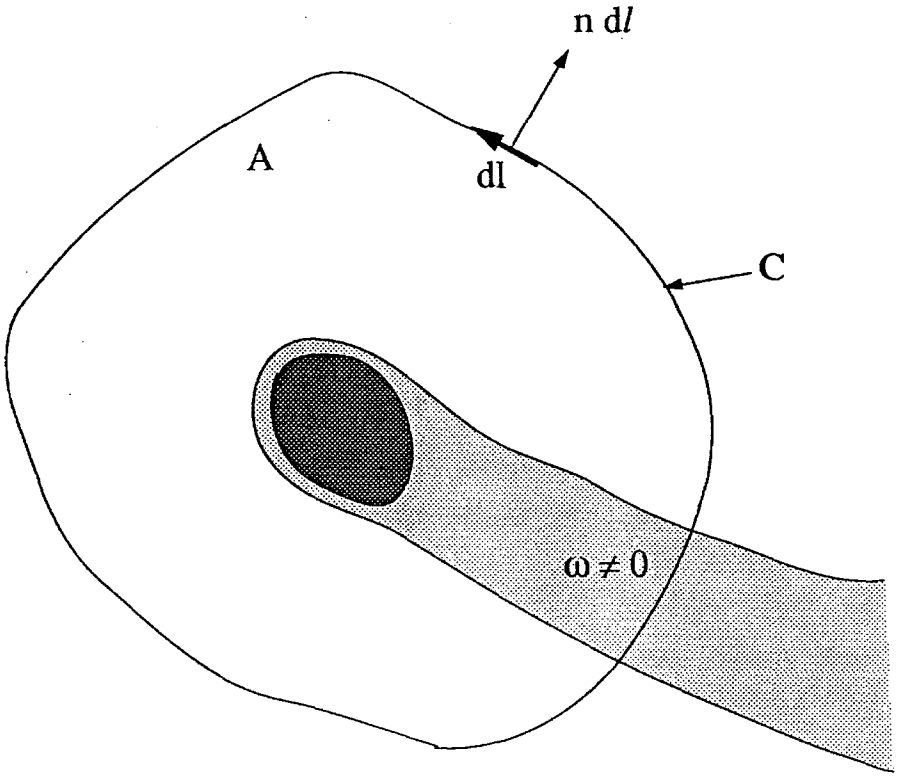

FIG. A.2 2-D Geometry.

A.2 Forces in two-dimensional flow

Writing this for two-dimensional flow,

$$\mathbf{\Gamma} \rightarrow \Gamma b\,\mathbf{e}_z \quad , \quad \boldsymbol{\omega} \rightarrow \omega\,\mathbf{e}_z \quad , \quad \mathbf{U}_\infty \rightarrow U_\infty\,\mathbf{e}_x \quad , \tag{A.2.1}$$

yields the force per unit span,

$$\mathbf{F}_B/b = -\rho\frac{d}{dt}\int_A \mathbf{u}\,dA - \int_C \beta\,\mathbf{n}\,dl - \rho U_\infty \Gamma\,\mathbf{e}_y + \mu\int_C \omega\,\mathbf{e}_z \times \mathbf{n}\,dl + \rho U_\infty^2 a\,\mathbf{\Sigma}_{2-D}\,, \tag{A.2.2}$$

where A is the two-dimensional cross-sectional area of the volume V, C is the boundary of A (See Fig. A.2), and

$$\mathbf{\Sigma}_{2-D} \equiv \int_C \frac{\mathbf{u}_0}{U_\infty}\left(\frac{\mathbf{u}_0}{U_\infty}\cdot\mathbf{n}\right)\frac{dl}{a} - \frac{1}{2}\int_C \left(\frac{\mathbf{u}_0}{U_\infty}\cdot\frac{\mathbf{u}_0}{U_\infty}\right)\mathbf{n}\,\frac{dl}{a}\,. \tag{A.2.3}$$

In terms of the force coefficient,

$$\begin{aligned}\mathbf{C}_{F_{2-\mathrm{D}}} \equiv & \frac{\mathbf{F_B}}{\frac{1}{2}\,\rho\, U_\infty^2 2a\, b} \\ = & -\frac{a}{U_\infty}\frac{d}{dt}\int_A \frac{\mathbf{u}}{U_\infty}\,\frac{dA}{a^2} \;-\; \int_C \frac{\beta}{\rho\, U_\infty^2\, a}\,\mathbf{n}\,\frac{dl}{a} \\ & -\frac{\Gamma}{U_\infty a}\,\mathbf{e}_y \;+\; \frac{2}{Re}\int_C \frac{\omega a}{U_\infty}\,\mathbf{e}_z \times \mathbf{n}\,\frac{dl}{a} \;+\; \boldsymbol{\Sigma}_{2-\mathrm{D}}\;.\end{aligned} \tag{A.2.4}$$

A.3 Lift coefficient

Calculating the lift coefficient,

$$\begin{aligned}C_L \;\equiv & \;\mathbf{C}_{F_{2-\mathrm{D}}}\cdot\mathbf{e}_y \\ = & -\frac{a}{U_\infty}\frac{d}{dt}\int_C \frac{v}{U_\infty}\,\frac{dA}{a^2} \;-\; \int_C \frac{\beta}{\rho\, U_\infty^2\, a}\,(\mathbf{n}\cdot\mathbf{e}_y)\,\frac{dl}{a} \\ & -\frac{\Gamma}{U_\infty a} \;+\; \frac{2}{Re}\int_C \frac{\omega a}{U_\infty}\,\frac{\mathbf{dl}\cdot\mathbf{e}_y}{a} \;-\; \boldsymbol{\Sigma}_{2-\mathrm{D}}\cdot\mathbf{e}_y\,,\end{aligned} \tag{A.3.1}$$

and following G. I. Taylor (1925), the β integral is eliminated by traversing the wake vertically, so that $(\mathbf{n}\cdot\mathbf{e}_y) = 0$ (recall that, by construction, $\beta = 0$ outside the wake). Then

$$C_L \;=\; -\frac{a}{U_\infty}\frac{d}{dt}\int_C \frac{v}{U_\infty}\,\frac{dA}{a^2} \;-\; \frac{\Gamma}{U_\infty a} \;+\; \frac{2}{Re}\int_C \frac{\omega a}{U_\infty}\,\frac{dy}{a} \;-\; \boldsymbol{\Sigma}_{2-\mathrm{D}}\cdot\mathbf{e}_y\;, \tag{A.3.2}$$

where

$$Re \;\equiv\; \frac{2\,a\,\rho\,U_\infty}{\mu}$$

is the Reynolds number.

Averaging Eq. A.3.2 yields

$$\overline{C}_L \;=\; -\frac{\Gamma}{U_\infty a} \;+\; \frac{2}{Re}\int_{\mathrm{wake}} \left(\frac{\overline{\omega} a}{U_\infty}\right)\frac{dy}{a} \;-\; \overline{\boldsymbol{\Sigma}}_{2-\mathrm{D}}\cdot\mathbf{e}_y\;. \tag{A.3.3}$$

Because $\overline{\Gamma}$ tends to a constant outside a small neighborhood of the body (*e.g.*, Thom 1931) and $\overline{C}_L$ is a property of the body, it is apparent that

$$\frac{2}{Re}\int_{\text{wake}}\left(\frac{\overline{\omega}a}{U_\infty}\right)\frac{dy}{a} - \overline{\Sigma}_{2-\text{D}}\cdot\mathbf{e}_y \sim \text{const.},$$

and since $\overline{\Sigma}$ approaches zero for large contours, it is proposed that

$$\frac{2}{Re}\int_{\text{wake}}\left(\frac{\overline{\omega}d}{U_\infty}\right)\frac{dy}{d} - \overline{\Sigma}_{2-\text{D}}\cdot\mathbf{e}_y \sim \frac{2}{Re}\frac{\Delta u}{U_\infty}$$

for *any* contour about the body that traverses the wake vertically, where Δu is the velocity jump across the wake at a large distance from the body. Equation A.3.3 can then be written as

$$\overline{C}_L = -\frac{\overline{\Gamma}}{U_\infty a} + \mathcal{O}\left(\frac{2}{Re}\frac{\Delta u}{U_\infty}\right). \qquad \text{(A.3.4)}$$

For even moderate Re, the second term in Eq. A.3.4 may be neglected, since $\Delta u/U_\infty$ will also tend to be small.

APPENDIX B

Streamlines averaged at constant forcing phase.

Forcing function:

$$\frac{\dot{\theta}(t)\,a}{U_\infty} \;=\; -\Omega_1 \sin\left(\pi S_f \frac{U_\infty t}{a}\right) \;,$$

where $\Omega_1 = 2$, $S_f = 0.94$, and $Re = 2.1 \times 10^4$ for the present experiments. In the figures, a negative rotation is in the clockwise direction. See Ch. 4 for a description of these data.

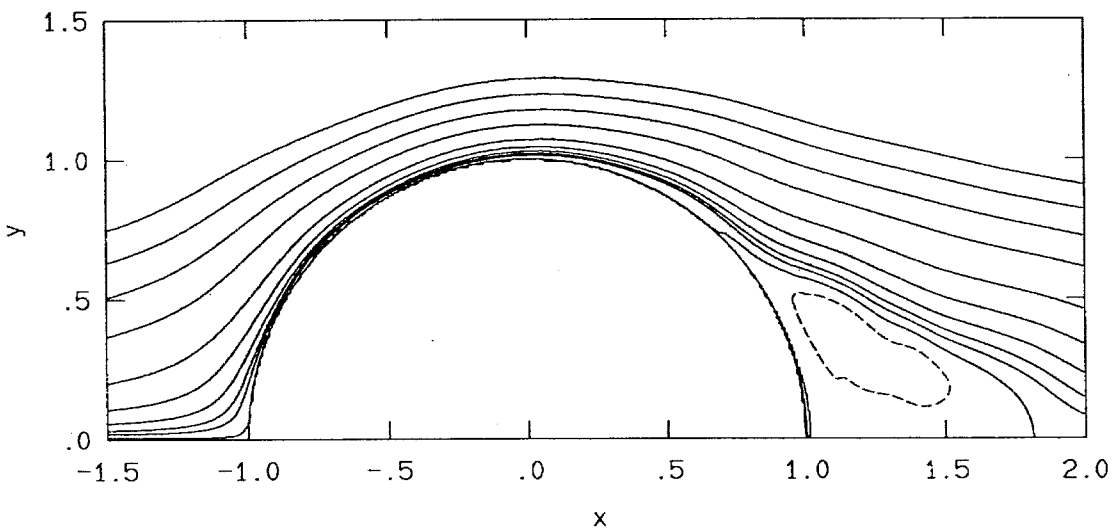

FIG. B.1 Time-averaged streamlines.

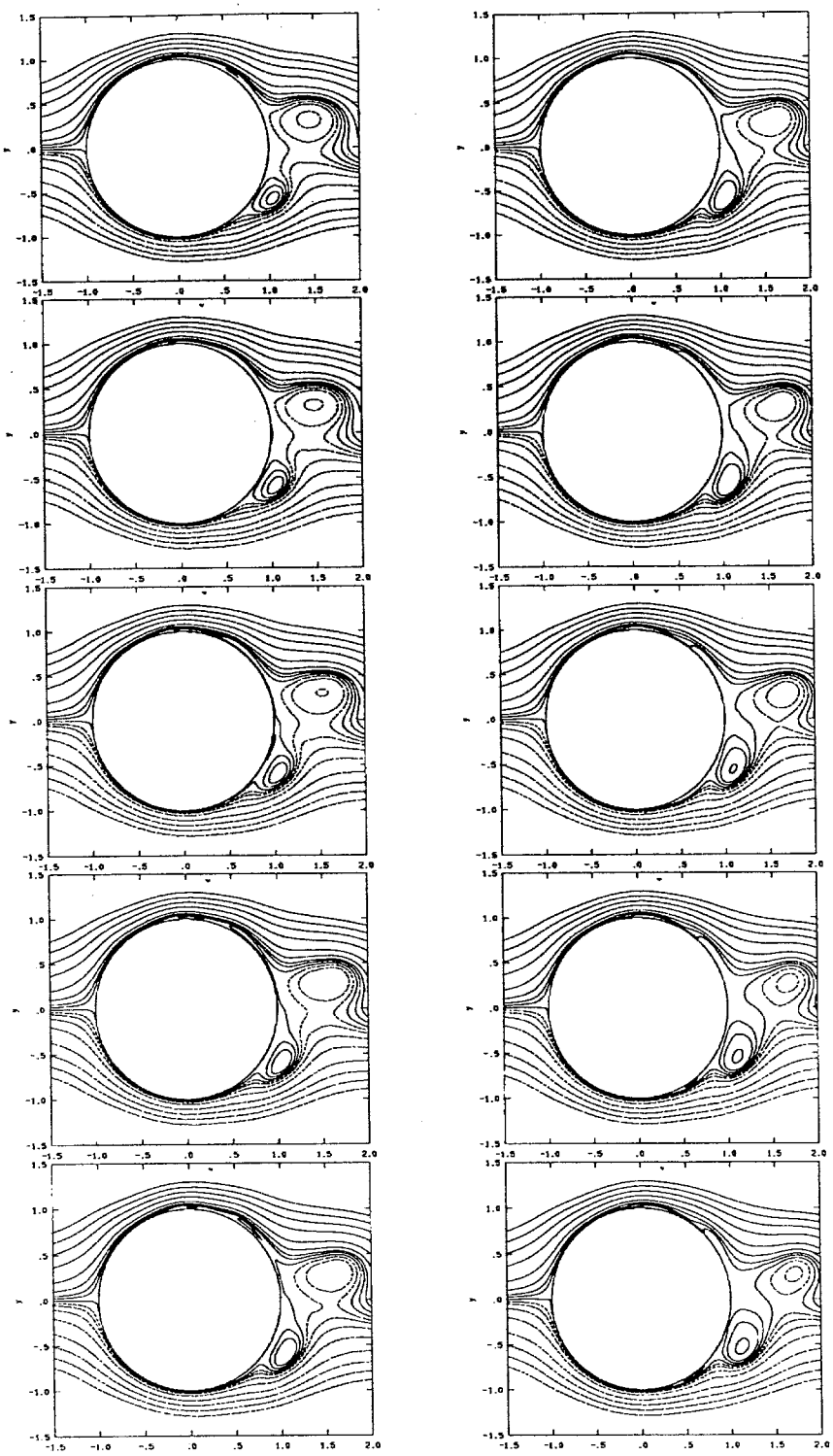

FIG. B.2 Streamlines for flow averaged at constant phase. Sequence on left: $0.00 \leq ft \leq 0.08$, right: $0.10 \leq ft \leq 0.18$.

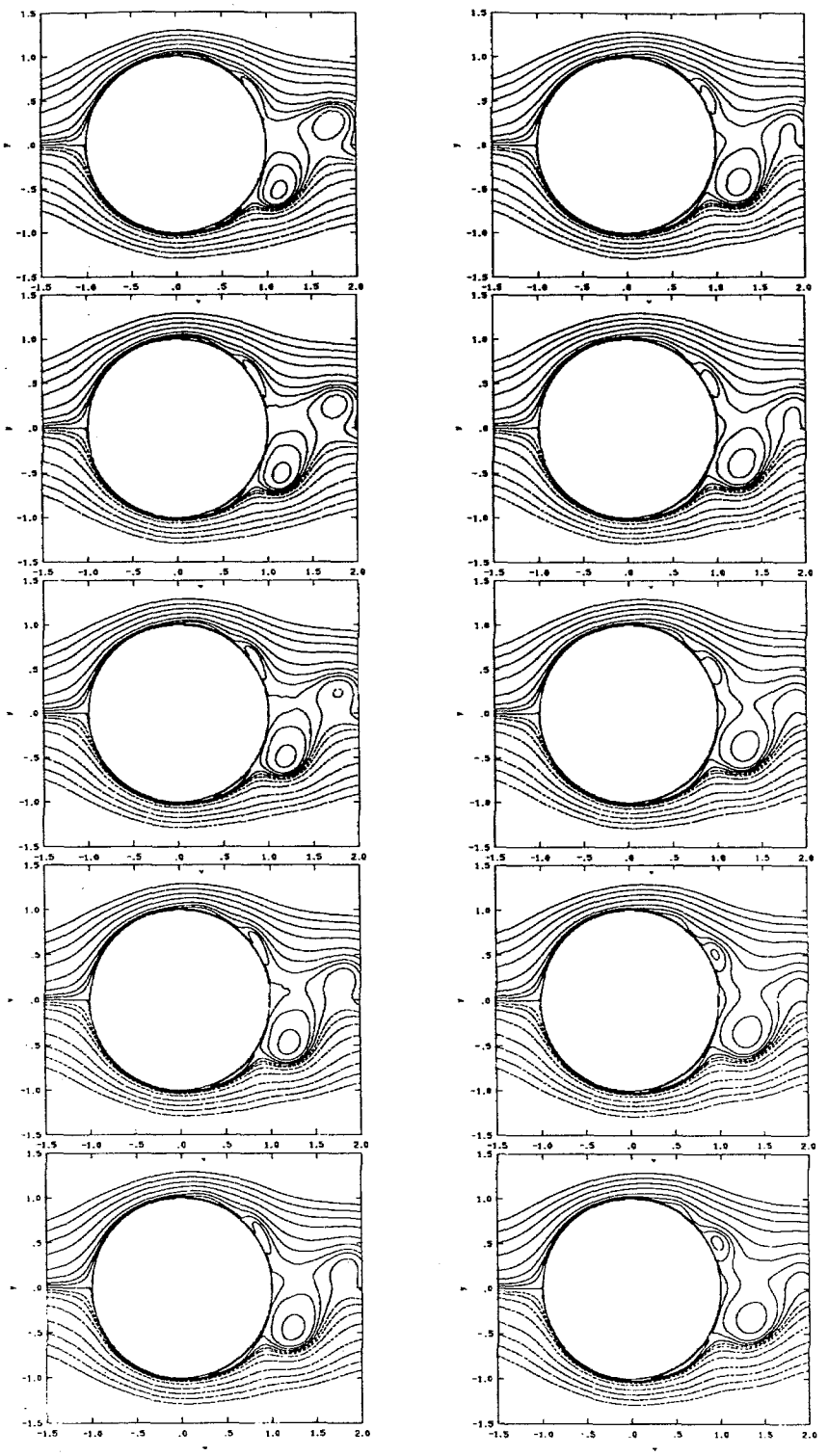

FIG. B.3 Streamlines for flow averaged at constant phase. Sequence on left: $0.20 \leq ft \leq 0.28$, right: $0.30 \leq ft \leq 0.38$.

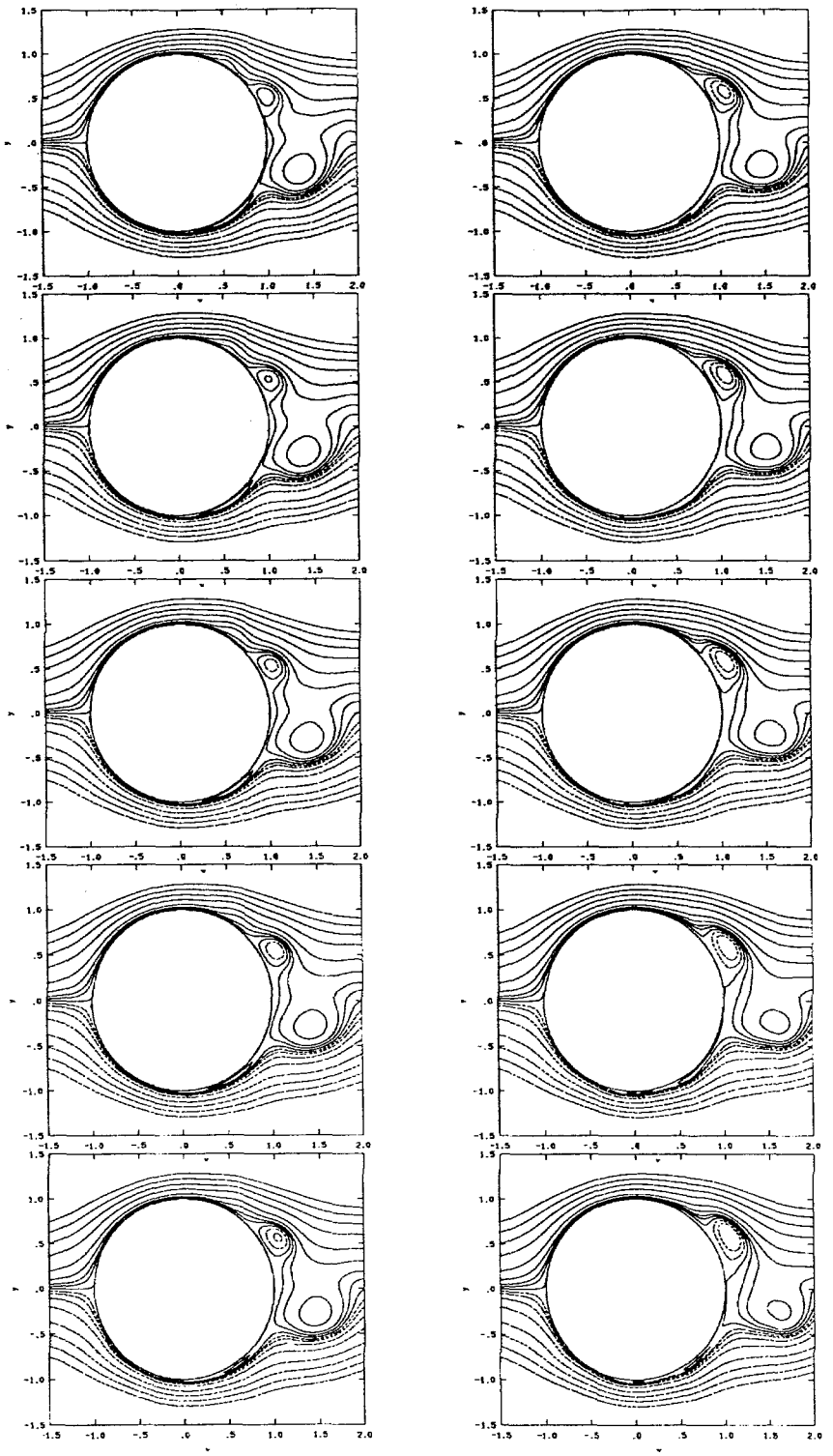

FIG. B.4 Streamlines for flow averaged at constant phase. Sequence on left: $0.40 \leq ft \leq 0.48$, right: $0.50 \leq ft \leq 0.58$.

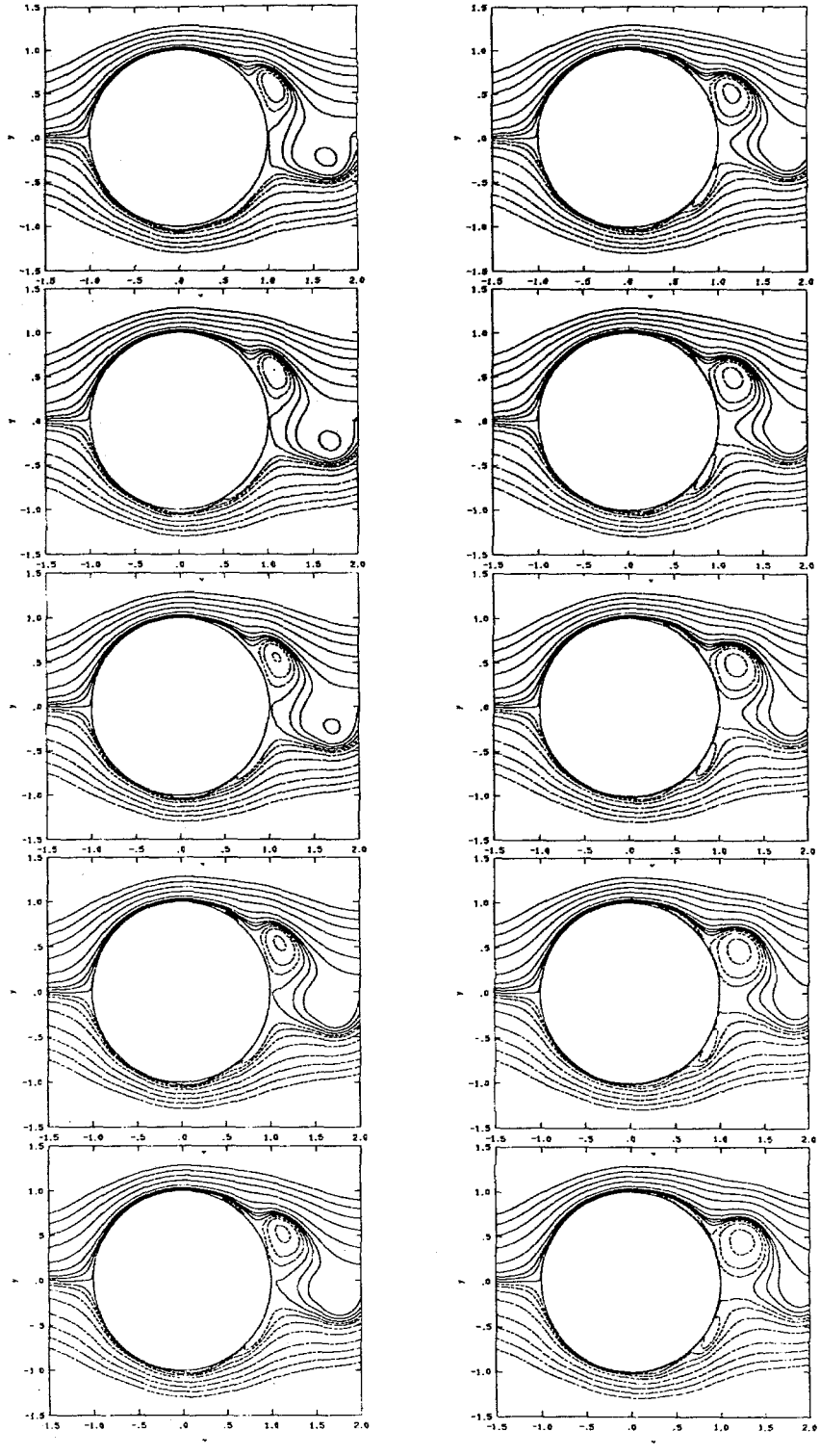

FIG. B.5 Streamlines for flow averaged at constant phase. Sequence on left: $0.60 \leq ft \leq 0.68$, right: $0.70 \leq ft \leq 0.78$.

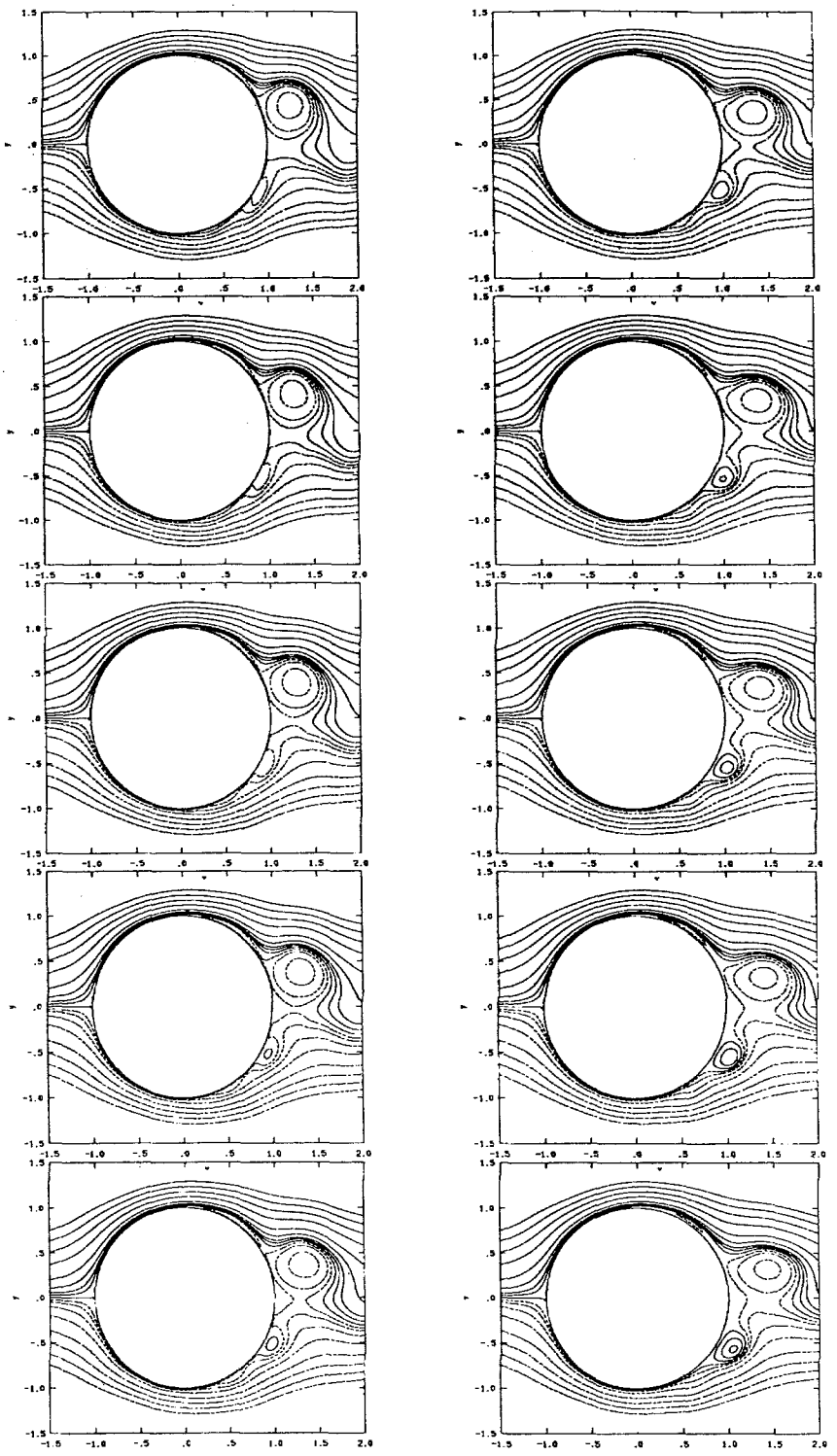

FIG. B.6 Streamlines for flow averaged at constant phase. Sequence on left: $0.80 \leq ft \leq 0.88$, right: $0.90 \leq ft \leq 0.98$.

APPENDIX R

References

BADAR, H. M., COUTANCEAU, M., DENNIS, S. C. R. and MÉNARD, C. [1990] "Unsteady flow past a rotating circular cylinder at Reynolds numbers 10^3 and 10^4," *J. Fluid Mech.* **220**, 459-484.

BATCHELOR, G. K. [1970] *An Introduction to Fluid Dynamics* (Cambridge U. Press).

BISHOP, R. E. D. and HASSAN, A. Y. [1964] "The lift and drag on a circular cylinder oscillating in a flow field," *Proc. Roy. Soc. London* A **277**, 51–75.

BRATT, J. B. [1953] "Flow patterns in the wake of an oscillating aerofoil," *Aero. Res. Counc. R. & M.*, No. 2773.

CHOMAZ, J. M., HUERRE, P. and REDEKOPP, L. G. [1988] "Bifurcations to Local and Global Modes in Spatially Developing Flows," *Phys. Rev. Lett.* **60**(1), January, pp. 25-28.

CIMBALA, J. M., NAGIB, H. M. and ROSHKO, A. [1988] "Large structure in the far wakes of two-dimensional bluff-bodies," *J. Fluid Mech.* **190**, 265–298.

DIMOTAKIS, P. E. [1978] "Laser-Doppler Velocimetry Momentum Defect Measurements of Cable Drag at Low to Moderate Reynolds Numbers," NCBC Report,

Contract No. N62583/77–M–R541.

FFOWCS-WILLIAMS, J. E. and ZHAO, B. C. [1989] "The Active Control of Vortex Shedding," *J. Fluids and Structures* **3**, 115–122.

GOLDSTEIN, S. [1938] *Modern Developments in Fluid Dynamics* (Clarendon Press, Oxford. Reprinted 1965, Dover publications).

GUCKENHEIMER, J. and HOLMES, P. [1983] *Nonlinear Oscillations, Dynamical Systems, and Bifurcations of Vector Fields,* (Springer-Verlag, New York).

HUERRE, P. and MONKEWITZ, P. A. [1985] "Absolute and convective instabilities in free shear layers," *J. Fluid Mech.* **159**, 151–168.

KARNIADAKIS, G. E. and TRIANTAFYLLOU, G. S. [1989] "Frequency selection and asymptotic states in laminar wakes," *J. Fluid Mech.* **199**, 441–469.

KOCH, W. [1985] "Local Instability Characteristics and Frequency Determination of Self-Excited Wake Flows," *J. Sound & Vibration* **99**(1), 53–83.

KOOCHESFAHANI, M. M. [1987] "Vortical Pattern in the Wake of an Oscillating Airfoil," *AIAA* 25^{th} *Aerospace Sciences Meeting*, 12–15 January 1987 (Reno, Nevada), AIAA Paper No. 87-0111.

KOOCHESFAHANI, M. M. and DIMOTAKIS, P. E. [1988] "A Cancellation Experiment in a Forced Turbulent Shear Layer," *First National Fluid Dynamics Congress*, 25–28 July 1988 (Cincinnati, Ohio), Proceedings **II**, 1204–1208.

KOOPMAN, G. H. [1967] "The Vortex wakes of vibrating cylinders at low Reynolds numbers," *J. Fluid Mech.* **28**, 501–512.

KUROSAKA, M., CHRISTIANSEN, W. H., GOODMAN, J. R., TIRRES, L. and WOHLMAN, R. A. [1988] "Crossflow Transport Induced by Vortices," *AIAA Journal* **26** (11), 1403–1405.

LANDAU, L. D. [1944] "On the Problem of Turbulence," *C. R. Acad. Sci. URSS* **44**, 311–314.

LANDAU, L. D. and LIFSHITZ, E. M. [1987] *Fluid Mechanics* 2^{nd} *edition,* (Pergamon Press, New York).

LANG, D. B. [1985] *Laser Doppler Velocity and Vorticity Measurements in Turbulent Shear Layers*, Ph.D. thesis, California Institute of Technology.

LEONARD, A. [1987] "Numerical Methods in Fluid Mechanics," Ae232 Lecture notes, California Institute of Technology.

LIEPMANN, H. W., BROWN, G. L. and NOSENCHUCK, D. M. [1982] "Control of Laminar-Instability Waves using a New Technique," *J. Fluid Mech.* **118**, 187-200.

LIEPMANN, H. W. and NOSENCHUCK, D. M. [1982] "Active control of laminar-turbulent transition," *J. Fluid Mech.* **118**, 201-204.

MAGNUS [1853] *Poggendorf's Annalen der Physik u. Chemie* **88**, 1-14.

MILNE-THOMSON, L. M. [1968] *Theoretical Hydrodynamics,* (The MacMillan

Company, New York).

MONKEWITZ, P. A. and NGUYEN, L. N. [1987] "Absolute Instability in the Near-Wake of Two-Dimensional Bluff Bodies," *J. Fluids and Structures* **1**, 165–184.

MONKEWITZ, P. A. [1988] "The absolute and convective nature of instability in two-dimensional wakes at low Reynolds numbers," *Phys. Fluids* **31** (5), 999–1006.

OKAJIMA, A., TAKATA, H. and ASANUMA, T. [1975] "Viscous Flow Around a Rotationally Oscillating Circular Cylinder," *Inst. Sp. & Aero. Sc.* (U. Tokyo), Report No. 532.

ONGOREN, A. and ROCKWELL, D. [1988a] "Flow structure from an oscillating cylinder, Part 1. Mechanisms of phase shift and recovery in the near wake," *J. Fluid Mech.* **191**, 197–223.

ONGOREN, A. and ROCKWELL, D. [1988b] "Flow structure from an oscillating cylinder, Part 2. Mode competition in the near wake," *J. Fluid Mech.* **191**, 225–245.

PRANDTL, L. [1925] *Die Naturwissenschaften,* **13** p. 93-108.

PRESS, W. H., FLANNERY, B. P., TEUKOLSKY, A. A. and VETTERLING, W. T. [1986] *Numerical Recipes. The Art of Scientific Computing.* (Cambridge Univ. Press).

PROVANSAL, M., MATHIS, C. and BOYER, L. [1987] "Bénard - von Kármán instability: transient and forced regimes," *J. Fluid Mech.* **182**, 1–22.

REID, E. G. [1924] "Tests of rotating cylinders," *NACA Technical Note* No. 209.

ROBERTS, F. A. [1985] *Effects of a Periodic Disturbance on Structure and Mixing in Turbulent Shear Layers and Wakes*, Ph.D. thesis, California Institute of Technology.

ROBERTS, F. A. and ROSHKO, A. [1985] "Effects of Periodic Forcing on Mixing in Turbulent Shear Layers and Wakes," AIAA Shear Flow Control Conference, 12-14 March 1985 (Boulder, CO), AIAA Paper No. 85-0570.

ROSHKO, A. [1954a] "On the drag and shedding frequency of two-dimensional bluff bodies," *N.A.C.A., Tech. Note* 3169.

ROSHKO, A. [1954b] "On the drag and shedding frequency of bluff cylinders," *J. Aero. Sci.* **22**, 124–132.

ROSHKO, A. [1954c] "On the development of turbulent wakes from vortex streets," *N.A.C.A., Report* 1191.

STUART, J. T. [1958] "On the non-linear mechanics of hydrodynamic stability," *J. Fluid Mech.* **4**, 1–21.

STUART, J. T. [1960] "On the non-linear mechanics of wave disturbances in stable and unstable parallel flows," *J. Fluid Mech.* **9**, 353–370.

TANEDA, S. [1978] "Visual Observations of the Flow Past a Circular Cylinder Performing a Rotatory Oscillation," *J. Phys. Soc. J.* **45**(3), 1038–1043.

TAYLOR, G. I. [1925] *Phil. Trans.* **A**, p. 238-245.

THOM, A. [1926] "The pressure round a cylinder rotating in an air current," *A.R.C. Reports and Memoranda, No.* 1082.

THOM, A. [1931] "Experiments on the flow past a rotating cylinder," *A.R.C. Reports and Memoranda, No.* 1410.

THWAITES, B. [1960] *Incompressible Aerodynamics* ((Clarendon Press, Oxford). Reprinted (1978, Dover Publications)).

TOKUMARU, P. and DIMOTAKIS, P. [1991] "Rotary oscillation control of a cylinder wake," *J. Fluid Mech.* **224**, 77–90.

TRIANTAFYLLOU, G. S., TRIANTAFYLLOU, M. S. and CHRYSSOSTOMIDIS [1986] "On the formation of vortex streets behind stationary cylinders," *J. Fluid Mech.* **170**, 461–477.

TRITTON, D. J. [1959] "Experiments on the flow past a circular cylinder at low Reynolds numbers," *J. Fluid Mech.* **6**, 547–567.

TRITTON, D. J. [1988] *Physical Fluid Dynamics* (2^{nd} edition, Clarendon Press, Oxford).

WARD, T. W. [1976] "The Hydrodynamics Laboratory at the California Institute of Technology," *Transactions A.S.M.E. Journal of Fluids Engineering*, **98**:740-748

WEIHS, D. [1972] "Semi-infinite vortex trails, and their relation to oscillating airfoils," *J. Fluid Mech.* **54**(4), 679–690.

WILLIAMS, D. R. and AMATO, C. W. [1988] "Unsteady Pulsing of Cylinder Wakes," Proceedings, *First National Fluid Dynamics Congress*, 25–28 July 1988 (Cincinnati, Ohio), 731–737 (AIAA–88–3532–CP).

WILLIAMSON, C. H. K. and ROSHKO, A. [1988] "Vortex formation in the wake of an oscillating cylinder," *J. Fluids and Structures* **2**, 355–381.

WU, J., MO, J. and VAKILI, A. [1989] "On the Wake of a Cylinder with Rotational Oscillations," *AIAA* 2^{nd} *Shear Flow Conference*, 13-16 March 1989 (Tempe, AZ), AIAA Paper No. 89-1024.